



UNIVERSIDAD DEL VALLE

TRABAJO DE GRADO

DINÁMICA DE UNO Y DOS BOSONES RETICULARES DE
ESPÍN 1 EN PRESENCIA DE CAMPOS MAGNÉTICOS
PERIÓDICOS EXTERNOS

SINGLE AND TWO-PARTICLES DYNAMICS OF SPIN-1
LATTICE BOSONS IN PRESENCE OF EXTERNAL
PERIODIC MAGNETIC FIELDS

PRESENTADO POR
SEBASTIÁN LOAIZA OSPINA

DIRIGIDO POR
DR. RER. NAT KAREM RODRÍGUEZ RAMÍREZ

FACULTAD DE CIENCIAS NATURALES Y EXACTAS

DEPARTAMENTO DE FÍSICA-3146

2024

To me

Agradecimientos

Quisiera agradecer primeramente a mi familia, a mi madre Martha Ospina que me apoyó incondicionalmente durante toda mi carrera, a mi padre Ramón Loaiza que siempre estuvo presente luchando porque nunca me faltara nada y sin duda a mi hermano Julián Loaiza que con sus ayudas y consejos me permitieron también salir adelante, gracias a ustedes soy la persona que soy y me siento muy orgulloso de ello. Agradezco mucho también a mi tía Beatriz Correa, a mi tío Oscar Ospina, los cuales me acogieron y ayudaron como si fuera uno de sus hijos, y gracias en general a todos los miembros de mi familia que de una forma u otra me ayudaron y apoyaron durante mi carrera.

Le agradezco también mucho a la profesora Karem Rodríguez, por su ayuda constante a lo largo de este trabajo y de la cual no solo aprendí muchísimas cosas como físico si no también como ser humano. Agradezco igualmente a mis compañeros y amigos de carrera Santiago Olave y Krystifer Campos los cuales me acompañaron literalmente desde el inicio hasta al final en esta travesía.

Agradezco también a la Universidad del Valle y al Departamento de Física por forjar mi carácter y brindarme una formación excelente, además del apoyo financiero brindado para este proyecto y para representarla internacionalmente en mi paso por el grupo IPT Univalle, donde viví una de las mejores experiencias que he tenido.

Finalmente, quisiera agradecer infinitamente a mi compañera de vida, Natalia Zules, la cual me apoyó, ayudó y aguantó durante estos 5 años, y que espero que pueda seguirlo haciendo durante muchísimos años más, como siempre lo ha hecho incluso antes de que me planteara ser físico.

Gracias.

Resumen

La realización experimental del condensado de Bose-Einstein ha resaltado la importancia de controlar y manipular con facilidad sistemas cuánticos cada vez más complejos. En este contexto, el estudio de átomos ultrafríos cargados en redes ópticas ha demostrado cumplir con estas exigencias, proporcionando escenarios ideales para investigar sistemas cuánticos muy complejos que solo pueden ser analizados a través de simuladores cuánticos. El presente trabajo tiene como objetivo principal desarrollar e implementar numéricamente el teorema de Floquet, específicamente mediante su método del espacio de Hilbert extendido, para el estudio dinámico de uno y dos bosones de espín 1 cargados en una red óptica unidimensional en el régimen de superfluído, utilizando como base el hamiltoniano de Bose-Hubbard de espín 1. Además, se aborda el estudio de dicho sistema bajo la influencia de campos de Zeeman lineales o cuadráticos externos conducidos periódicamente de manera tanto lineal como cuadrática.

En primer lugar, se presenta el modelo a estudiar. Comenzamos con el modelo de Bose-Hubbard sin espín, para luego incorporar el grado de libertad de espín 1 junto con sus interacciones e incluir campos de Zeeman lineales y cuadráticos acoplados a un driving periódico, lo que sitúa nuestro sistema en un marco dinámico. Posteriormente, se introduce la representación bosónica de SU(3) para espín 1 como grupo de simetría, junto con las bases, estados y observables relevantes necesarios para caracterizar completamente nuestro sistema.

Para analizar eficazmente este sistema, se emplea una técnica numérica basada en la teoría de Floquet. Se describe el teorema de Floquet, sus implicaciones y sus analogías con el teorema de Bloch. Luego, se presenta el método numérico principal utilizado en nuestro análisis: el método del espacio de Hilbert extendido, que aprovecha la naturaleza periódica de nuestro sistema para transferir el problema al espacio armónico de Fourier, donde la evolución del estado se puede determinar fácilmente. Este método se valida resolviendo analíticamente de manera exacta nuestro sistema de una partícula en dos sitios y se compara con nuestra implementación numérica, demostrando una coincidencia sin errores discernibles.

Entre los resultados obtenidos, se muestra que, independientemente de la presencia de interacciones cuadrupolares o incluso de interacciones del tipo densidad entre partículas, cualquier estado de espín 1 muestra inherentemente tanto orden cuadrupolar como espinorial. De hecho, se muestra que, cuando el estado inicial es un estado local, sin importar el campo aplicado, la dinámica del orden cuadrupolar junto con la espinorial puede condensarse en la desigualdad $\frac{10}{9} \leq \langle \hat{\mathbf{S}} \rangle_t^2 + \langle \hat{\mathbf{Q}} \rangle_t^2 \leq \frac{4}{3}$, donde el límite superior e inferior resultan ser los valores propios de los operadores cuadrático y

cúbico de Casimir del grupo SU(3), respectivamente. Adicionalmente, se muestra que la presencia de campos magnéticos genera nuevas fases y fenómenos en los sistemas, tales como la ruptura de la simetría de invarianza temporal en el caso de una sola partícula bajo un campo lineal, lo que da lugar a fenómenos como la precesión del espín o la resonancia del spin-mixing en el caso de dos partículas bajo un campo cuadrático, donde la intensidad del campo y la interacción entran en fase mostrando oscilaciones máximas y rápidas que no decaen en el tiempo.

Finalmente, se concluye que el método numérico del espacio de Hilbert extendido basado en el teorema de Floquet es una herramienta robusta y de alto nivel que proporciona una forma directa y sencilla de estudiar sistemas cuánticos de manera dinámica, incluso en presencia de interacciones complejas y espacios de Hilbert grandes. Además, demuestra una versatilidad notable para analizar los sistemas desde distintos regímenes impuestos por la periodicidad del driving acoplado, tales como el régimen de altas frecuencias, bajo la aproximación de onda rotante, el régimen fuerte, entre otros.

Palabras Clave: Redes ópticas, modelo de Bose-Hubbard de espin-1, régimen superfluido, teoría de Floquet.

Abstract

The experimental realization of Bose-Einstein condensates has highlighted the importance of controlling and easily manipulating increasingly complex quantum systems. In this context, the study of ultracold atoms loaded into optical lattices has proven to meet these demands, providing ideal scenarios for investigating highly complex quantum systems that can only be analyzed through quantum simulators. The main objective of this work is to develop and implement Floquet's theorem numerically, specifically through its extended Hilbert space method, to study the dynamics of one and two spin-1 bosons loaded into a one-dimensional optical lattice in the superfluid regime, using the spin-1 Bose-Hubbard Hamiltonian as the foundational model. Additionally, this work explores the system's behavior under the influence of external linear and quadratic Zeeman fields, with periodic driving applied in both linear and quadratic forms.

First, the model to be studied is presented. We begin with the spinless Bose-Hubbard model and then incorporate the spin-1 degree of freedom along with its interactions, including both linear and quadratic Zeeman fields coupled to a periodic driving, which places our system in a dynamic framework. Subsequently, the SU(3) bosonic representation of a spin-1 as a symmetry group is introduced, along with the relevant bases, states, and observables necessary to fully characterize our system.

To effectively analyze this system, a numerical technique based on Floquet theory is employed. Floquet's theorem, its implications, and its analogies with Bloch's theorem are described. Then, the main numerical method used in our analysis is presented: the extended Hilbert space method, which takes advantage of the periodic nature of our system to transfer the problem into Fourier harmonic space, where the state's evolution can be easily determined. This method is validated by analytically solving our one-particle system exactly in two sites and comparing it with our numerical implementation, demonstrating a perfect match with no discernible errors.

Among the results obtained, it is shown that, regardless of the presence of quadrupolar interactions or any particle density type interaction at all, an arbitrary spin-1 state inherently exhibits both quadrupolar and spin order. In fact, it is shown that when the initial state is a local state, regardless of the applied field, the dynamics of the quadrupolar order together with the spin order can be condensed into the inequality $\frac{10}{9} \leq \langle \hat{\mathbf{S}} \rangle_t^2 + \langle \hat{\mathbf{Q}} \rangle_t^2 \leq \frac{4}{3}$, where the upper and lower limits correspond to the eigenvalues of the quadratic and cubic Casimir operators of the SU(3) group, respectively. Additionally, it is shown that the presence of magnetic fields generates new phases and phenomena in the systems, such as the breaking of time-invariance symmetry in the case of a single particle

under a linear field, leading to phenomena such as spin precession or spin-mixing resonance in the case of two particles under a quadratic field, where the field intensity and interaction come into phase, showing maximum and rapid oscillations that do not decay over time.

Finally, it is concluded that the extended Hilbert space method based on Floquet's theorem is a robust and high-level tool that provides a straightforward and simple way to study quantum systems dynamically, even in the presence of complex interactions and large Hilbert spaces. Additionally, it demonstrates notable versatility for analyzing systems from different regimes imposed by the periodicity of the coupled driving, such as the high-frequency regime, under the rotating wave approximation, the strong-driving regime, among others.

Key words: Optical lattices, Spin-1 Bose-Hubbard model, Superfluid regime, Floquet theory.

CONTENTS

1	Introduction	1
2	Spin-1 System Modeling	5
2.1	Bose-Hubbard model	5
2.2	Superfluid-Mott Insulator transition	7
2.2.1	Mott-Insulator phase $J \ll U$	8
2.2.2	Superfluid phase $J \gg U$	9
2.3	Spin-1 Bose-Hubbard model	10
2.3.1	Interacting Potential	10
2.3.2	External Fields	11
2.4	Building the time-dependent driving Hamiltonian	13
2.4.1	One particle dynamics	14
2.4.2	Two particles dynamics	16
2.5	Single Spin-1 Characterization	19
2.5.1	SU(2) Description	19
2.5.2	SU(3)-Bosonic Representation of a Spin-1	20
2.5.3	Spin-1 Basis	22
2.5.4	Physical Observables	27
3	Floquet Formalism	29
3.1	Floquet's Theorem	29
3.1.1	Consequences of Floquet's Theorem	30
3.1.2	Analogies between Bloch's Theorem and Floquet's Theorem	33
3.2	Numerically solving the Floquet problem	34
3.2.1	The Extended Hilbert Space	35
3.2.2	Truncation of the harmonic Fourier space	37
3.3	Implementation of the Floquet's Theorem	39
3.3.1	Exact Solution	39
3.3.2	Numerical implementation	42
3.3.3	Comparison between analytical and numerical solutions	43

CONTENTS

4	Dynamical Analysis	46
4.1	One particle	46
4.1.1	Linear Zeeman Field	49
4.1.2	Quadratic Zeeman Field	59
4.2	Two particles	63
4.2.1	Antiferromagnetic phase $U_2 > 0$	66
4.2.2	Ferromagnetic phase $U_2 < 0$	70
5	Conclusions and Perspectives	73
5.1	Conclusions	73
5.2	Perspectives	75
A	Spin 1 Calculations	77
A.1	Interaction Potential	77
A.2	Second quantization	79
A.3	Schwinger Bosons (SB)	81
A.4	SU(3) Group	82
B	Supplementary Material on Floquet Theory	85
B.1	Proof of Floquet theorem	85
B.2	Alternative Approaches to Numerical Solutions	89
B.2.1	Exact Time-Evolution of $\hat{U}(t_0 + T, t_0)$	89
B.2.2	Trotter Decomposition of $\hat{U}(t_0 + T, t_0)$	89
B.3	Summary of important definitions	91
C	Floquet's Implementation in C/C++	92
D	Additional Findings on the dynamical analysis	95
D.1	One Particle	95
D.1.1	Effect of Relative Phases	95
D.1.2	Driving Variations	97
D.2	Two particles	99
D.2.1	Increase in the number of sites	99
	Bibliography	101

Chapter 1

INTRODUCTION

In the early 20th century, the emergence of quantum mechanics captivated physicists with its numerous counterintuitive predictions, including wave-particle duality [1], the principles of superposition [2], quantum entanglement [3] among many others. Within this paradigm, in 1925, physicists Satyendra N. Bose and Albert Einstein proposed a distinctive prediction, they predicted that a group of bosonic atoms at ultra-low temperatures could all occupy the lowest quantum state of the system, thus forming a “Super Atom” due to the overlap of all present wave functions. This phenomenon led to the recognition of what we now call the fifth state of matter, the Bose-Einstein Condensate [4, 5]. The extraction of these physical properties at a macroscopic level was a dream and challenge for the technology of that time, due to the states required temperatures close to absolute zero. It was not until 1995 that Eric Cornell and Carl Wieman, using rubidium atoms, managed to achieve microkelvin (μK) temperatures through laser cooling, specifically Doppler cooling [6, 7], and then used magnetic traps with evaporative cooling [8, 9] to obtain nanokelvin (nK). This experiment marked the first experimental realization of this quantum state, theorized at the start of the century—the Bose-Einstein Condensate [10]. This discovery implied a great increase in interest in the control and manipulation of quantum systems that showed increasing eccentricity in their properties, starting a new era, since that, the physics of ultra-cold atoms and the use of lasers have been marked by numerous Nobel Prizes until today [11, 12, 13, 14, 15, 16]. These fields continue to be studied both theoretically and experimentally, further exploring these quantum phenomena that captivate and drive technological advancements.

In this context, the study of ultra-cold atoms loaded into optical lattices has gained significant relevance due to the possibility of controlling and manipulating various parameters within the system, thus facilitating the study of quantum states [17], quantum phases [18], and quantum phase transitions [19] with greater ease. This approach has proven to be one of the most powerful and useful tools for driving advancements in several areas of physics, both at the experimental and theoretical levels enclosing emerging fields such as quantum simulators [20] and quantum information [21], as well as areas with broader applicability like quantum sensors [22], interferometry [23], and others like photonics [24].

CHAPTER 1. INTRODUCTION

Optical lattices are periodic potentials created by superposition of lasers, where massive particles can be uploaded due to the light-matter interaction. This interaction can be explained through two processes [25]: the conservative process, which induces a dipole moment in the atom that interacts with the electric field to create a spatially dependent potential energy and thus trapping the atom; and the dissipative process, which involves multiple cycles of stimulated absorption followed by spontaneous emission, eventually cooling the atom. A significant aspect of optical lattices is their resemblance to the crystal structures of typical solids [26], which allows the well-established theory of solids to be applied to these systems and where depending on their dimensionality, different properties may arise. Various geometries have been explored over the years [27, 28, 29] with the one-dimensional (1D) case being particularly interesting due to the inevitable interactions among the particles loaded into the lattice, which provides a unique environment to explore quantum coherence and cooperativity, which is the focus of this work.

Within this context, the importance of many-body physics and the formalism of second quantization become evident. The indistinguishable nature of bosons in these systems facilitates the exploration of collective quantum phenomena such as superfluidity [30], which is the main phase explored in this work. Moreover, the formalism of second quantization is an indispensable tool for effectively incorporating the quantum statistics of particles, providing a natural framework for describing transitions between different many-body states and their associated dynamics [31]. In optical lattices, the interactions between particles can range from binary collisions to three-body and even four-body interactions, and for this work, we focus primarily on binary collisions, where the interactions between their internal degrees of freedom such as the spin have to be taken into account as well. Particularly in spin-1 systems, phenomena such as spin mixing can be observed [32] see chapter 2 for further details. Furthermore, when external fields like a Zeeman ones either linear or quadratic are considered, a comprehensive description of the system emerges [33], taking into account all its phases and the intrinsically present quantum magnetism [34, 35].

However, due to the Hilbert space size associated with spin bosonic systems and the complexity of the interactions present in their Hamiltonians, direct analysis is generally very challenging. Consequently, the use of advanced computational techniques and alternative methods becomes essential for an adequate description. Such methods include Quantum Monte Carlo (QMC) [36, 37], Density Matrix Renormalization Group (DMRG) [34, 38], the Gutzwiller ansatz [39, 40], among other computational approaches. Typically, these methods are used to characterize the system based on specific parameters that depend on the space, interactions, or some other variable specific to the system. The ability to adjust parameters of cold atoms and optical lattices enables the

CHAPTER 1. INTRODUCTION

study of out-of-equilibrium dynamics, a field that is still emerging and rather challenging. To date, only a few topics within this field have been investigated, with most studies focusing on spinless bosons [41, 42]. Therefore, the dynamics of spinor bosons remains an emerging field, where research has primarily concentrated on mean field studies [43], dynamical instability [44], and only a few investigations have explored the effects of external magnetic fields [45]. In this context, the Floquet theory formalism [46] provides an effective approach for studying dynamical systems and addressing temporal evolution in periodic systems, which is of great interest for this work.

Floquet theory is a sophisticated approach used to solve systems of ordinary differential equations subject to periodic time conditions. Its central element is Floquet's theorem, and it was proposed by Gaston Floquet in 1883 providing the general form of system solutions [47]. Traditionally, Floquet theory has not been the method of choice for solving ordinary differential equations due to the analytical convenience offered by other techniques, such as characteristic equations. Moreover, the application of Floquet theory requires that the system under study satisfy a certain periodicity condition. However, as physical systems become more complex and the demand for numerical methods has increased, simpler approaches often prove inadequate, leading to the inclusion of periodic driven in the systems [48]. In recent years, Floquet theory has become a powerful analytical and numerical tool, making significant contributions to both classical and quantum systems, including studies in open systems [49], prethermalization [50], chaos [51], topology [52], condensed matter [53] or even in exotic quantum phenomena such as time crystals [54] among many others. Particularly in the physics of condensed matter, when, together with its spatial counterpart, Bloch's theorem, is taking into account the exploitation of spatial and temporal discretization arise, giving to significant advances in fields such as optical lattices [55, 56]. In this framework, the study of the dynamics of spin-1 bosons trapped in an optical lattice, modeled by external periodic magnetic fields, provides a perfect scenario where Floquet theory allows the comprehensive extraction of information from the system, the main numerical technique of this work.

This document is organized as follows: In Chapter 2, we explore the spin-1 Bose-Hubbard Hamiltonian which effectively describes a system of ultracold spin-1 particles trapped in a one-dimensional optical lattice within the superfluid regime. We subsequently incorporate a time dependence through periodic Zeeman magnetic fields and finally, a complete description of a single quantum spin-1 is provided, with general complementary material in Appendix A. In Chapter 3 we discuss the formalism of Floquet's theory, emphasizing its analogies with Bloch's theorem and the consequences of its central axis, Floquet's theorem. Subsequently, the numerical approach, the extended Hilbert space method with which the Floquet problem is treated is described and finally a comparison

CHAPTER 1. INTRODUCTION

between the numerical implementation and a particular case of our system that has an exact solution is provided. In addition, supplementary material on Floquet's theory is provided in Appendix **B** and details of its numerical implementation in C++ are provided in Appendix **C**. In Chapter **4** we perform the dynamic analysis for both the single-particle and two-particle systems, emphasizing in the single-particle system the effects of both quadratic and linear Zeeman fields in the different regimes provided by Floquet Theory. Subsequently we address the system of two particles only with a quadratic field focusing on the ferromagnetic and antiferromagnetic phase that the system presents. Also with deeper analysis and changes in the parameters of the systems in appendix **D**. Finally in the Chapter **5** the conclusions and perspectives collected throughout the work are presented for subsequent studies.

Chapter 2

SPIN-1 SYSTEM MODELING

The present investigation focuses on the study of one and two spin-1 bosons trapped in a one-dimensional optical lattice within the superfluid regime, subject to a periodic external magnetic field. Our discussion begins by introducing the Bose-Hubbard model, which describes ultracold spinless bosons loaded into a one-dimensional lattice system. Subsequently, we incorporate the spin-1 degree of freedom, which alters the contact interaction between particles into two independent scattering processes: charge scattering and spin scattering. Additionally, we introduce linear and quadratic external magnetic fields to partially eliminate degeneracy in the case of the quadratic Zeeman field, and completely in the case of the linear Zeeman field, thus allowing new magnetic phases to emerge which are going to be extended by incorporating a temporal periodicity. Finally, a complete description of a single quantum spin-1 is provided via the SU(3) bosonic representation, in addition to the bases, states and observables that we use to analyze our system.

2.1 Bose-Hubbard model

The model that describes bosonic particles (alkali atoms) loaded in an optical lattice is the Bose-Hubbard Hamiltonian [57], which is constructed taking into account the kinetic energy of the particles, the periodic potential of the lattice and the potential interaction between these, which is uniquely of the contact type for the spinless particles. In first quantization the Hamiltonian is expressed as,

$$\hat{H} = \sum_{i=1}^N \left(\frac{\hat{p}_i^2}{2m} + \hat{V}_{\text{lat}}(x_i) + \sum_{j \neq i}^N \hat{V}_{\text{int}}(x_i - x_j) \right), \quad (2.1)$$

where the first term represents the kinetic energy of the particles, and $\hat{V}_{\text{lat}}(x)$ and $\hat{V}_{\text{int}}(x - x')$ represent the periodic and interaction potentials, respectively. Since the system is composed by many particles, it is appropriate to move ourselves to the second quantization formalism, considering a basis that satisfies orthonormal conditions and is ideal to captures the discreteness of the space imposed by the lattice. The set of functions that fulfill these conditions are the Wannier functions, $W_j(x)$, characterized by their high localization in contrast to its dual, the Bloch functions,

$$W_j(x) = \frac{1}{\sqrt{L}} \sum_k e^{-ijkR/\hbar} \phi_k(x) \quad \text{and} \quad \int dx W_i^*(x) W_j(x) = \delta_{ij}, \quad (2.2)$$

where L is the number of lattice sites, R the lattice constant, $\phi_k(x)$ the Bloch functions, and k represents the quasi-momenta that include all possible values in the first Brillouin zone. Now, with the appropriate single particle basis established, we can construct the field operators $\hat{\Psi}(x)$ by expanding them in terms of the Wannier functions and the creation \hat{b}_i^\dagger and annihilation \hat{b}_i bosonic operators at the i -th site

$$\hat{\Psi}^\dagger(x) = \sum_i W_i^*(x) \hat{b}_i^\dagger \quad \text{and} \quad \hat{\Psi}(x) = \sum_i W_i(x) \hat{b}_i. \quad (2.3)$$

These operators adhere to the usual bosonic commutation relations:

$$\begin{aligned} [\hat{b}_i^\dagger, \hat{b}_j^\dagger] &= [\hat{b}_i, \hat{b}_j] = 0, & [\hat{b}_i, \hat{b}_j^\dagger] &= \delta_{ij}, \\ [\hat{\Psi}^\dagger(x), \hat{\Psi}^\dagger(x')] &= [\hat{\Psi}(x), \hat{\Psi}(x')] = 0, & [\hat{\Psi}(x), \hat{\Psi}^\dagger(x')] &= \delta(x - x'). \end{aligned}$$

Since we aim to describe a system of ultracold atoms, the interaction between particles in this context is modeled as binary collisions at the lowest energy orbital, namely the s-wave. Consequently, all information regarding the collision is captured in the scattering length a , which determines the strength of the interaction [58]. This is represented by a contact potential given by:

$$V_{\text{int}}(x - x') = \frac{4\pi\hbar^2 a}{m} \delta(x - x'), \quad (2.4)$$

being m the reduced mass of the particles. We can calculate the Hamiltonian in second quantization using the previously mentioned field operators by means of,

$$\hat{H} = \int dx \hat{\Psi}^\dagger(x) \left(-\frac{\hbar^2 \nabla^2}{2m} + V_{\text{lat}}(x) \right) \hat{\Psi}(x) + \frac{g}{2} \int dx dx' \hat{\Psi}^\dagger(x) \hat{\Psi}^\dagger(x') \delta(x - x') \hat{\Psi}(x') \hat{\Psi}(x), \quad (2.5)$$

with $g = \frac{4\pi\hbar^2 a}{m}$. Finally, considering the tight-binding approximation due to the Wannier functions localization, the Hamiltonian in second quantization is expressed as follows:

$$\hat{H} = -J \sum_{\langle i,j \rangle} (\hat{b}_i^\dagger \hat{b}_j + \hat{b}_j^\dagger \hat{b}_i) + \frac{U}{2} \sum_i \hat{n}_i (\hat{n}_i - 1) - \mu \sum_i \hat{n}_i, \quad (2.6)$$

this expression is known as the Bose-Hubbard model. The first term, commonly known as the hopping term, describes the tunneling between neighboring sites. The hopping rate J quantifies the probability that a particle moves to its nearest site. This rate is considered equal for all sites within the lattice and is characterized by the amplitude

$$-J = \int dx W_i^*(x) \left(-\frac{\hbar^2 \nabla^2}{2m} + V_{\text{lat}}(x) \right) W_j(x). \quad (2.7)$$

The second term in Eq. (2.6) represents the contact interaction, where $\hat{n}_i = \hat{b}_i^\dagger \hat{b}_i$ denotes the occupation number operator at the i -th site. This term is characterized by the interaction strength U given by:

$$U = g \int dx |W(x)|^4. \quad (2.8)$$

Finally, we include the last term to situate our system within a grand canonical ensemble, allowing the system to adjust the number of particles when needed in order to minimize the energy. Here, μ represents the chemical potential, which corresponds to the energy required to add or remove a particle from the lattice.

2.2 Superfluid-Mott Insulator transition

At ultralow temperatures, close to absolute zero, where thermal fluctuations become less relevant, quantum fluctuations begin to dominate, potentially inducing phase transitions in the ground state of the system by altering its parameters [27]. In the Bose-Hubbard model, the parameters typically are rescaled in terms of U as the energy unit, i.e., $\overline{J} = \frac{J}{U}$ and $\overline{\mu} = \frac{\mu}{U}$. When the relative variation of these two competitive terms crosses a critical value, a phase transition occurs. Consequently, a competition arises between the hopping or kinetic energy and the interaction, leading to the division of the physics described by the Bose-Hubbard model into two distinct phases: the Mott-Insulator and the Superfluid.

2.2.1 Mott-Insulator phase $J \ll U$

This phase occurs when the interactions are significantly stronger than the kinetic energy, i.e., when $J \ll U$. In this scenario, due to the strong interactions, the particles encounter difficulties in tunneling to neighboring sites. Consequently, the number of particles per site is fixed, the wavefunctions of the system are highly localized in coordinates representation, and generally, the ground state can be described as the tensor product of Fock states at each lattice site,

$$|\psi_{\text{MI}}\rangle \propto \bigotimes_i^L \left(\hat{b}_i^\dagger\right)^n |\emptyset\rangle, \quad (2.9)$$

where n is the number of particles in each site and $|\emptyset\rangle$ is the vacuum state. The phases are appropriately described within the plane $(\bar{\mu}, \bar{J})$, which is constructed by finding the ground state wave function, followed by evaluation of the observables that characterize them. These include the expected value of the number operator $\langle \hat{n} \rangle$ and its standard deviation $\langle \Delta \hat{n}^2 \rangle = \sum_i \langle \hat{n}_i^2 \rangle - \langle \hat{n} \rangle^2$. In the case of the Mott-Insulator phase, it is clear that due to the fixed number of particles per site the variance vanishes $\langle \Delta \hat{n}^2 \rangle = 0$. The phase diagram can be derived using various techniques such as Density-Matrix Renormalization Group (DMRG) [59], Padé analysis of the series [60], Quantum Monte Carlo (QMC) [61], among others. These methods are illustrated in Fig. 2.1, which illustrates the region with unit occupation in the Mott insulator lobe, surrounded by the superfluid phases.

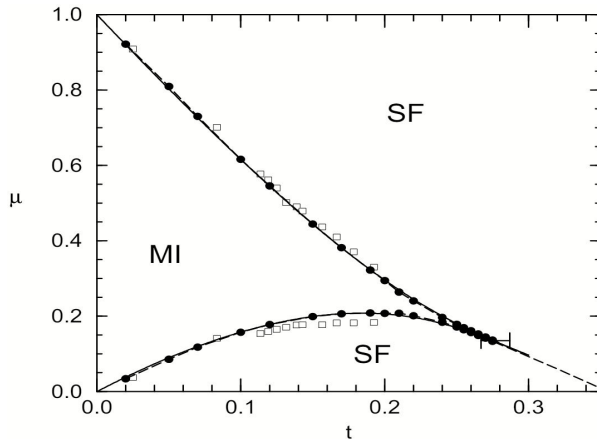


Figure 2.1: Phase diagram of the Bose-Hubbard model (MI: Mott-insulator with density one, SF:superfluid phase). The solid lines show a Padé analysis of 12th order strong coupling expansions, the boxes show Quantum Monte Carlo data. The circles are the DMRG results ($J \rightarrow t, U = 1$) [59].

2.2.2 Superfluid phase $J \gg U$

This phase occurs when the kinetic energy is significantly greater than the interaction, i.e., when $J \gg U$. In this scenario, the high kinetic energy allows particles to move freely throughout the entire lattice. Consequently, the wavefunctions of the system become highly delocalized in coordinates representation but remain highly localized in momentum space, ensuring that the quasi-momentum of the system is well-defined and long-range coherence is established. Therefore, in this case, the ground state can be expressed as a superposition of all possible occupation states, as follows:

$$|\psi_{\text{SF}}\rangle \propto \left(\sum_i^L \hat{b}_i^\dagger \right)^N |\emptyset\rangle, \quad (2.10)$$

where N is the total number of particles. This state is well described by a Poissonian distribution, such as coherent states, thus it can be demonstrated that $\langle \Delta \hat{n}^2 \rangle = \langle \hat{n} \rangle$, as a consequence, there is always an inherent uncertainty in measuring the number of particles, which may be of the order of the mean value of the number of particles.

The transitions between these two phases were first experimentally observed in 2002 through changes in the periodic lattice potential. Depending on the depth of the potential well, the system exhibits characteristics of one phase or another, as illustrated in Fig. 2.2.

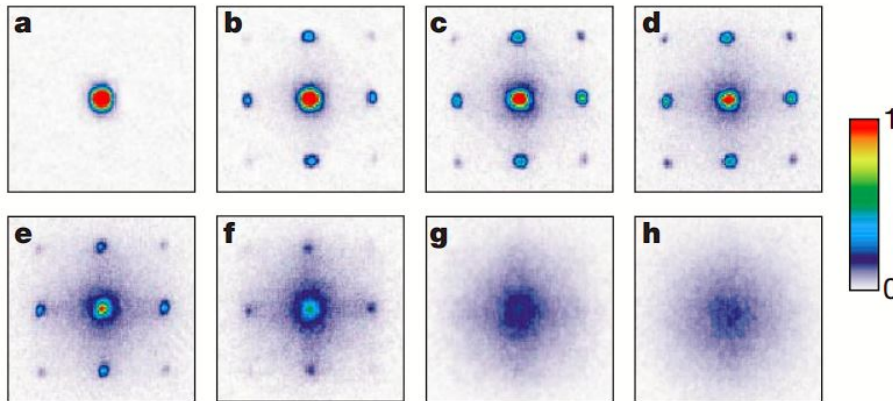


Figure 2.2: Absorption images in momentum space of multiple matter wave interference patterns showing the superfluid to Mott-insulator phase transition. Potential depths increased from 0 to 20 times the initial one. Graph **a** shows the superfluid phase, with high coherence, while in **h** coherence is lost, representing a Mott insulator [27].

In this work, we focus on the superfluid phase with the main objective of developing a numerical method to study the dynamics of one and two spin-1 particles. Therefore, in the following we introduce this degree of freedom into our one-dimensional system, along with external Zeeman fields.

2.3 Spin-1 Bose-Hubbard model

The inclusion of the spin degree of freedom to the system allows to the contact potential describe spinorial interactions [62], which can be explained by theory of addition of angular momenta, in terms of two well-known bases: the first is the coupled basis $|s_1, s_2, F, M\rangle = |F, M\rangle$, where s_i is the spin of the i -th particle, and F and M represent the total spin and magnetic projection of the particles, respectively. The second basis is the uncoupled basis $|s_1, s_2, \sigma_1, \sigma_2\rangle = |\sigma_1, \sigma_2\rangle$, which considers the magnetic projections on the z -axis of each particle independently. Since we aim to describe spin-1 particles, σ_i can take the values $\{-1, 0, 1\}$. The relationship between these two bases is characterized by the usual Clebsch-Gordan coefficients.

2.3.1 Interacting Potential

The scattering processes associated with the total spin of the particles are independent, and due to the bosonic nature of the particles, collisions can only occur in symmetric channels, that is, those corresponding to a total spin $F = \{0, 2\}$. Therefore, using the coupled basis, the interaction can now be expressed as a sum of processes associated with a total spin F as shown in the following expression,

$$\hat{V}_{\text{int}} = \sum_F g_F \hat{P}_F \delta(x - x'), \quad \text{with: } g_F = \frac{4\pi\hbar^2 a_F}{m}, \quad (2.11)$$

where a_F is the scattering length associated with the process involving a total spin F , and $\hat{P}_F = |F, M\rangle\langle M, F|$ is the projector associated to the total spin F . Using the expansion of the coupled basis in terms of the uncoupled one, it is possible to rewrite the projectors as a superposition of the uncoupled basis and compute the new interaction term as in Eq. (2.5). However, it is also possible to write the projectors in terms of spin operators, as detailed in Appendix A, such that

$$\hat{V}_{\text{int}} = \left(c_0 + c_2 \hat{\mathbf{S}}_1 \cdot \hat{\mathbf{S}}_2 \right) \delta(x - x') \quad \text{with: } c_0 = \frac{g_0 + 2g_2}{3} \quad \text{and} \quad c_2 = \frac{g_2 - g_0}{3}. \quad (2.12)$$

In this way, the scattering processes are divided into two types: one that is independent of spin, responsible for what is commonly referred to as *charge scattering*, and another that depends on the spin, proportional to $\hat{\mathbf{S}}_1 \cdot \hat{\mathbf{S}}_2$, responsible for *spin scattering*. Hence expressing the operator in second quantization form

$$\hat{V}_{\text{int}} = \frac{1}{2} \sum_{\{\sigma\}} \int dx \, dx' \hat{\Psi}_{\sigma_1}^\dagger(x) \hat{\Psi}_{\sigma_2}^\dagger(x') \langle \sigma_1, \sigma_2 | \hat{V}_{\text{int}} | \sigma_3, \sigma_4 \rangle \hat{\Psi}_{\sigma_3}(x') \hat{\Psi}_{\sigma_4}(x), \quad (2.13)$$

the interaction term then becomes

$$\hat{H}_I = \frac{U_0}{2} \sum_{i,\sigma} \hat{n}_{i,\sigma} (\hat{n}_{i,\sigma} - 1) + \frac{U_2}{2} \sum_i \left(\hat{\mathbf{F}}_i^2 - 2 \sum_{\sigma} \hat{n}_{i,\sigma} \right), \quad (2.14)$$

where $\hat{\mathbf{F}}_i = (\hat{F}_i^x, \hat{F}_i^y, \hat{F}_i^z)$ is the total spin operator at site i , with $\hat{F}_i^\nu = \sum_{\sigma,\sigma'} \hat{b}_{i,\sigma}^\dagger [\hat{S}^\nu]_{\sigma,\sigma'} \hat{b}_{i,\sigma'}$ being $[\hat{S}^\nu]_{\sigma,\sigma'}$ the matrix elements of the standard spin-1 matrices. $\hat{b}_{i,\sigma}^\dagger$ and $\hat{b}_{i,\sigma}$ are the creation and annihilation operators, respectively, which create and annihilate a particle with magnetic projection σ at site i . The interaction strength in the channel F is denoted as U_F and is defined as

$$U_F = c_F \int dx |W(x)|^4. \quad (2.15)$$

The most commonly used elements for the formation of these ultracold spinor gases are alkali metals. These metals typically have a single valence electron and a nuclear spin of $3/2$ in their most common and stable isotopes. Consequently, this interaction strength also characterizes the type of spinor system we have. For instance, with $U_2 > 0$, the system displays antiferromagnetic behavior, exemplified by ^{23}Na , which has a specific relationship with the charge scattering term, $U_2 = 0.036U_0$ [45]. Conversely, for $U_2 < 0$, as in ^{87}Rb , the system exhibits ferromagnetic properties, which also have a specific interaction strength relationship, $U_2 = -0.004U_0$ [45].

2.3.2 External Fields

Finally, the last term we take into account in our spin-1 Hamiltonian is the coupling to an external magnetic field, which can be expressed in terms of spin-1 operators [63]:

$$\hat{H}_Z = - \sum_i \left[\frac{\mu_B B}{2} \hat{S}_i^z + \frac{\mu_B^2 B^2}{2C_{hyp}} \left(1 - \frac{(\hat{S}_i^z)^2}{4} \right) \right], \quad (2.16)$$

where B is the strength of the field, μ_B the Bohr magneton, and C_{hyp} is the hyperfine constant that couples the electron spin to the nuclear spin. It is well known that the linear Zeeman field contributes more significantly to the total energy of the system compared to the quadratic field [63]. However, because the interaction commutes with the linear contribution, i.e., $\sum_i \hat{S}_i^z$, it does not affect the dynamics of the populations when equally probable magnetic projection samples are considered and therefore, only the quadratic contributions affect in this specific case, that is call the balanced mixture condition . Otherwise, the linear field must be consider, so since we aim to analyze the dynamics of one and two particles, in scenarios where only one particle is present and thus no interaction occurs, the linear contributions of the Zeeman field can significantly influence the system. Hence, these contributions should be considered in our analysis.

Then, the external magnetic field in second quantization takes the form:

$$\hat{H}_Z = D \sum_{i,\sigma} \sigma \hat{n}_{i,\sigma} + Q \sum_{i,\sigma} \sigma^2 \hat{n}_{i,\sigma}, \quad (2.17)$$

with D and Q representing the coupling of each Zeeman field, linear and quadratic, respectively.

These fields may lift the degeneracy of the system by favoring energy minimization for states with different spin magnetic projections, which depends on the sign, strength, and type of the field. For the **linear magnetic field**, if $D = 0$, the system is triply degenerate, and states with magnetic projections $-1, 0$, and 1 minimize the energy equally. Conversely, if $D \neq 0$, the degeneracy is totally lifted: magnetic projection -1 is favored when $D > 0$, and projection 1 is favored when $D < 0$. The effects of this external linear Zeeman field are depicted in Fig. 2.3.

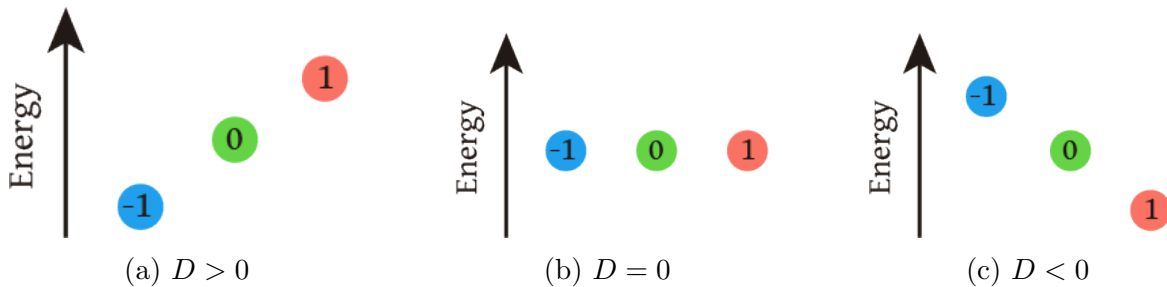


Figure 2.3: Degeneracy of states with magnetic projections $-1, 0$, and 1 as a function of the linear Zeeman strength. (a) Projection -1 minimizes the energy. (b) States are triple degenerate. (c) Projection 1 is favored.

Now, if we consider the **quadratic magnetic field**, when $Q = 0$, the system is also triply degenerate, and if $Q \neq 0$, the degeneracy is partially lifted, equally favoring projections -1 and 1 when $Q > 0$, and favoring projection 0 when $Q < 0$. The effects of this external quadratic Zeeman field are depicted in Fig. 2.4.

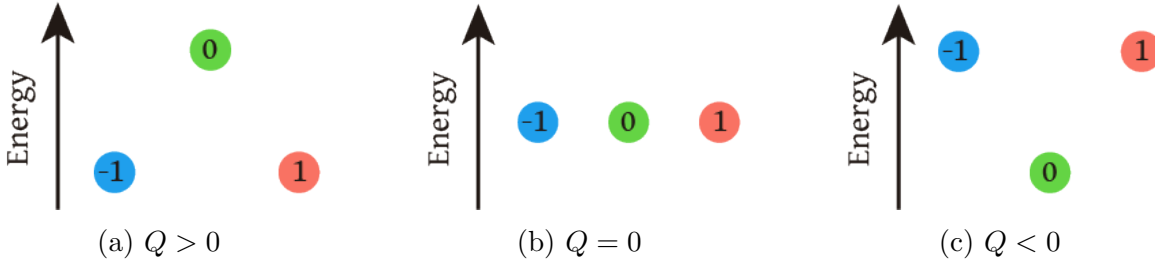


Figure 2.4: Degeneracy of states as a function of the quadratic Zeeman strength. (a) Projections -1 and 1 are favored. (b) States are triple degenerate. (c) Projection 0 minimizes the energy.

Finally, with the addition of the spin-1 degree of freedom to the interaction Eq. (2.14), the hopping term, and the external Zeeman fields Eq. (2.17), we can rewrite the model Eq. (2.6) as the extended spin-1 Bose-Hubbard Hamiltonian as follows:

$$\hat{H} = \underbrace{-J \sum_{\langle i,j \rangle, \sigma} \left(\hat{b}_{i,\sigma}^\dagger \hat{b}_{j,\sigma} + \text{h.c.} \right)}_{\text{Hopping}} + \underbrace{\hat{H}_I}_{\text{Interaction}} - \underbrace{\mu \sum_{i,\sigma} \hat{n}_{i,\sigma}}_{\text{Chemical Potential}} + \underbrace{\hat{H}_Z}_{\text{Zeeman Fields}}. \quad (2.18)$$

As mentioned above, the objective is to describe the dynamics of one and two spin-1 bosons in the presence of the magnetic fields already described. In the next section, a temporal dependence is introduced to these fields, which are periodic in time, hence we aim to approach the solution through Floquet theory (see Chapter 3).

2.4 Building the time-dependent driving Hamiltonian

The dynamics of spin-1 bosons has been relatively understudied in recent years. Nonetheless, the effects of static Zeeman fields, which enhance quantum magnetism [35, 34], are better understood. These fields are known to contribute to energy minimization by favoring states with different magnetic projections of spin, as detailed in the previous section. With this foundation, our current objective is build the Hamiltonian which is going to drive the dynamics of the system, under conditions where these external fields are not static but modulated over time. This analysis includes

both single-particle and two-particle physics when interactions are present.

2.4.1 One particle dynamics

For a single particle, it is understood that no interaction effects are present in the system, allowing both linear and quadratic Zeeman fields to directly influence the single spin. However, for simplicity and to focus our analysis correctly, we consider each Zeeman field independently, applying periodic time dependence specifically to one while excluding it from the other. Consequently, the dynamics of a single particle are analyzed in two distinct scenarios: one with a **linear magnetic field** and another with a **quadratic magnetic field**.

Linear Magnetic Field

In the first scenario, the system is influenced only by the **linear Zeeman field**, as described in the first term of Eq. (2.17), with the field coupling modulated periodically as follows:

$$D \rightarrow D(t) = D_0 \cos^2(\omega t) \text{ with } D_0 > 0. \quad (2.19)$$

This modification dynamically lifts the degeneracy of the system, favoring energy minimization towards the -1 magnetic projection, except near $t = n\pi/2$ where n is an odd number and all magnetic projections are equally favored. The effects of this external periodic linear Zeeman field are illustrated in Figure 2.5.

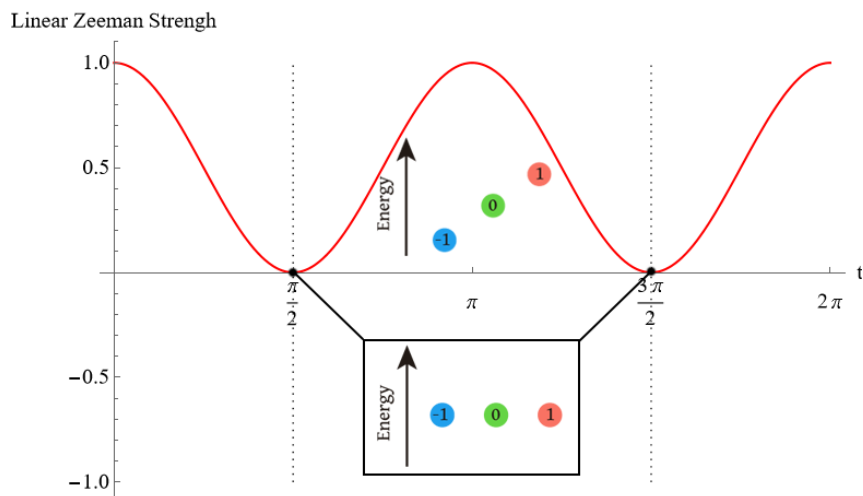


Figure 2.5: Effect of the linear Zeeman field on magnetic projections over time.

Then, with the addition of the periodic **linear magnetic field** we can rewrite the Eq. (2.18) for one particle into a one-dimensional optical lattice as a time-dependent Hamiltonian as follows:

$$\hat{H}(t) = -J \sum_{i,\sigma} \left(\hat{b}_{i,\sigma}^\dagger \hat{b}_{i+1,\sigma} + \hat{b}_{i+1,\sigma}^\dagger \hat{b}_{i,\sigma} \right) - \mu \sum_{i,\sigma} \hat{n}_{i,\sigma} + D_0 \cos^2(\omega t) \sum_{i,\sigma} \sigma \hat{n}_{i,\sigma}. \quad (2.20)$$

Quadratic Magnetic Field

In the second scenario, the system is governed by the **quadratic Zeeman field**, as specified in the second term of Eq. (2.17), with the field coupling also modulated periodically:

$$Q \rightarrow Q(t) = Q_0 \cos^2(\omega t) \text{ with } Q_0 > 0. \quad (2.21)$$

This modification causes the quadratic field to partially lift the degeneracy of the system dynamically, favoring energy minimization towards magnetic projections 1 and -1. Similar to the linear field scenario, this preference decreases near $t = n\pi/2$, where n is an odd number and all magnetic projections are equally favored. The effects of this external periodic quadratic Zeeman field are depicted in Figure 2.6.

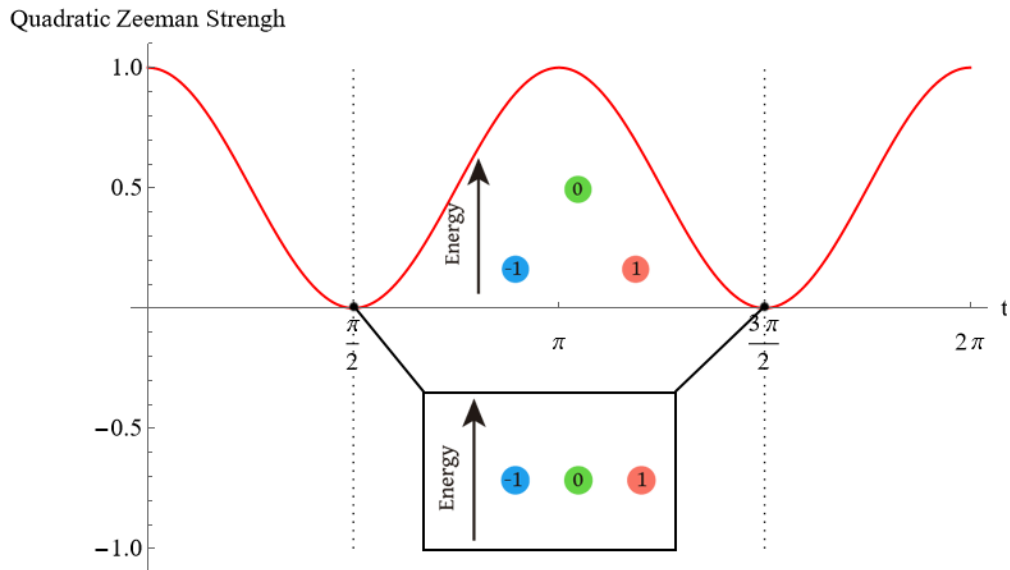


Figure 2.6: Effect of the quadratic Zeeman field on magnetic projections over time.

Then, with the addition of the periodic **quadratic magnetic field** we can rewrite the Eq. (2.18) for one particle into a one-dimensional optical lattice as a time-dependent Hamiltonian as follows:

$$\hat{H}(t) = -J \sum_{i,\sigma} \left(\hat{b}_{i,\sigma}^\dagger \hat{b}_{i+1,\sigma} + \hat{b}_{i+1,\sigma}^\dagger \hat{b}_{i,\sigma} \right) - \mu \sum_{i,\sigma} \hat{n}_{i,\sigma} + Q_0 \cos^2(\omega t) \sum_{i,\sigma} \sigma^2 \hat{n}_{i,\sigma}. \quad (2.22)$$

2.4.2 Two particles dynamics

In the case of two particles, interactions within the system become significant, and as shown in Eq. (2.12), these interactions can be categorized into two types: charge scattering and spin scattering. These two types of scattering are related with the three degrees of freedom present in the system: *charge*, *spin*, and *quadrupole* [64].

The first degree of freedom, *charge*, is mainly related to the density of the particles and the possibility of the particles occupying a specific location in the lattice or existing in a superposition of locations. The second, *spin*, represents the typical intrinsic internal degree of freedom of all particles, whose effects were first observed in the Stern-Gerlach experiment in 1922 [65]. The third, *quadrupole*, is another internal degree of freedom similar to spin, but appears only in spin 1 systems or higher. For $S = 1$, its origins are linked to the SU(3) symmetry [66], a topic that is explored further in the next section.

On the other hand, the second term of the interaction, as expressed in Eq. (2.14), comprise two implicit processes: spin-preserving and spin changing. These can be analyzed explicitly by considering the identity of the total spin operator at site i , $\hat{\mathbf{F}}_i^2 = \frac{1}{2}(\hat{S}_i^- \hat{S}_i^+ + \hat{S}_i^+ \hat{S}_i^-) + (\hat{S}_i^z)^2$ together with the Schwinger boson formalism thus allowing a comprehensive representation of spin interactions, as detailed in Appendix A.

Therefore, the total spin operator at site i , $\hat{\mathbf{F}}_i^2$, can be reformulated as follows:

$$\begin{aligned} \hat{\mathbf{F}}_i^2 &= (\hat{n}_{i,1} - \hat{n}_{i,-1})^2 + \hat{n}_{i,1} + 2\hat{n}_{i,0} + \hat{n}_{i,-1} + 2(\hat{n}_{i,1}\hat{n}_{i,0} + \hat{n}_{i,0}\hat{n}_{i,-1}) \\ &\quad + 2 \left(\hat{b}_{i,1}^\dagger \hat{b}_{i,-1}^\dagger \hat{b}_{i,0} \hat{b}_{i,0} + \hat{b}_{i,0}^\dagger \hat{b}_{i,0}^\dagger \hat{b}_{i,1} \hat{b}_{i,-1} \right), \end{aligned} \quad (2.23)$$

this representation of the total spin operator reveals two distinct types of collisions in the system. Figure 2.7 schematically illustrates these processes: **a)** two incoming particles (top) interact (crossing lines) and result in two outgoing particles (bottom) with the same spin projection, hence,

we term this a spin-preserving collision. **b)** In the second scenario, represented by a black dot, a spin-changing collision occurs, where the interaction between the initial particles results in two particles with altered spin projections. This process, induced by the last two terms of Eq (2.23), involves a mixing between the $\sigma = \pm 1$ and 0 states, known as *spin mixing* [45], which enriches the physics of this model compared with spinless models. However, it is important to note that a key constraint must be satisfied: the total spin projection must be conserved before and after each interaction, such that $\sigma_1 + \sigma_2 = \sigma_3 + \sigma_4$.

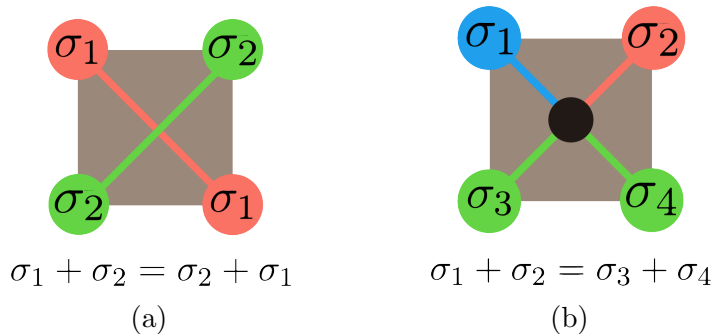


Figure 2.7: Two different spin-1 interactions, with a) spin preserving collision and b) spin changing collision.

Now, taking into account the types of collisions and under the balance mixture condition, the role of an external Zeeman field is mainly influenced by the quadratic contribution. Consequently, the dynamics of two particles in this context is governed by the quadratic Zeeman field, as specified in Eq. (2.17), with the coupling of the field modulated periodically as specified in Eqs. (2.21).

The inclusion of this quadratic field initially favors the -1 and 1 projections, as shown in Fig. 2.4. However, spin-changing collisions complicates the impact of this field on the system, particularly when it is modulated. Despite this complexity, studies have demonstrated that in a three-dimensional optical lattice with a constant field, the influence of the field significantly affects spin mixing [45], as illustrated in Fig 2.8.

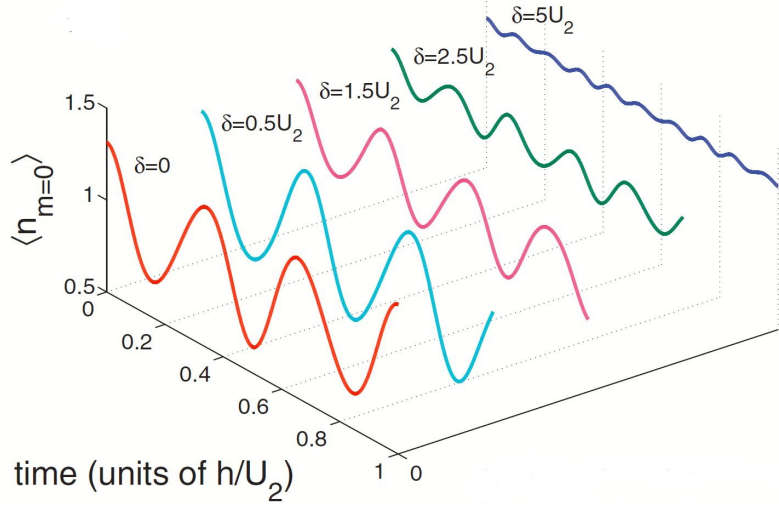


Figure 2.8: Spin-mixing oscillations in the presence of a magnetic field in the form of a quadratic Zeeman shift. Panel shows the population in $m = 0$ as a function of hold time for several values of the quadratic Zeeman shift($Q \rightarrow \delta$) [45].

Then with reformulation of the spin total operator of the Eq. (2.23) and the addition of the periodic quadratic Zeeman field we can rewrite the Eq. (2.18) for two particles as a time-dependent Hamiltonian as follows:

$$\begin{aligned} \hat{H} = & -J \sum_{i,\sigma} \left(\hat{b}_{i,\sigma}^\dagger \hat{b}_{i+1,\sigma} + \hat{b}_{i+1,\sigma}^\dagger \hat{b}_{i,\sigma} \right) - (\mu + U_2) \sum_{i,\sigma} \hat{n}_{i,\sigma} + Q_0 \cos^2(\omega t) \sum_{i,\sigma} \sigma^2 \hat{n}_{i,\sigma} \\ & + \frac{U_0}{2} \sum_{i,\sigma} \hat{n}_{i,\sigma} (\hat{n}_{i,\sigma} - 1) + \frac{U_2}{2} \sum_i \hat{\mathbf{F}}_i^2. \end{aligned} \quad (2.24)$$

The Hamiltonians in Eqs. (2.20), (2.22) and (2.24) now satisfy $\hat{H}(t) = \hat{H}(t + T)$, where $T = 2\pi/\omega$, rendering them periodic in time. This periodicity is a crucial property that is exploited in the chapter 3 using Floquet theory. However, before applying this technique, it is essential to understand the type of information that can be extracted from the system. Therefore, the next section provides a comprehensive overview of the entire description for a single quantum spin-1.

2.5 Single Spin-1 Characterization

In this section, we discuss the fundamental components to characterize a single spin-1 system. We begin by introducing the generators of the associated Hilbert space, then we proceed to describe arbitrary spin-1 states. Subsequently we also explore the different bases that can be used to represent the system. Finally, we provide an overview of the various observables that can be used to extract information about our system.

2.5.1 SU(2) Description

To determine the potential observables that can provide relevant information about our spin-1 system, it is essential to understand the symmetry group that governs the system. For spin- $\frac{1}{2}$ systems, the associated symmetry group is represented by the 2-dimensional representation of the SU(2) group, with its generators being the Pauli matrices [67]:

$$\sigma^x = \begin{pmatrix} 0 & 1 \\ 1 & 0 \end{pmatrix}, \quad \sigma^y = \begin{pmatrix} 0 & -i \\ i & 0 \end{pmatrix}, \quad \sigma^z = \begin{pmatrix} 1 & 0 \\ 0 & -1 \end{pmatrix}. \quad (2.25)$$

For spin-1 systems, they can also be described by the SU(2) group, but with a 3-dimensional representation, providing the typical spin-1 matrices:

$$S^x = \frac{1}{\sqrt{2}} \begin{pmatrix} 0 & 1 & 0 \\ 1 & 0 & 1 \\ 0 & 1 & 0 \end{pmatrix}, \quad S^y = \frac{1}{\sqrt{2}} \begin{pmatrix} 0 & -i & 0 \\ i & 0 & -i \\ 0 & i & 0 \end{pmatrix}, \quad S^z = \begin{pmatrix} 1 & 0 & 0 \\ 0 & 0 & 0 \\ 0 & 0 & -1 \end{pmatrix}, \quad (2.26)$$

where both representations satisfy the Lie algebra $[\hat{S}^\alpha, \hat{S}^\beta] = i\epsilon_{\alpha\beta\gamma}\hat{S}^\gamma$. These representations are constructed from a complete set of commuting observables (CSCO), which in this case are $\{\hat{S}^2, \hat{S}^z\}$, providing a basis for different representations $|S, \sigma\rangle$ where $-S \leq \sigma \leq S$, and give us the typical information about the magnetic density $\langle \hat{S}^z \rangle$, transverse magnetization $|\langle S^x \rangle|^2$ among others.

Thus, describing spin-1 particles requires at least a 3-dimensional representation or 3-dimensional matrices to account for all magnetic projections. Notably, the fundamental representation of SU(3) is also 3-dimensional, which enables us to obtain a SU(3) representation of spin-1, yielding additional generators that provide more information than the 3-dimensional representation of SU(2) does.

2.5.2 SU(3)-Bosonic Representation of a Spin-1

The U(N) group consists of all $N \times N$ matrices that satisfy the *unitary* condition, i.e., $U^\dagger U = I$, and therefore comprises N^2 elements, then to generate any matrix within this group, N^2 independent generators are required. The SU(N) group, a subgroup of U(N), consists of all $N \times N$ unitary matrices with the additional *special* condition that their determinant must be equal to one. This additional condition reduces the number of independent generators to $N^2 - 1$. For SU(3), this results in eight independent generators that can provide additional information about the system, unlike SU(2), which has only three generators.

Any Hermitian operator \hat{O} acting in the associated Hilbert space can be decomposed as $\hat{O} = \sum_{\alpha,\beta=1}^3 A_{\alpha\beta} |\alpha\rangle\langle\beta|$, where $|1\rangle$, $|2\rangle$, and $|3\rangle$ are states from an arbitrary basis of the Hilbert space, with real matrix elements satisfying $A_{\alpha\beta}^* = A_{\beta\alpha}$ [64]. These eight independent operators can be constructed using the *spherical tensor operator*, defined as an operator whose components satisfy the following commutation relations:

$$\begin{aligned} [\hat{S}^z, \hat{T}_q^{(k)}] &= q \hat{T}_q^{(k)}, \\ [\hat{S}^\pm, \hat{T}_q^{(k)}] &= \sqrt{k(k+1) - q(q \pm 1)} \hat{T}_{q \pm 1}^{(k)}, \end{aligned} \quad (2.27)$$

where k is the rank of the tensor, and q indexes its $2k + 1$ elements ($q \in [-k, k]$). It can be straightforwardly shown that for $k = 0$, the operator that fulfills the conditions is the identity. However, since we are seeking non-trivial independent physical operators, the identity is not part of the Lie algebra. For $k = 1$, this yields the first three non-trivial, independent physical operators, which are \hat{S}^+ , \hat{S}^- , and \hat{S}^z . For $k = 2$, it produces the five remaining generators, which are:

$$\begin{aligned} \hat{T}_0^{(2)} &= \frac{1}{\sqrt{3}} \left(3 \left(\hat{S}^z \right)^2 - S(S+1) \right), \\ \hat{T}_{\pm 1}^{(2)} &= \frac{1}{\sqrt{2}} \{ \hat{S}^\pm, \hat{S}^z \}, \\ \hat{T}_{\pm 2}^{(2)} &= \frac{1}{\sqrt{2}} \left(\hat{S}^\pm \right)^2. \end{aligned} \quad (2.28)$$

Suitable linear combinations of the eight \hat{T} operators result in eight Hermitian operators that generate our local Hilbert space. Any operator can be constructed from their superposition:

$$\begin{aligned}\hat{\Lambda}^1 &= \hat{S}^x, \quad \hat{\Lambda}^2 = \hat{S}^y, \quad \hat{\Lambda}^3 = \hat{S}^z, \\ \hat{\Lambda}^4 &= \{\hat{S}^x, \hat{S}^z\}, \quad \hat{\Lambda}^5 = \{\hat{S}^y, \hat{S}^z\}, \quad \hat{\Lambda}^6 = \{\hat{S}^x, \hat{S}^y\}, \\ \hat{\Lambda}^7 &= (\hat{S}^y)^2 - (\hat{S}^x)^2, \quad \hat{\Lambda}^8 = \sqrt{3}(\hat{S}^z)^2 - \frac{2}{\sqrt{3}}\hat{I},\end{aligned}\tag{2.29}$$

where they meet the SU(3) algebra, as detailed in Appendix A. Thus, we may arrange these operators conveniently in the following vectorial form:

$$\hat{\mathbf{S}}_i = \begin{pmatrix} \hat{\Lambda}_i^1 \\ \hat{\Lambda}_i^2 \\ \hat{\Lambda}_i^3 \end{pmatrix} = \begin{pmatrix} \hat{S}_i^x \\ \hat{S}_i^y \\ \hat{S}_i^z \end{pmatrix}, \quad \hat{\mathbf{Q}}_i = \begin{pmatrix} \hat{\Lambda}_i^4 \\ \hat{\Lambda}_i^5 \\ \hat{\Lambda}_i^6 \\ \hat{\Lambda}_i^7 \\ \hat{\Lambda}_i^8 \end{pmatrix} = \begin{pmatrix} \{\hat{S}_i^x, \hat{S}_i^z\} \\ \{\hat{S}_i^y, \hat{S}_i^z\} \\ \{\hat{S}_i^x, \hat{S}_i^y\} \\ (\hat{S}_i^y)^2 - (\hat{S}_i^x)^2 \\ \sqrt{3}(\hat{S}_i^z)^2 - \frac{2}{\sqrt{3}}\hat{I} \end{pmatrix},\tag{2.30}$$

where the first vector is associated with the magnetic nature, represented by the spin operator, and the second one is related to the quadrupolar nature, denoted as the *quadrupolar operator* [64]. Notice that although $\hat{\mathbf{Q}}$ is referred to as a vector, it is actually a tensor defined by $\hat{Q}^{ij} = \hat{S}^i \hat{S}^j + \hat{S}^j \hat{S}^i - \frac{S(S+1)}{3} \delta_{ij}$. For convenience, we choose to arrange its independent components as specified in Eq. (2.30) [68]. In fact, these two vector operators are related with the conventional generators of SU(3), the Gell-Mann matrices ($\hat{\lambda}^a$) [69], so that $\hat{\mathbf{S}} = (\hat{\lambda}^7, -\hat{\lambda}^5, \hat{\lambda}^2)$ and $\hat{\mathbf{Q}} = -(\hat{\lambda}^1, \hat{\lambda}^3, \hat{\lambda}^4, \hat{\lambda}^6, -\hat{\lambda}^8)$. This arrangement underscores a strong connection between the generators of SU(3) and the physical quantities of interest in our system.

Therefore, apart from spin ordering, a system of local spin-1 particles inherently possesses the capacity to also exhibit a quadrupolar order [68, 66]. The competition between these two vectorial order parameters, $\hat{\mathbf{S}}$ and $\hat{\mathbf{Q}}$, is reflected in the following equality that is valid for an arbitrary spin-1 state [64]:

$$\sum_{a=1}^8 \langle \hat{\Lambda}^a \rangle^2 = \langle \hat{\mathbf{S}} \rangle^2 + \langle \hat{\mathbf{Q}} \rangle^2 = \frac{4}{3},\tag{2.31}$$

and its value is directly related to the quadratic Casimir operator of SU(3), specifically being its eigenvalue (see Appendix A)[70]. Thus, as a consequence of the nature of spin-1, it is necessary to introduce appropriate bases that allow extracting relevant physical information from both the spin and the quadrupole [68].

2.5.3 Spin-1 Basis

The choice of a basis for representing a system, whether discrete or continuous, is crucial for both extracting specific types of information and for the effective application of the numerical techniques described in the following chapter. This section presents a summary of the most commonly used bases, including Cartesian and magnetic bases, as well as an overview to spin-1 coherent states and quadrupole states.

Magnetic Basis

The most common basis to represent any spin state is given by eigenstates of the \hat{S}^z operator which tell us that our quantization axis is the z -axis. Here, the eigenstates comprise the 3 states in the following order,

$$\mathcal{B}_m = \{|1\rangle, |-1\rangle, |0\rangle\}, \quad (2.32)$$

forming what we denote here as the “magnetic” basis illustrated in Fig. (2.9) by using spin coherent states representation [64].

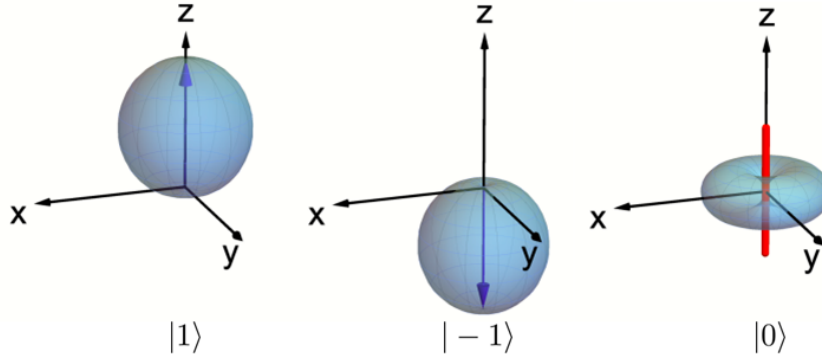


Figure 2.9: Usual, “magnetic” basis for a spin-1 system, formed by eigenstates of \hat{S}^z . States $|1\rangle$, and $|-1\rangle$, have a finite spin-dipole moment (blue arrow). Meanwhile, the state, $|0\rangle$, has a quadrupolar magnetic moment, which can be represented through a director (red bar), perpendicular to the plane of the quadrupole. States are represented as probability surfaces through the spin coherent states [68].

More generally, any spin-1 state can be described through a linear superposition of the states of \mathcal{B}_m ,

$$|\psi\rangle = c_1|1\rangle + c_2|-1\rangle + c_3|0\rangle, \quad (2.33)$$

the coefficients of the superposition are generally arbitrary complex numbers, but imposing a normalization condition and considering the overall phase, it can be demonstrated that any state of a spin-1 particle can be fully described using just four real numbers [64]. It's important to note that while the states $|1\rangle$ and $| - 1\rangle$ exhibit a magnetic nature characterized by a finite spin-dipole moment, the state $|0\rangle$ does not demonstrate this property,

$$\langle 0 | \hat{S}^x | 0 \rangle = \langle 0 | \hat{S}^y | 0 \rangle = \langle 0 | \hat{S}^z | 0 \rangle = 0, \quad (2.34)$$

in this instance, the state $|0\rangle$ cannot support a dipole moment [68]. On the other hand, if we look at the other generators of the group, some of them indeed exhibit this quadrupole magnetic moment,

$$\langle 0 | \hat{\Lambda}^8 | 0 \rangle = -\frac{2}{\sqrt{3}}, \quad (2.35)$$

implying that $\hat{\Lambda}^8$ has a quadrupolar nature. Therefore, one of the distinctive characteristics that differentiates spin-1 particles from spin-1/2 particles is the potential existence of a finite quadrupole moment at a single site. This peculiarity makes spin-1 particles excellent candidates for illustrating magnetism rooted in higher-order moments, as well as atypical and unique quantum phases [64, 68]. For this reason, to effectively highlight the quadrupole nature, it is advisable to work with alternative bases, such as the Cartesian base.

Cartesian Basis

Although the magnetic basis is often predominantly used for the description of spinor systems, this choice of basis is not unique. Any linear combination that forms three orthogonal states can be used to represent the system. Therefore, one alternative is the base known as the *Cartesian basis* [71]:

$$\mathcal{B}_c = \{|x\rangle, |y\rangle, |z\rangle\}, \quad (2.36)$$

where its superpositions are expressed as follows:

$$\begin{aligned} |x\rangle &= \frac{i}{\sqrt{2}}(|1\rangle - | - 1\rangle), \\ |y\rangle &= \frac{1}{\sqrt{2}}(|1\rangle + | - 1\rangle), \\ |z\rangle &= -i|0\rangle, \end{aligned} \quad (2.37)$$

likewise the magnetic basis, the Cartesian can be illustrated using coherent states as shown in the Fig. 2.10.

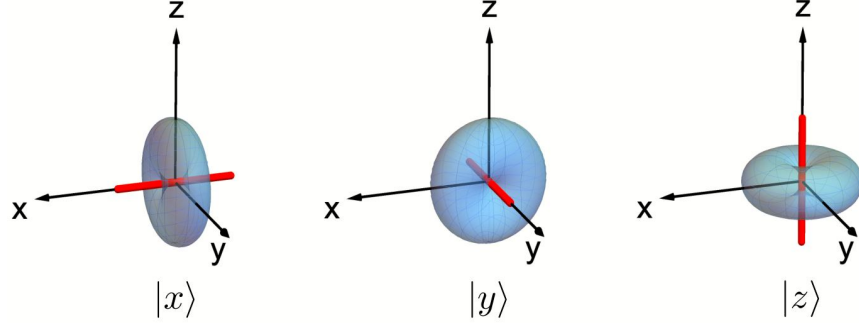


Figure 2.10: Cartesian basis for a spin-1 moment. The three states exhibit a characteristic “doughnut-shaped” profile of spin fluctuations characteristic of a quadrupolar nature [68].

In particular, some authors define this basis with an extra factor of i (e.g., $|\tilde{x}\rangle = -i|x\rangle$) [72], however, this does not affect any physical property and is done for convenience. From Eq. (2.37), we can extract the transformation matrix to relate \mathcal{B}_c and \mathcal{B}_m . Thus, we define

$$\mathcal{U}_{m \rightarrow c} = \begin{pmatrix} \frac{i}{\sqrt{2}} & \frac{1}{\sqrt{2}} & 0 \\ -\frac{i}{\sqrt{2}} & \frac{1}{\sqrt{2}} & 0 \\ 0 & 0 & -i \end{pmatrix}. \quad (2.38)$$

This is the transformation matrix that goes from the magnetic basis to the Cartesian basis, where we have assumed the order $|1\rangle, |-1\rangle, |0\rangle$ for the magnetic basis. Similarly, we can express a general spin-1 state as a linear superposition of the elements defined in Eq. (2.37). Thus, $|\psi\rangle$ must be expressed as

$$|\psi\rangle = c_1|x\rangle + c_2|y\rangle + c_3|z\rangle, \quad (2.39)$$

with complex coefficients c_j . However, as mentioned before, a general normalized wavefunction with a fixed phase can be characterized by four real parameters. Therefore, a general spin-1 state can be written as

$$|\psi\rangle = e^{i\alpha} \sin \theta \cos \varphi |x\rangle + e^{i\beta} \sin \theta \sin \varphi |y\rangle + \cos \theta |z\rangle, \quad (2.40)$$

where $\{\theta, \phi\} \in [0, \pi/2]$ and $\{\alpha, \beta\} \in [0, 2\pi]$ [64]. This basis is also known as the *time-reversal invariant basis* [68], as any state formed by a superposition within this basis remains invariant under the action of the time-reversal operator, $\mathcal{T}|\psi\rangle = |\psi\rangle$. This is because \mathcal{T} changes the sign of

$|0\rangle$ and interchanges $|1\rangle$ with $| - 1\rangle$, i.e., $\mathcal{T}|0\rangle = -|0\rangle$, $\mathcal{T}|1\rangle = | - 1\rangle$ and $\mathcal{T}| - 1\rangle = |1\rangle$, along with the complex conjugation of the associated amplitudes.

Another interesting feature of this basis is that the action of the spin operators can be expressed concisely.

$$\hat{S}^\alpha|\beta\rangle = i \sum_{\gamma=x,y,z} \varepsilon_{\alpha\beta\gamma}|\gamma\rangle, \quad (2.41)$$

consequently, the basis elements are zero eigenvalue eigenstates of the corresponding spin operators,

$$\hat{S}^x|x\rangle = \hat{S}^y|y\rangle = \hat{S}^z|z\rangle = 0. \quad (2.42)$$

Having introduced the magnetic and Cartesian bases, it is useful to introduce two types of states that allow us to explore the limiting cases of spin-1 states: the coherent states and the quadrupolar states.

Spin coherent states

A spin coherent state $|\Omega\rangle$ is a state in which the spin length is maximal, i.e., $(\langle\Omega|\hat{S}|\Omega\rangle)^2 = S^2$. Such a state describes a spin pointing in the direction of the unit vector Ω and is fully characterized by the polar angles $\{\theta, \phi\}$ [64]. Hence,

$$\langle\Omega|\hat{S}|\Omega\rangle = S\Omega = S \begin{pmatrix} \sin\theta\cos\varphi \\ \sin\theta\sin\varphi \\ \cos\theta \end{pmatrix}, \quad (2.43)$$

where $\theta \in [0, \pi]$ and $\varphi \in [0, 2\pi)$. The coherent spin state $|\Omega\rangle$ is furthermore an eigenstate of the spin component parallel to the vector Ω , meaning $(\Omega \cdot \hat{\mathbf{S}})|\Omega\rangle = S|\Omega\rangle$.

In fact, for the spin-1 case, the coherent spin states may conveniently be written as a superposition of the magnetic basis in the form [64]:

$$|\Omega\rangle = \frac{1 + \cos\theta}{2}e^{-i\varphi}|1\rangle + \frac{\sin\theta}{\sqrt{2}}|0\rangle + \frac{1 - \cos\theta}{2}e^{i\varphi}| - 1\rangle, \quad (2.44)$$

and they obey the completeness relation

$$\hat{I} = \frac{3}{4\pi} \int_0^\pi \int_0^{2\pi} d\varphi d\theta \sin\theta |\Omega\rangle\langle\Omega|, \quad (2.45)$$

which makes coherent states form an overcomplete basis. Applying this completeness relation to an arbitrary spin-1 state $|\psi\rangle$, we can find:

$$|\psi\rangle = \hat{I}|\psi\rangle = \frac{3}{4\pi} \int_0^\pi \int_0^{2\pi} d\varphi d\theta \sin \theta \langle \Omega | \psi \rangle | \Omega \rangle, \quad (2.46)$$

Hence, we can see that $|\psi\rangle$ can be expressed as a superposition of coherent spin states. This result allows for a pictorial representation of any arbitrary spin-1 state, as previously shown in Figs. 2.9 and 2.10.

Quadrupolar states

On the other hand, the quadrupolar states $|\mathbf{d}\rangle$, contrary to the coherent states, are those in which the corresponding spin length is equal to zero, namely,

$$\langle \langle \mathbf{d} | \hat{\mathbf{S}} | \mathbf{d} \rangle \rangle^2 = 0, \quad (\mathbf{d} \cdot \hat{\mathbf{S}}) | \mathbf{d} \rangle = 0. \quad (2.47)$$

Nevertheless, as seen in Fig. 2.9, the spin fluctuations exhibit anisotropy, which confines the state to a plane perpendicular to an axis known as the director [64]. Therefore, a quadrupolar state is fully characterized by the polar angles θ, φ defining the unit vector \mathbf{d} as follows:

$$\mathbf{d} = \begin{pmatrix} d_x \\ d_y \\ d_z \end{pmatrix} = \begin{pmatrix} \sin \theta \cos \varphi \\ \sin \theta \sin \varphi \\ \cos \theta \end{pmatrix}, \quad (2.48)$$

which points along the director axis. In particular, quadrupolar states can be conveniently written using the Cartesian basis,

$$|\mathbf{d}\rangle = d_x|x\rangle + d_y|y\rangle + d_z|z\rangle, \quad (2.49)$$

where d_i are the components of Eq. (2.48). This form reveals the nematic nature of a quadrupolar state, i.e., the quadrupolar states characterized by $|\mathbf{d}\rangle$ and $-|\mathbf{d}\rangle$ are physically equivalent, meaning it defines an axis without direction [68]. Bearing this in mind, the quadrupolar states are characterized by \mathbf{d} , which we refer to as the director, rather than the axis along which it points [64].

One interesting feature about these states is that every quadrupolar state, when depicted as a probability surface, assumes a doughnut shape, as illustrated in Fig. 2.10, characterized by a vector director defined in Eq. (2.48). In contrast, coherent states exhibit a “globe-like” appearance, shown

in Fig. 2.8. These two states, coherent spin states and quadrupolar states constitute the extremes of possible states for a spin-one system. However, a typical spin-one state simultaneously exhibits distinct spin and quadrupolar characteristics, as detailed in Eq. (2.31). It's important to note that these states are defined by four independent real parameters, making the specification of just the length and direction of the spin vector insufficient for uniquely determining a physical state.

2.5.4 Physical Observables

Once the generators of the associated Hilbert space and the different bases for representation have been analyzed, it becomes feasible to identify several candidates for physical observables. These observables can provide various types of relevant information for analyzing the magnetic and quadrupole nature of the system either statically or dynamically, where the latter is of great interest in this work.

The first three candidates are clearly the number of atoms per lattice site in each spin component, namely,

$$\{\langle \hat{n}_{i,1} \rangle, \langle \hat{n}_{i,-1} \rangle, \langle \hat{n}_{i,0} \rangle\}, \quad (2.50)$$

which can be detected either *in situ* [73] or, after the release of the atoms from the lattice, by the Stern-Gerlach separation method where the spin states are first spatially separated and then detected [74].

Other possible operators that can provide information about the system are found among the generators. However, not all generators provide relevant physical information. To determine those relevant generators, it is useful to look at those that form a *Cartan Subalgebra* [70] which are called *Cartan operators*. A Cartan Subalgebra \mathfrak{h} is a subalgebra within the Lie algebra of the group, characterized by being a commuting subalgebra. Namely,

$$\forall \hat{\Lambda}^a, \hat{\Lambda}^b \in \mathfrak{h} : [\hat{\Lambda}^a, \hat{\Lambda}^b] = 0, \quad (2.51)$$

the importance of the Cartan subalgebra is that all its members can be diagonalized simultaneously. This means that they form a complete set of commuting observables, and therefore their eigenvalues are physical quantities that can be measured in the laboratory.

In the case of SU(3), the Cartan operators are $\hat{\Lambda}_3$ and $\hat{\Lambda}_8$, which correspond to two quantities called the *magnetic density* $\langle \hat{S}^z \rangle$ and the *quadrupolar density* $\langle \hat{Q}^d \rangle$ respectively, which can be written in

terms of number operators of the magnetic projections as:

$$\begin{aligned}\hat{S}_i^z &= \hat{n}_{i,1} - \hat{n}_{i,-1}, \\ \hat{Q}_i^d &= \frac{1}{\sqrt{3}} (\hat{n}_{i,1} + \hat{n}_{i,-1} - 2\hat{n}_{i,0}).\end{aligned}\quad (2.52)$$

These observables, being Cartan operators, can be diagonalized simultaneously, in this case within the magnetic basis. The eigenvalues of these operators provide crucial information. For instance, the magnetic density reveals the difference in populations between the $|1\rangle$ and $| - 1\rangle$ states. On the other hand, the quadrupolar density offers insights into the competition between the quadrupolar and magnetic natures. This is achieved by comparing the populations in the $|1\rangle$ and $| - 1\rangle$ states with those in the $|0\rangle$ state, which can fluctuate due to spin-changing collisions, thus revealing the behavior of the quadrupole.

Another interesting observable is the total transverse magnetization at site i , $|\langle \hat{F}_i^x \rangle|^2$, which can provide information about the spin fluctuations in the plane perpendicular to the quantization axis, allowing for the extraction of more comprehensive information about the system and the spin 1 nature. This can also be expressed in terms of creation and annihilation operators using the Schwinger boson formalism. This observable can be measured using Faraday rotation spectroscopy, which allows continuous observation of the spin population in a BEC [75].

Finally, another relation worth analyzing dynamically is the one given by the competition between the spin order and the quadrupolar order, Eq. (2.31) with which it is proven that a spin 1 state presents both orders, and with which it is possible to analyze and connect our system with the SU(3) symmetry group through the quadratic and cubic Casimir operators (see Appendix A).

Having studied all the physics related to spin-1, including its different bases, nature, and observables, to understand the dynamics of the Bose-Hubbard Hamiltonian of spin-1 in more depth, we are now ready to introduce the formalism with which the dynamical problem is addressed. This formalism is the Floquet theory (Chapter 3), which, through its numerical approaches, allows us to evolve the system, revealing the rich physics that arises from the interplay between the internal magnetic and quadrupolar degrees of freedom on time.

Chapter 3

FLOQUET FORMALISM

Floquet theory is both an analytical and numerical formalism used to solve systems of ordinary differential equations subject to periodic time conditions. Its central element is Floquet's theorem, proposed by Gaston Floquet in 1883, which provides the general form of the solutions of the system [47]. In this chapter, Floquet's theorem is first stated, highlighting its main conditions and consequences. Subsequently, it is shown how Floquet's theorem can be understood as the temporal counterpart of Bloch's theorem, referring to the quantities that are discretized in both cases: the quasimomentum and the quasienergies for Bloch and Floquet, respectively. Consequently, the different numerical approaches that Floquet's theorem can take to solve an arbitrary system are formulated, focusing mainly on the extended Hilbert space approach and the expansion in discrete Fourier series. Finally, the problem of the spin-1 Bose-Hubbard Hamiltonian for a single particle in two sites is addressed through Floquet's theorem. These results are compared with those obtained from analytical solutions in momentum space, thus corroborating the validity of the technique to be used in the complete one- and two-particle systems that are analyzed in last chapter.

3.1 Floquet's Theorem

The Floquet's theorem in quantum mechanics can be enunciated in several ways, one of them focuses on the form of the time evolution operator $\hat{U}(t, t_0)$ and its properties at any time and during periodic jumps, emphasizing the Heisenberg picture [76]. The other approach is to use that operator on an arbitrary initial state, providing a general form for the solutions of the system's Hamiltonian, emphasizing the Schrödinger picture [46]. Considering the convenience of using the numerical approach, we express it in the latter form as follows:

Consider a quantum system whose dynamics is governed by a time-periodic Hamiltonian:

$$\hat{H}(t + T) = \hat{H}(t),$$

with driving period T .

The system's evolution state $|\psi_n(t)\rangle$ can be expanded in a complete basis of orthonormal quasi-

stationary states called “*Floquet states*”:

$$|\psi_n(t)\rangle = e^{-\frac{i}{\hbar}\varepsilon_n(t-t_0)}|u_n(t)\rangle, \quad (3.1)$$

where the states $|u_n(t)\rangle$ are called the “*Floquet modes*” and satisfy $|u_n(t+T)\rangle = |u_n(t)\rangle$. The parameter ε_n is called the “*quasienergy*” and n labels the different eigenstates, reflecting the analogy with the quasimomentum k characteristic of Bloch’s theorem in the solid state physics (see Appendix B for supplementary material that deepens Floquet’s theory).

3.1.1 Consequences of Floquet’s Theorem

Floquet’s theorem presents a scenario in which, independent of the Hamiltonian, if it is periodic, a general expression can be given for the evolution of the state $|\psi(t)\rangle$ at any time $t > 0$. This provides a basis to write any initial state $|\psi(0)\rangle$ that subsequently evolves using the time evolution operator. This basis is clearly given by the Floquet modes, which fulfill the typical completeness relation at an arbitrary time, let’s say $t_0 = 0$:

$$\sum_n |u_n(0)\rangle \langle u_n(0)| = \hat{I}, \quad (3.2)$$

Then, we can write any initial state as a superposition of this basis,

$$\begin{aligned} \hat{I}|\psi(0)\rangle &= \sum_n |u_n(0)\rangle \underbrace{\langle u_n(0)|\psi(0)\rangle}_{\equiv c_n}, \\ |\psi(0)\rangle &= \sum_n c_n |u_n(0)\rangle. \end{aligned}$$

Therefore, the state at later times is given by

$$\begin{aligned} |\psi(t)\rangle &= \hat{U}(t, 0)|\psi(0)\rangle, \\ &= \sum_n c_n \hat{U}(t, 0)|u_n(0)\rangle, \\ &= \sum_n c_n |\psi_n(t)\rangle, \\ |\psi(t)\rangle &= \sum_n c_n e^{-\frac{i}{\hbar}\varepsilon_n t} |u_n(t)\rangle. \end{aligned} \quad (3.3)$$

We can see that in this superposition, the coefficients c_n don't depend on time, carrying all dynamics in the Floquet modes $|u_n(t)\rangle$ and the “*Floquet multipliers*”, $e^{-\frac{i}{\hbar}\varepsilon_n t}$. This implies that occupancy probabilities $|c_n|^2$ can be assigned to states that are conserved despite the periodic influence of time, allowing various concepts and techniques used for time-independent quantum systems to be applied to periodically time-dependent systems [56].

In fact, the factor $e^{-\frac{i}{\hbar}\varepsilon_n t}$ in Eq. (3.3) resembles the factors $e^{-\frac{i}{\hbar}E_n t}$ that appear in the temporal evolution of the eigenstates of time-independent Hamiltonians, with E_n being the eigenenergies of the system itself, i.e. resembles to stationary states [77]. Therefore, the quantity ε_n is similar to the energy of the system and were aptly named quasi-energy by physicists Yakov Borisovich Zel'dovich [78] and Vladimir Ivanovich Ritus [79] in 1966, referring also to the aforementioned Bloch theorem.

Now, the problem is to find the respective eigenvalue equation that satisfies the Floquet modes, thus also allowing us to find the quasienergies. This enables us to determine the superposition of the Eq. (3.1) and construct the evolved state at any time t . To achieve this, we start with the time-dependent Schrödinger equation and apply Floquet's theorem.

$$\begin{aligned} i\hbar \frac{d}{dt} |\psi(t)\rangle &= \hat{H}(t) |\psi(t)\rangle, \\ i\hbar \frac{d}{dt} \left[e^{-\frac{i}{\hbar}\varepsilon_n t} |u_n(t)\rangle \right] &= e^{-\frac{i}{\hbar}\varepsilon_n t} \hat{H}(t) |u_n(t)\rangle, \\ \left[\hat{H}(t) - i\hbar \frac{d}{dt} \right] |u_n(t)\rangle &= \varepsilon_n |u_n(t)\rangle, \\ \hat{H}_F(t) |u_n(t)\rangle &= \varepsilon_n |u_n(t)\rangle, \end{aligned} \quad (3.4)$$

where $\hat{H}_F(t) = \hat{H}(t) - i\hbar \frac{d}{dt}$ is the Hamiltonian that satisfies the eigenvalue equation for the Floquet modes, and is called the “*Floquet Hamiltonian*”. Note that the eigenvalue equation in Eq. (3.4) resembles a typical time-independent eigenvalue equation; however, both the Floquet Hamiltonian and the Floquet modes depend on time. This implies that the state does evolve over time, despite not having the typical form of the Schrödinger equation. Nevertheless to solve it, we need a specific representation, and due to the form of the Floquet Hamiltonian, its matrix representation loses meaning, requiring additional elements to solve and find the respective Floquet modes and their quasienergies. These elements are discussed in subsequent sections, delving into one of the numerical approaches to Floquet's formalism.

Another consequence of Floquet's theorem, as seen in Eq. (3.4), is that the Floquet modes can be

expressed with an additional phase that has a certain driving frequency ω . Specifically,

$$|u_{n,m}(t)\rangle = e^{im\omega t}|u_n(t)\rangle, \quad (3.5)$$

where m is an integer $m = 0, \pm 1, \pm 2$, and $\omega = 2\pi/T$. This new form of Floquet modes yields the same eigenvalue equation (3.4), but with a shifted quasienergy:

$$\varepsilon_n \rightarrow \varepsilon_{n,m} = \varepsilon_n + m\hbar\omega. \quad (3.6)$$

Therefore, this implies that the quasienergies ε_n can be mapped into a zone that contains independent information and is not affected by the multi-evaluation of the complex exponential function. This zone is called the first “*Floquet-Brillouin zone*” [46], alluding again to a concept from solid-state physics, the Brillouin zone. By convention, it is given for $m = 0$ and includes the interval $-\hbar\omega/2 < \varepsilon < \hbar\omega/2$, which can be shifted in multiples of $\hbar\omega$ for the convenience of each system.

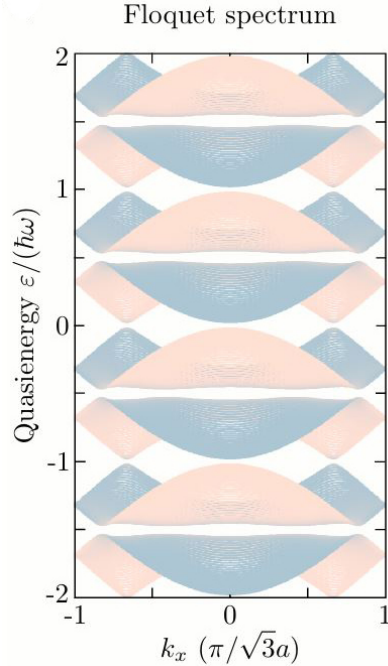


Figure 3.1: The Floquet (quasienergy) spectrum, obtained by diagonalizing the Floquet Hamiltonian \hat{H}_F , is periodic with a Floquet-Brillouin zone of width equal to the driving field energy, $\hbar\omega$ [46].

Thus, any solution to the Eq. (3.4) with quasienergies outside the first Floquet-Brillouin zone, contains physical information identical to a corresponding one inside the first Floquet-Brillouin

zone. Consequently, as illustrated in Fig. (3.1), the spectrum of \hat{H}_F consists of an infinite number of copies of the Floquet spectrum, that is, the information within the first Floquet-Brillouin zone, shifted up and down by integer multiples of $\hbar\omega$.

Now, what type of information about the system do quasienergies offer? We know that because the Hamiltonian depends on time, the energy is no longer conserved, and its expected value loses meaning. However, it can be shown that, under certain conditions, the quasienergies and Floquet states can be seen as approximations to the eigenenergies and eigenstates of the time-independent system [54], thereby providing insights into the system's behavior across different regimes with or without periodic driving. Nevertheless, although quasienergies can provide us with important information about the system, they are not analyzed in this document due to the initially proposed objectives. Thus, quasienergies are utilized solely for constructing the evolved state, as shown in Eq. (3.3) and from it extract information about the observables raised in the Chapter 2. Then, before addressing the time-dependent problem, let's briefly review the theory that describes the spatially periodic but yet temporally static system, Bloch's theorem and its similarities with the Floquet theorem.

3.1.2 Analogies between Bloch's Theorem and Floquet's Theorem

The Bloch theorem is the spatial counterpart of Floquet's theorem, and like it, it provides the general form of the solutions for a system that is periodic, but in space [80].

This theorem is used when solving the stationary Schrödinger equation for a Hamiltonian with a spatially periodic potential, i.e., $\mathcal{H}(x) = \mathcal{H}_0(x) + \mathcal{V}(x)$ with $\mathcal{V}(x) = \mathcal{V}(x + R)$, where R is the lattice spacing. Bloch's theorem tells us that the solutions to the system are given by $\psi_n(x, k) = e^{ikx} \phi_n(x, k)$ with $\phi_n(x, k) = \phi_n(x + R, k)$, where $\phi_n(x, k)$ are the Bloch functions and k is called quasimomentum.

The crucial advantage of the Bloch functions is their spatial periodicity, which allows us to expand them into position-independent Fourier coefficients $a_{n,j}(k)$:

$$\phi_n(x, k) = \sum_{j=-\infty}^{\infty} a_{n,j}(k) e^{i \frac{2\pi}{R} j x}. \quad (3.7)$$

This expansion is not limited to functions or states with spatial periodicities but can be applied to any function or state with a parameter that meets the same periodicity conditions. In this

way, Floquet states can also be expanded into a discrete Fourier series, enabling advantages in the harmonic Fourier space, as discussed in the following section.

So, in spatially discrete lattice systems, the continuous momentum p loses its meaning and is replaced by $\hbar k$, the *quasimomentum*, defined within the first Brillouin zone $-\pi/R < k < \pi/R$ and the Bloch's theorem helps us describe such systems more adequately. Conversely, in Floquet theory, due to the periodicity in time, energy becomes undefined and must be replaced by *quasienergy*, defined within the first Floquet-Brillouin zone $-\hbar\omega/2 < \varepsilon < \hbar\omega/2$. In both theories, a given quantity of the system is replaced due to the discretization of one of its parameters. In Bloch's theorem, space discretization replaces momentum with quasimomentum, and in Floquet's theorem, time discretization (or periodic time jumps T) replaces energy with quasienergy. This illustrates the clear relationship between space-momentum and energy-time, as pairs of canonically conjugated variables that are inherently closely related, exemplifying basic principles of quantum mechanics such as the canonical commutation relations or the Heisenberg uncertainty principle [77]. However, the analogies between Bloch and Floquet theories hold only to a certain extent and should not be overstretched, as the two descriptions address different problems and time cannot be associated as eigenvalue to any operator.

Given this context, we see the importance of both tools for the problem posed in this work. Bloch's theorem helps us lay the foundations for writing and understanding our initial Hamiltonian, which is inherently periodic in space. On the other hand, Floquet's theorem provides a method to tackle the system's dynamics, considering its all degrees of freedom (spin, quadrupole and charge) in a simple and practical manner, provided the condition of temporal periodicity is also met. This condition was introduced in Chapter 2 through external fields, constituting the periodic driving. With this in mind, we are now ready to demonstrate how the Floquet eigenvalue equation proposed in Eq. (3.1) can be solved numerically to analyze the dynamics of the proposed system, which is the main objective of this work.

3.2 Numerically solving the Floquet problem

To solve the Floquet problem numerically, that is, to find a solution to the Floquet modes and quasienergies, there are several approaches focuses in the time evolution operator [76]. However, another common option is to further exploit the periodicity property by expanding the Floquet modes and the Hamiltonian of the system into discrete Fourier series, as we saw can be done in the previous section. This approach transfers the system to harmonic Fourier space, where Eq.

(3.4) can be diagonalized directly. This method is known as extended Hilbert space [46] and is the method used to solve the system under study in this Thesis. .

3.2.1 The Extended Hilbert Space

The extended Hilbert space method [46] uses, as mentioned, the fact that the Floquet modes meet the periodic condition $|u_n(t+T)\rangle = |u_n(t)\rangle$, in such a way that they can be expanded into discrete Fourier series in terms of their harmonics and the drive frequency $\omega = 2\pi/T$,

$$|u_n(t)\rangle = \sum_{m=-\infty}^{\infty} e^{-im\omega t} |\nu_n^{(m)}\rangle, \quad (3.8)$$

where $|\nu_n^{(m)}\rangle$ is the m -th Fourier coefficient. Note that the Fourier coefficients $|\nu_n^{(m)}\rangle$ are not normalized, i.e., generically $\langle \nu_n^{(m)} | \nu_n^{(m)} \rangle < 1$ and there is not a simple orthogonality relation between different Fourier coefficients $|\nu_n^{(m)}\rangle$ and $|\nu_n^{(m')}\rangle$, apart from the (nontrivial) fact that they must add up to produce orthogonal Floquet states $|\psi_n(t)\rangle$ at every time t . Now, the Hamiltonian of the system $\hat{H}(t)$ for the same reasons, also can be expressed as,

$$\hat{H}(t) = \sum_{m=-\infty}^{\infty} e^{-im\omega t} \hat{H}^{(m)}. \quad (3.9)$$

Then taking into account de Fourier decomposition of Floquet modes Eq. (3.8) and the Hamiltonian (3.9) the eigenvalue equation (3.4) can be express in terms of the Fourier coefficients as follows,

$$\left(\sum_{m'} \hat{H}^{(m-m')} - m\hbar\omega \right) |\nu_n^{(m)}\rangle = \varepsilon_n |\nu_n^{(m)}\rangle, \quad (3.10)$$

where

$$\hat{H}^{(m-m')} = \frac{1}{T} \int_0^T dt \hat{H}(t) e^{-i\omega(m-m')t}. \quad (3.11)$$

Note that the Eq. (3.10) takes the form of a typically eigenvalue equation in the Fourier harmonic space. Specifically, we can create a vector $\vec{\varphi}_n$ by “stacking up” the Fourier coefficients $\{|\nu_n^{(m)}\rangle\}$, and rearrange the coefficients $\hat{H}^{(m-m')}$ into a matrix \mathcal{H} acting on vectors in this space, namely the Eq. (3.10) can be represented as:

$$\mathcal{H}\vec{\varphi}_n = \varepsilon_n \vec{\varphi}_n , \quad (3.12)$$

with

$$\mathcal{H} = \begin{pmatrix} \ddots & \hat{H}^{(-1)} & \hat{H}^{(-2)} & \\ \hat{H}^{(1)} & \hat{H}^{(0)} - m\hbar\omega & \hat{H}^{(-1)} & \hat{H}^{(-2)} \\ \hat{H}^{(2)} & \hat{H}^{(1)} & \hat{H}^{(0)} - (m+1)\hbar\omega & \hat{H}^{(-1)} \\ & \hat{H}^{(2)} & \hat{H}^{(2)} & \ddots \end{pmatrix}, \quad \vec{\varphi}_n = \begin{pmatrix} \vdots \\ |\nu_n^{(m)}\rangle \\ |\nu_n^{(m+1)}\rangle \\ \vdots \end{pmatrix}, \quad (3.13)$$

where

$$\hat{H}^{(0)} = \frac{1}{T} \int_0^T dt \hat{H}(t) , \quad (3.14)$$

is the time-average Hamiltonian. Note that the matrix \mathcal{H} , known as the *Floquet Matrix*, in Eq. (3.13) has a block structure: each block is of size d , where d is the dimension of the Hilbert space of the local system, i.e., the dimension of $\hat{H}(t)$. The number of blocks, labeled by Fourier harmonic indices, is formally infinite since the sum over m in Eq. (3.8) and (3.9) ranges over all integers.

By diagonalizing Eq. (3.12), we can obtain the stack of Fourier coefficients and their respective quasienergies, thus providing the necessary superposition to reconstruct the Floquet states and subsequently the state at any time t :

$$|\psi(t)\rangle = \sum_n c_n e^{-\frac{i}{\hbar}\varepsilon_n t} |u_n(t)\rangle = \sum_n c_n e^{-\frac{i}{\hbar}\varepsilon_n t} \left(\sum_{m=-\infty}^{\infty} e^{-im\omega t} |\nu_n^{(m)}\rangle \right). \quad (3.15)$$

However, the extended Hilbert space method has a significant challenge. As seen in Eq. (3.13), we have transitioned from a problem with a matrix of finite dimensions to one requiring the diagonalization of an infinite-dimensional matrix, since the Fourier expansion includes all possible integer harmonics to reconstruct the state. Numerically, this makes it impossible to completely reconstructed the state. Nevertheless, it is important to consider that, as is known, not all coefficients in a Fourier expansion are significant, allowing for the truncation of the matrix in Eq. (3.13). This truncation depends on the regime being studied, as discussed in the following section.

3.2.2 Truncation of the harmonic Fourier space

The problem of dimensionality in the extended Hilbert space can be managed by truncating the Fourier expansion, that is, truncating the matrix of Eq. (3.13), at a certain harmonic m' , such that the sum over the harmonics is within the interval $m \in [-m', m']$. This approach increases the dimensionality of the original system's matrix $\hat{H}(t)$ from d to $d(2m' + 1)$, making it numerically solvable. However, the question arises: Is it possible to truncate the matrix \mathcal{H} without losing relevant system information? To answer this, it is convenient to analyze the structure of the matrix \mathcal{H} given a certain periodic drive, which is commonly cosine-shaped. Let's consider the following time-dependent Hamiltonian:

$$\hat{H}(t) = \hat{H}_0 + \hat{V}(t), \quad \hat{V}(t) = \hat{V}e^{i\omega t} + \hat{V}^\dagger e^{-i\omega t}, \quad (3.16)$$

the corresponding extended-zone of the Floquet Hamiltonian, \mathcal{H} then takes the form in Eq. (3.13) with $\hat{H}^{(1)} = \hat{V}$, $\hat{H}^{(-1)} = \hat{V}^\dagger$, and $\hat{H}^{(\Delta m)} = 0$ for $|\Delta m| > 1$. In this case, \mathcal{H} has a block-tridiagonal form, with the non-driven Hamiltonian \hat{H}_0 (shifted by multiples of $\hbar\omega$) repeated along the diagonal blocks, and the drive coupling \hat{V} (\hat{V}^\dagger) placed in the blocks above (below) the diagonal:

$$\mathcal{H} = \begin{pmatrix} \ddots & \hat{V} & 0 & & \\ \hat{V}^\dagger & \hat{H}_0 + \hbar\omega & \hat{V} & 0 & \\ 0 & \hat{V}^\dagger & \hat{H}_0 & \hat{V} & 0 \\ & 0 & \hat{V}^\dagger & \hat{H}_0 - \hbar\omega & \hat{V} \\ & & 0 & \hat{V}^\dagger & \ddots \end{pmatrix}. \quad (3.17)$$

Importantly, the (block) tridiagonal structure of \mathcal{H} is closely analogous to a tight-binding lattice with nearest-neighbor hopping and a linear potential, i.e., to the problem of a particle in a one-dimensional lattice with a uniform electric field, but in this case it would be in a harmonic Fourier space or in a “*Floquet lattice*”, as can be seen in the Fig. (3.2). By making analogies to Bloch oscillations [81] and to the Wannier-Stark ladder [82], we may gain important insight into the nature of the Floquet states encoded in the solutions to Eq. (3.13). These insights furthermore shed light on the utility of this approach as a numerical method for obtaining Floquet states.

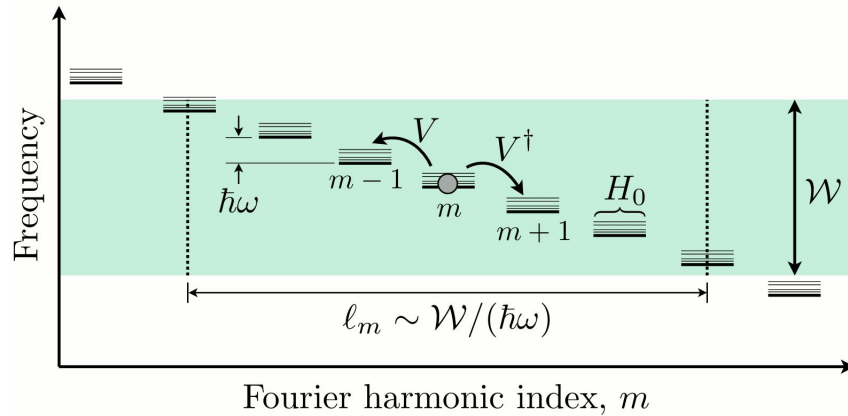


Figure 3.2: The extended-zone of the Floquet Hamiltonian, Eq. (3.17), can be interpreted as describing the one-dimensional tight-binding dynamics of an effective “particle” hopping in Fourier harmonic space [46].

So, as we can see, the extended Hamiltonian in the Fourier harmonic space can be interpreted as the dynamics of an effective “particle” that jumps between sites of a one-dimensional lattice, the Floquet lattice. Each unit cell is represented by a harmonic m and is described by the time-averaged Hamiltonian \hat{H}_0 . The linear driving term induces “jumps” between neighbors in the different lattice sites of the Fourier space, making the harmonic index m change by one, and the energies at the sites vary linearly with m due to the terms $-m\hbar\omega$ in the diagonal blocks of Eqs. (3.14), which can be interpreted as a “linear potential” analogous to applying a uniform field in a classical system. In the absence of this potential, the eigenstates of the system can be understood as “Bloch functions” in Fourier space with a corresponding bandwidth $\mathcal{W} \sim \{\langle \hat{V} \rangle, \langle \hat{H}_0 \rangle\}$, being strongly delocalized. However, by including the “linear potential” ($-m\hbar\omega$), it acts as a uniform electric field on the particle, meaning that from a semiclassical point of view, the effective particle can only explore a range of harmonics $\ell_m \sim \mathcal{W}/(\hbar\omega)$, and therefore the Floquet states represent “Wannier functions”, implying they are strongly localized in the Fourier harmonic space. Consequently, the infinite dimensional matrices of Eqs. (3.13) and (3.14) can be safely truncated up to the most relevant harmonics [46].

But how can we truncate this matrix up to the most relevant harmonics? Here, we have to distinguish two regimes. In the “*weak-driving*” regime, i.e. $\hbar\omega \gg \langle \hat{V} \rangle$, which is also known as the high-frequency regime [83], only one block of the Floquet matrix is relevant, namely,

$$\mathcal{H} = \begin{pmatrix} \hat{H}_0 + \hbar\omega & \hat{V} \\ \hat{V}^\dagger & \hat{H}_0 \end{pmatrix}, \quad (3.18)$$

in which it recognize in the context of quantum optics as the rotating-wave approximation [84]. If instead the driving frequency is on the same order as the periodic driving $\hbar\omega \sim \langle \hat{V} \rangle$, we reach the “*strong-driving*” regime in which many blocks of the Floquet matrix have to be taken into account [85]. One way to know how many blocks or harmonics are enough to completely reconstruct the state is to consider the completeness of the Floquet modes. Since unitary evolutions are always being considered, the norm of the state must be preserved (Eq. 3.15), and therefore, the sum of the square modulus of the superposition coefficients must be exactly equal to 1, at every instant of time t , $\sum_n |c_n|^2 = 1$. If this sum is greater or less, it means that not enough harmonics are being considered and therefore they must be increased, or, alternatively, the period of the driving must be decreased to be closer to the high-frequency regime.

Having explained the technique and numerical method to be used, the implementation of Floquet’s Theorem and the extended Hilbert space for the case of a single particle in a two-site lattice is shown below, in addition to the exact analytical calculation that can be developed. This comparison between the numerical technique and the exact solution demonstrates the validity of the method for its subsequent use in the complete system described in Chapter 2.

3.3 Implementation of the Floquet’s Theorem

To show the comparison between the numerical implementation of Floquet’s theorem and the exact calculation provided for a single-particle system, let us start with the analytical solution which involves a typical diagonalization with Fourier transforms.

3.3.1 Exact Solution

To solve the single-particle system described in chapter 2, we start with the Hamiltonian given in Eq. (2.20), which is:

$$\hat{H}(t) = -J \sum_{i,\sigma} \left(\hat{b}_{i,\sigma}^\dagger \hat{b}_{i+1,\sigma} + \hat{b}_{i+1,\sigma}^\dagger \hat{b}_{i,\sigma} \right) - \mu \sum_{i,\sigma} \hat{n}_{i,\sigma} + D_0 \cos^2(\omega t) \sum_{i,\sigma} \sigma \hat{n}_{i,\sigma}. \quad (3.19)$$

As mentioned, this Hamiltonian describes a single spin-1 particle in a one-dimensional optical lattice under the influence of a periodic driving, let's consider the linear Zeeman field, but one can equally apply a quadratic Zeeman field. The analytical solution for this system is obtained through a Fourier transform of the Hamiltonian, which allows it to be expressed in momentum space,

$$\hat{b}_{j,\sigma} = \frac{1}{\sqrt{L}} \sum_{k=1}^L e^{-i\frac{2\pi}{L}jk} \hat{c}_{k,\sigma}, \quad \hat{c}_{k,\sigma} = \frac{1}{\sqrt{L}} \sum_{j=1}^L e^{i\frac{2\pi}{L}jk} \hat{b}_{j,\sigma}, \quad (3.20)$$

then, the Hamiltonian in momentum space takes the form:

$$\hat{H}(t) = -2J \sum_{k,\sigma} \cos\left(\frac{2\pi}{L}k\right) \hat{n}_{k,\sigma} - \mu \sum_{k,\sigma} \hat{n}_{k,\sigma} + D_0 \cos^2(\omega t) \sum_{k,\sigma} \sigma \hat{n}_{k,\sigma}, \quad (3.21)$$

which is diagonal in momentum space. Note that the temporal dependency of the Hamiltonian in Eq. (2.20) was introduced as an amplitude of a specific operator, in this case \hat{S}^z . This indicates that the commutation relations between the operators that make up the Hamiltonian do not change over time, ensuring that the Hamiltonian commutes at different times, i.e., $[\hat{H}(t_1), \hat{H}(t_2)] = 0$. Consequently, the time evolution operator can be calculated in the usual form:

$$\hat{U}(t) = \exp\left\{-\frac{i}{\hbar} \int_0^t \hat{H}(t') dt'\right\}, \quad (3.22)$$

therefore, integrating the Hamiltonian, we obtain

$$\int_0^t \hat{H}(t') dt' = \sum_{k,\sigma} \left(-2J \cos\left(\frac{2\pi}{L}k\right) - \mu \right) t \hat{n}_{k,\sigma} + D_0 \frac{\sin(2\omega t) + 2\omega t}{4\omega} \sum_{k,\sigma} \sigma \hat{n}_{k,\sigma}, \quad (3.23)$$

and finally, the time-evolution operator is given by

$$\hat{U}(t) = \exp\left\{\frac{i}{\hbar} \sum_{k,\sigma} (\epsilon_{k,L} t - g(t)\sigma) \hat{n}_{k,\sigma}\right\}, \quad (3.24)$$

where we define $\epsilon_{k,L} = 2J \cos\left(\frac{2\pi}{L}k\right) + \mu$ and $g(t) = D_0 \frac{\sin(2\omega t) + 2\omega t}{4\omega}$. Now, the choice of basis is clearly the eigenbasis of the number operator $\{|n_1, n_{-1}, n_0\rangle\}$, which tells us the number of particles with a momentum k (site i) in a specific magnetic projection σ , namely,

Position space	Momentum space	
$\cdots n_1, n_{-1}, n_0\rangle_i n_1, n_{-1}, n_0\rangle_{i+1} \cdots$	$\cdots n_1, n_{-1}, n_0\rangle_k n_1, n_{-1}, n_0\rangle_{k+1} \cdots$	(3.25)

Then, since we want to describe a single spin-1 particle in the entire lattice, the only possible states are of the type $\{|1, 0, 0\rangle_1 |\emptyset\rangle \cdots, |0, 1, 0\rangle_1 |\emptyset\rangle \cdots, |0, 0, 1\rangle_1 |\emptyset\rangle \cdots, |\emptyset\rangle_1 |0, 0, 0\rangle_2 |\emptyset\rangle \cdots, \cdots\}$, i.e., one particle in the magnetic projection 1, -1 , or 0 with a momentum (site) 1 and vacuum in the other sites, or one particle in the magnetic projection 1, -1 , or 0 with a momentum (site) 2 and vacuum in the other sites, and so on. Note that the time evolution operator of Eq. (3.24) evolves any initial state for any number of sites. However, determining the evolved state for any number of initial states and calculating all observables for those different initial states becomes impractical, thus the implementation of a numerical technique (Floquet) to speed up this process becomes more striking. Therefore, for comparison, let us consider only two sites $L = 2$. The matrix representation for the two-site time evolution operator is given by

(k)	$ \emptyset\rangle$	$ 1, 0, 0\rangle \emptyset\rangle$	$ 0, 1, 0\rangle \emptyset\rangle$	$ 0, 0, 1\rangle \emptyset\rangle$	$ \emptyset\rangle 1, 0, 0\rangle$	$ \emptyset\rangle 0, 1, 0\rangle$	$ \emptyset\rangle 0, 0, 1\rangle$
$\mathcal{U} =$	$\langle \emptyset $	1	0	0	0	0	0
	$\langle \emptyset 1, 0, 0 $	0	$e^{\frac{i}{\hbar}(\epsilon_{1,2}t-g(t))}$	0	0	0	0
	$\langle \emptyset 0, 1, 0 $	0	0	$e^{\frac{i}{\hbar}(\epsilon_{1,2}t+g(t))}$	0	0	0
	$\langle \emptyset 0, 0, 1 $	0	0	0	$e^{\frac{i}{\hbar}\epsilon_{1,2}t}$	0	0
	$\langle 1, 0, 0 \langle \emptyset $	0	0	0	$e^{\frac{i}{\hbar}(\epsilon_{2,2}t-g(t))}$	0	0
	$\langle 0, 1, 0 \langle \emptyset $	0	0	0	0	$e^{\frac{i}{\hbar}(\epsilon_{2,2}t+g(t))}$	0
	$\langle 0, 0, 1 \langle \emptyset $	0	0	0	0	0	$e^{\frac{i}{\hbar}\epsilon_{2,2}t}$

where the matrix representation is given in the momentum basis (k) . We can see that the vacuum state $|\emptyset\rangle$ has been included in the basis, due to the importance of the vacuum state in this type of lattice systems, where jumps between sites only occur if there is a vacuum in the consecutive sites. Without the vacuum state, the description of the system in Hilbert space would be incomplete, meaning that some physically possible configurations of the system would be inaccessible in the mathematical formulation. Furthermore, the vacuum state plays a crucial role in modeling phase transitions, such as the Superfluid-Mott Insulator transition in the spinless model [86]. Thus, only the initial conditions $|\psi(0)\rangle$ are needed to calculate the state at any time $|\psi(t)\rangle = \hat{U}(t)|\psi(0)\rangle$.

3.3.2 Numerical implementation

For the numerical implementation of Floquet's Theorem and the extended Hilbert space approach in the spin-1 Bose-Hubbard model, the following steps are followed (for further details see appendix C):

1. **Set the initial parameters:** For both of our considered systems defined by the Eqs. (2.20) and (2.24), we set the number of sites L , the hopping rate J , the chemical potential μ , the interaction strengths U_2 and U_0 (which vanish for the one particle system), the Linear Zeeman Strength D_0 (or quadratic Zeeman strength Q_0), the driving frequency ω , which is set to $\omega \gg D_0$ (\hbar is fixed to 1) for the high-frequency regime or $\omega \sim D_0$ for the strong-driving regime, and the number of harmonics m , which are determined depending on the regime used, and is equivalent to $2m + 1$ blocks of the Floquet matrix.
2. **Generate the local and non-local matrix of the Hamiltonian:** With the parameters defined previously, we generate the local matrix of each operator of the Hamiltonian in the position basis, i.e., the matrix of each operator of only one site (two sites in the case of the hopping term): the hopping term, the chemical potential $\hat{n}_{i,\sigma}$, the charge scattering $\hat{n}_{i,\sigma}(\hat{n}_{i,\sigma} - 1)$, the spin scattering \hat{F}_i^2 , and the linear Zeeman field $\sigma\hat{n}_{i,\sigma}$ (or quadratic Zeeman field $\sigma^2\hat{n}_{i,\sigma}$). Then, we generate the non-local matrices from the local ones using Kronecker products, i.e., we generate the matrices for L sites.
3. **Generate the Floquet Matrix:** Once the Hamiltonian matrix for L sites is defined, we generate the Floquet matrix from Eq. (3.13), calculating each Fourier coefficient of the Hamiltonian as specified by Eq. (3.11), integrating with the Trapezoidal Quadrature, given by the C++ Boost-Math library and only up to the number of harmonics m specified.
4. **Diagonalization and reconstruction of the state:** Given the previously calculated Floquet matrix, we proceed to diagonalize it with the help of the LAPACK library, thereby finding the quasienergies and the determined Floquet modes to reconstruct the state given by Eq. (3.15), taking into account the previous calculation of the coefficients c_n defining the initial state $|\psi(0)\rangle$.
5. **Measurement of observables:** Once the state $|\psi(t)\rangle$ has been reconstructed for any time t , we measure the observables described in chapter 2, the number of atoms per lattice site in each spin component $\langle\hat{n}_{i,\sigma}\rangle$, the magnetic density $\langle\hat{S}_i^z\rangle$, the quadrupolar density $\langle\hat{Q}_i^d\rangle$, and the total transverse magnetization, $|\langle\hat{F}_i^x\rangle|^2$, analyzing their behavior over time.

3.3.3 Comparison between analytical and numerical solutions

To compare the numerical technique with the exact analytical solution, we established the two-site single-particle model. The analytically evolved state is obtained by applying the time evolution operator given by Eq. (3.24), and the numerically evolved state is obtained by following the steps described above. Note that the matrix of the two-site system is expressed as follows:

$$\mathbf{H} = \begin{pmatrix} 0 & 0 & 0 & 0 & 0 & 0 & 0 \\ 0 & -\mu + D_0 & 0 & 0 & -2J & 0 & 0 \\ 0 & 0 & -\mu - D_0 & 0 & 0 & -2J & 0 \\ 0 & 0 & 0 & -\mu & 0 & 0 & -2J \\ 0 & -2J & 0 & 0 & -\mu + D_0 & 0 & 0 \\ 0 & 0 & -2J & 0 & 0 & -\mu - D_0 & 0 \\ 0 & 0 & 0 & -2J & 0 & 0 & -\mu \end{pmatrix}. \quad (3.26)$$

To simplify both analytical and numerical calculations, we set the following values for the system parameters, taking into account that the hopping rate is our energy unit: $J = \mu = D_0 = 1$ and $\omega = 2\pi/T$ with $T = 0.01$ s. This places us in the high-frequency regime, where only one harmonic $m = 1$ is sufficient to consider. Once the parameters are established, we choose an arbitrary initial state; in this case, $|\psi(0)\rangle = |1, 0, 0\rangle^{(1)}|\emptyset\rangle$, i.e., the initial state is given by a particle with magnetic projection 1 at site $i = 1$.

It must be noted that the numerical method is given in the position basis, while the analytical solution is in the momentum basis. To ensure that the same initial state is evolving, it must be written $|\psi(0)\rangle$ in the momentum basis using Eq. (3.20),

$$|\psi(0)\rangle = |1, 0, 0\rangle^{(i)}|\emptyset\rangle = -\frac{1}{\sqrt{2}}|1, 0, 0\rangle^{(k)}|\emptyset\rangle + \frac{1}{\sqrt{2}}|\emptyset\rangle|1, 0, 0\rangle^{(k)}, \quad (3.27)$$

where the superscript i (k) indicates the state in the position (momentum) basis. Therefore, using the time-evolution operator of Eq. (3.24) and noting that with the parameters given above $\epsilon_{1,2} = -1$, $\epsilon_{2,2} = 3$, and $g(t)$ results in a global phase, the evolved state in the momentum basis is given by

$$|\psi(t)\rangle = -\frac{e^{-2it}}{\sqrt{2}}|1, 0, 0\rangle^{(k)}|\emptyset\rangle + \frac{e^{2it}}{\sqrt{2}}|\emptyset\rangle|1, 0, 0\rangle^{(k)}, \quad (3.28)$$

or in the position basis using again Eq. (3.20) as

$$|\psi(t)\rangle = \cos(2t)|1, 0, 0\rangle^{(i)}|\emptyset\rangle + i \sin(2t)|\emptyset\rangle|1, 0, 0\rangle^{(i)}. \quad (3.29)$$

This allows us to measure the observables mentioned in the previous section over time. For comparison purposes, a clear behavior of the evolution of the state can be seen if we project it onto its initial state $|\psi(0)\rangle$,

$$|\langle\psi(0)|\psi(t)\rangle|^2 = \cos^2(2t), \quad (3.30)$$

which can also be seen numerically in Fig 3.3.

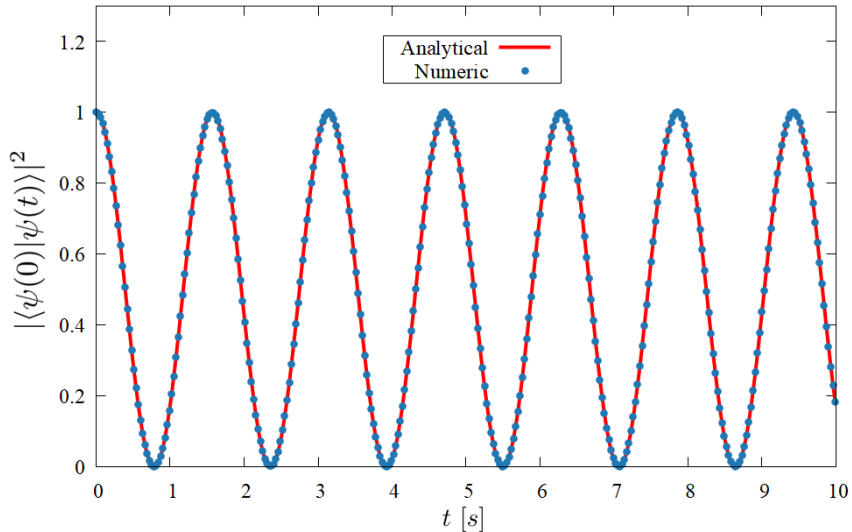


Figure 3.3: Probability that the evolved state $|\psi(t)\rangle$ returns to its initial state $|\psi(0)\rangle = |1, 0, 0\rangle^{(i)}|\emptyset\rangle$, calculated exactly Eq. (3.30) and numerically through Floquet's theory, for $L = 2$, $J = \mu = D_0 = 1$ and $T = 0.01$ s.

Then, we can see that the numerical implementation matches perfectly with the exact analytical solution, showing in both cases a clear transition between the states $|1, 0, 0\rangle|\emptyset\rangle \rightarrow |\emptyset\rangle|1, 0, 0\rangle$, i.e., a jump of a particle from site 1 to site 2, then from site 2 to site 1 again, and so on in time, always preserving the same initial magnetic projection (i.e., $\sigma=1$) due to the absence of interactions.

We can also compare the behavior of the observables described in Chapter 2. However, due to the lack of interactions and the polarized initial state, it can be easily shown that the quadrupolar density, magnetic density, and transverse magnetization remain constant over time: $\langle \hat{Q}_i^d \rangle_t = \frac{1}{\sqrt{3}}$, $\langle \hat{S}_i^z \rangle_t = 1$, $|\langle \hat{S}_i^x \rangle_t|^2 = 0$, as corroborated by Fig 3.4.

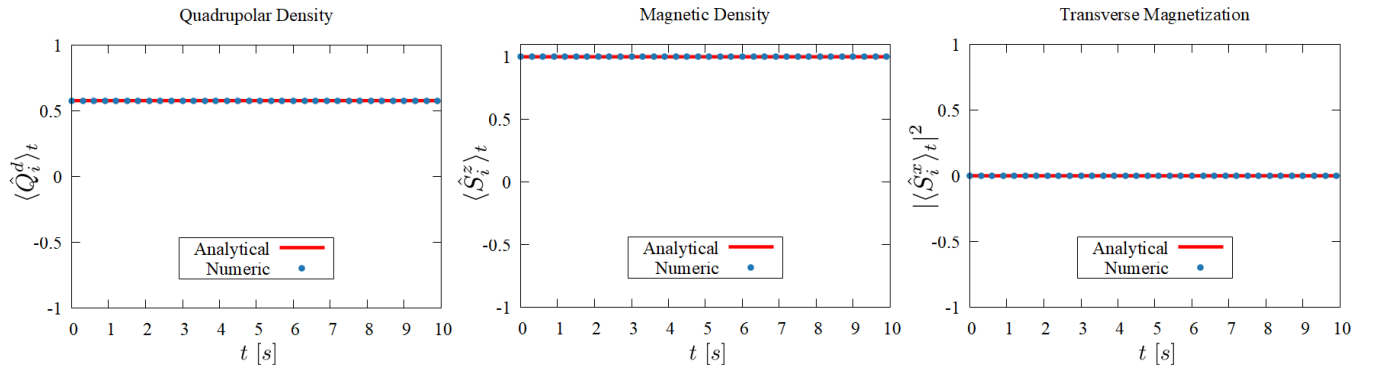


Figure 3.4: The expected value in time for the quadrupolar density \hat{Q}_i^d , the magnetic density \hat{S}_i^z and the transverse magnetization \hat{S}_i^x given the initial state $|\psi(0)\rangle = |1, 0, 0\rangle^{(i)} |\emptyset\rangle$.

Note that for this specific initial state, the contribution of the Zeeman field results in a global phase, so the imposed driving does not affect the system, and its behavior depends exclusively on the hopping term and the chemical potential. However, this is due exclusively to the initial condition, and by exploring different initial states, the effect of the driving and its different regimes on the system can be better analyzed, both for linear and quadratic Zeeman fields, as discussed in depth in the following chapter.

Although the above description for the implementation of Floquet's theorem was given for a particular physical system with an exact analytical solution, it is easy to modify all parameters to work with more sites, different initial states, include interactions, among other modifications which make the system more complex and therefore analytically unsolvable, but numerically plausible and flexible. Whether for one or two particles, the method requires following the steps provided in this section. Likewise, if two-dimensional or three-dimensional lattices are considered, it is possible to apply Floquet's technique by adjusting the Hamiltonian of the system accordingly, just as with any other numerical method that works with lattice systems. In Appendix C, we provide a more in-depth explanation of the implementation of Floquet's theorem in the C++ language, mentioning the libraries used, specifications in the integration method, and other details introduced to make the calculations more efficient.

With the construction of our Numerical Floquet Theorem, we proceed to use it to study the dynamics of one and two spin-1 lattice bosons in the presence of external magnetic fields, focusing mainly on the behavior of spinorial and quadrupolar dynamics and the effects of driving on this type of system.

Chapter 4

DYNAMICAL ANALYSIS

In this chapter, we present the study of the dynamics of one and two spin-1 lattice bosons in the presence of external periodic magnetic fields, either linear or quadratic Zeeman, within the superfluid regime, employing the Floquet theory described in chapter 3. This chapter is divided into two main sections: one focusing on the dynamics of a single particle and the other on the dynamics of two particles.

First, we analyze a single particle. For this, we establish the parameters and cases to be analyzed, which are divided into a linear Zeeman field case and a quadratic Zeeman field case. In each case, we focus on the weak and strong driving regimes, analyzing the behavior of the observables described in previous chapters with different initial states.

Subsequently, we analyze two particles. We again begin by establishing the chosen parameters. In this case, only the dynamics with a quadratic field is relevant and the section is divided into antiferromagnetic and ferromagnetic phases. In each phase, we focus on the regimes appear due to the presence of the Zeeman field, the interaction regime and the Zeeman regime, analyzing the behavior of the same observables with a polarized initial state.

4.1 One particle

To show the dynamic behavior of our single-particle system, following the steps that we established in the previous chapter in the numerical implementation, let us first specify the particularities of the single-particle system:

1. **Set the initial parameters:** The Hamiltonian for this system is given by Eq. (2.20) and Eq. (2.22), each differing only by the external magnetic field, while the other parameters of the system remain the same. Taking this into account, we define the number of sites L , which is determined by considering how our system grows given a number of sites and defining an L according to our computational power. This is also related to the number of states in the basis. Generally, the number of states (N_T) or the size of the Hilbert space in these types of systems grows exponentially as a function of the states of the local basis (n_l) and the number of sites (L),

i.e., $N_T = (n_l)^L$. In this case, the states of the local basis are given by the number of magnetic projections, $\{|1, 0, 0\rangle, |0, 1, 0\rangle, |0, 0, 1\rangle\}$, and the vacuum state $|\emptyset\rangle$. Thus, the growth of our Hilbert space would be 4^L . However, since we want to describe a single particle in the entire lattice, the number of states given by this analysis includes all mathematically possible combinations of states given a local basis, which are not all physically possible due to our single-particle constraint. To see this, let's consider the case with only two sites $L = 2$, such that the total number of states is $N_T = 16$. However, the matrix of the system includes only 7 effective states. To see where these seven states come from, let's consider the 16 total states:

Site 1	Site 2	All combinations of states				
$ \emptyset\rangle$	$ \emptyset\rangle$	$ \emptyset\rangle \emptyset\rangle$	$ \emptyset\rangle 1, 0, 0\rangle$	$ \emptyset\rangle 0, 1, 0\rangle$	$ \emptyset\rangle 0, 0, 1\rangle$	
$ 1, 0, 0\rangle$	$ 1, 0, 0\rangle$	$ 1, 0, 0\rangle \emptyset\rangle$	$ 1, 0, 0\rangle 1, 0, 0\rangle$	$ 1, 0, 0\rangle 0, 1, 0\rangle$	$ 1, 0, 0\rangle 0, 0, 1\rangle$	(4.1)
$ 0, 1, 0\rangle$	$ 0, 1, 0\rangle$	$ 0, 1, 0\rangle \emptyset\rangle$	$ 0, 1, 0\rangle 1, 0, 0\rangle$	$ 0, 1, 0\rangle 0, 1, 0\rangle$	$ 0, 1, 0\rangle 0, 0, 1\rangle$	
$ 0, 0, 1\rangle$	$ 0, 0, 1\rangle$	$ 0, 0, 1\rangle \emptyset\rangle$	$ 0, 0, 1\rangle 1, 0, 0\rangle$	$ 0, 0, 1\rangle 0, 1, 0\rangle$	$ 0, 0, 1\rangle 0, 0, 1\rangle$	

As we can see, all the mathematically possible states are built from the Kronecker product (see appendix C). However, only the states in row 1 and column 1 are physically possible, since they respect the single particle constraint. Hence, for two sites, the effective basis consists of 7 states. For three sites, the effective basis consists of 10 states. Thus, for L sites, the total number of states is $N_T = 3L + 1$. Consequently, for a single particle, the size of our Hilbert space grows linearly, making the growth of the system not result in any computational problem.

Having taken this into account, it is possible to choose an arbitrary number of sites without any numerically relevant cost. For this case, we choose $L = 30$, a common number of sites in these types of systems.

For the other parameters, we must consider our energy unit, which is the hopping rate, $J = 1$. We similarly set the chemical potential to the same order $\mu = 1$. For the parameters of the external field, we establish the couplings $D_0 = 1$ and $Q_0 = 1$ for the linear and quadratic fields, respectively. Finally, we establish the study regime, considering that for the weak driving regime, we set the period to 1000 times smaller than the field coupling, i.e., $T = 10^{-3}D_0$, such that $\omega \gg D_0$ and only one harmonic is sufficient $m = 1$. For the strong driving regime, we set the period of equal order to the coupling, i.e., $T = D_0$, such that $\omega \sim D_0$ and set five harmonics $m = 5$, ensuring that for each initial state $\sum_n |c_n|^2 = 1$ is fulfilled.

2. Generate the local and non-local matrix of the Hamiltonian: We generate the non-local operators directly, the matrix elements are arranged as specified in Eq. (3.25), in the position basis. Additionally, we manually include periodic boundary conditions (PBC), allowing transitions between the local states first and last sites.

3. Generate the Floquet Matrix: We generate the Floquet matrix as specified in Eq. (3.13). This matrix has a dimension of $(3L + 1)(2m + 1) \times (3L + 1)(2m + 1)$, which again does not pose any further computational cost.

4. Diagonalization and reconstruction of the state: We diagonalize and fully reconstruct the state for any time t in time steps of $\delta t = 0.01$ s, specifying the initial evolved state, which was chosen based on experimentally realizable initial states. These generally encompass polarized states [45] in a specific magnetic projection, polarized states with slight deviations indicating a certain uncertainty, quadrupolar states, among others that are specified in each case.

5. Measurement of observables: Finally, we measure the average number of total particles in each magnetic projection $\langle \hat{n}_\sigma \rangle$, the total magnetic density $\langle \hat{S}^z \rangle$, the total quadrupole density $\langle \hat{Q}^d \rangle$ and the transverse magnetization $|\langle \hat{S}^x \rangle|^2$.

These considerations leave us with the following suitable parameters for the single-particle system.
Cases:

1. **$L = 30, J = 1, \mu = 1, D_0 = 1, T = 10^{-3}D_0$** , and $m = 1$ for the weak-driving regime with linear Zeeman field.
2. **$L = 30, J = 1, \mu = 1, D_0 = 1, T = D_0$** , and $m = 5$ for the strong-driving regime with linear Zeeman field.
3. **$L = 30, J = 1, \mu = 1, Q_0 = 1, T = 10^{-3}Q_0$** , and $m = 1$ for the weak-driving regime with quadratic Zeeman field.
4. **$L = 30, J = 1, \mu = 1, Q_0 = 1, T = Q_0$** , and $m = 5$ for the strong-driving regime with quadratic Zeeman field.

This section should be read in conjunction with Appendix D, which further explores various changes to system parameters that aid in a more comprehensive analysis of the system.

4.1.1 Linear Zeeman Field

For the linear Zeeman field described by Eq. (2.19), we begin by analyzing the behavior in the weak-driving regime, $T = 10^{-3}D_0$, first case.

Case 1: Weak-Driving Regime with a linear Zeeman field.

Fully-polarized initial states.

The most typical initial states to analyze are the polarized states corresponding to each of the magnetic projections. In this scenario, the only particle in the lattice is in the magnetic projection 1, -1, or 0 at an arbitrary site, with all other sites in the vacuum state, i.e., $\{|1, 0, 0\rangle_1|\emptyset\rangle \dots, |0, 1, 0\rangle_1|\emptyset\rangle \dots, |0, 0, 1\rangle_1|\emptyset\rangle \dots\}$. It is possible for simplicity to use the single-spin magnetic basis notation as shown in Chapter 2. This approach allows us to analyze the behavior of the observables given the initial states $|1\rangle$, $| - 1\rangle$, and $|0\rangle$ in the weak-driving regime, as illustrated in Figs. 4.1 and 4.2.

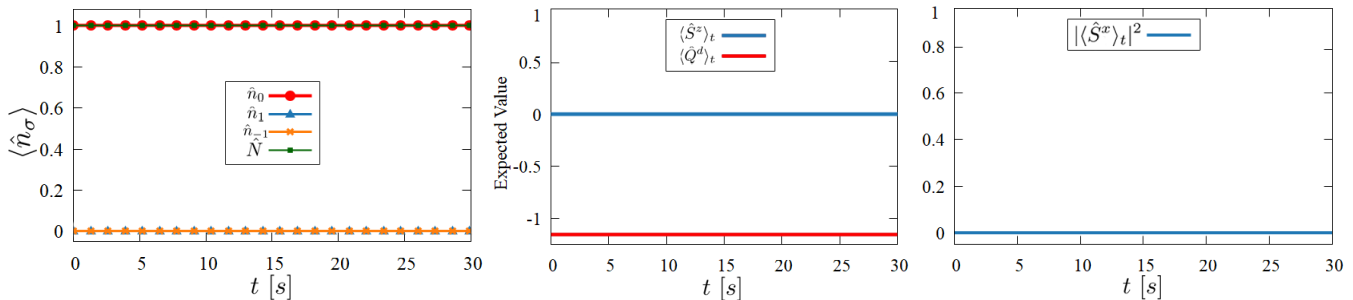


Figure 4.1: The expected value in time for the number of particles in each magnetic projection \hat{n}_σ (left), the quadrupolar density \hat{Q}^d together with the magnetic density \hat{S}^z (center) and the transverse magnetization \hat{S}^x (right) given the initial state $|\sigma = 0\rangle$ with $L = 30$, $J = 1$, $\mu = 1$, $D_0 = 1$, $T = 10^{-3}D_0$, and $m = 1$.

As depicted in Figs. 4.1 and 4.2, for all three initial states, the evolution of the observables remains constant over time. Moreover, the behavior for the initial states with projections $|1\rangle$ and $| - 1\rangle$ is identical, with the exception that the magnetic density changes sign and the populations are clearly inverted. Consequently, when this clear symmetry is present, it is sufficient to analyze only one of the two states. Additionally, it is observed that the external field has no effect on the system, since in all three cases, the initial state is polarized with a single particle, meaning there is no interaction that alters the initial magnetic projections. Furthermore, both the magnetic density and the quadrupolar density retain their expected values given the initial states described ($\langle \pm 1 | \hat{S}^z | \pm 1 \rangle = \pm 1$, $\langle 0 | \hat{Q}^d | 0 \rangle = -\frac{2}{\sqrt{3}}$), as demonstrated in Eq. (2.35). It is also noteworthy that

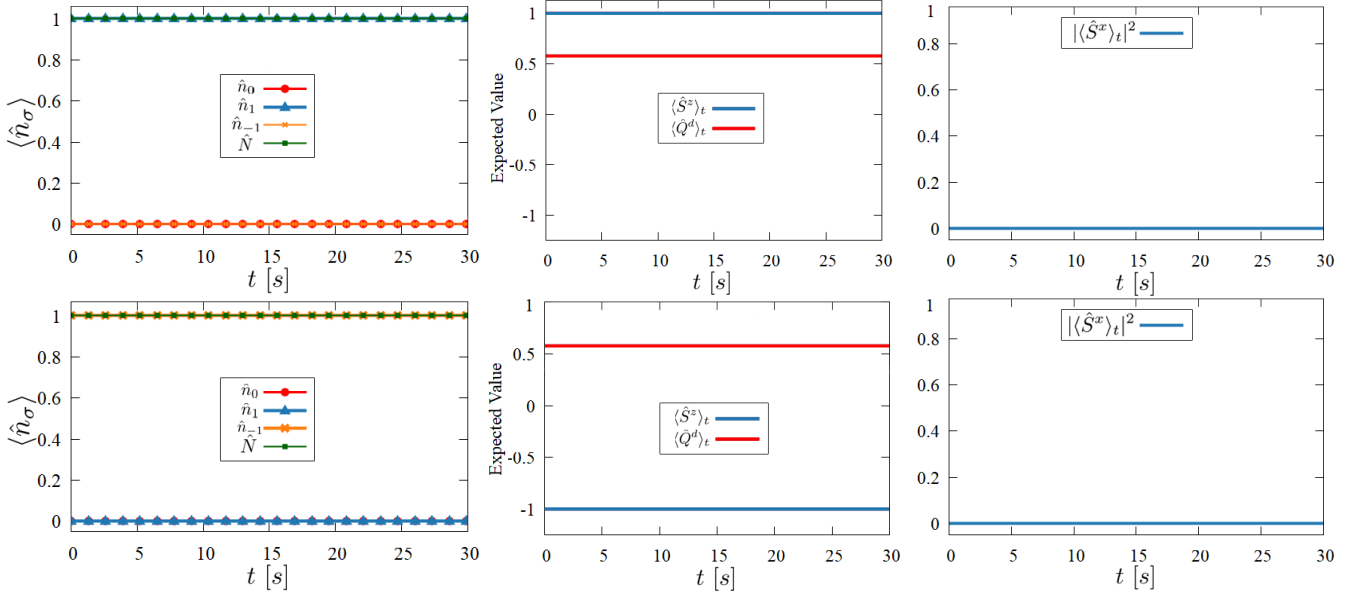


Figure 4.2: The expected value in time for the number of particles in each magnetic projection \hat{n}_σ (left), the quadrupolar density \hat{Q}^d together with the magnetic density \hat{S}^z (center) and the transverse magnetization \hat{S}^x (right) given the initial state $|\sigma = 1\rangle$ (top row) and $|\sigma = -1\rangle$ (bottom row) with $L = 30$, $J = 1$, $\mu = 1$, $D_0 = 1$, $T = 10^{-3}D_0$, and $m = 1$.

for all three initial states, the transverse magnetization vanishes, which is typical of polarized states that do not exhibit any spin fluctuations in the plane.

Another important quantity worth for analyzing over time is the total contributions from both the spin and the quadrupole, i.e., verifying whether the competition $\langle \hat{S} \rangle^2 + \langle \hat{Q} \rangle^2 = 4/3$, described in Eq. (2.31) is fulfilled over time. As observed, this relationship is composed of quadratic contributions, making it sufficient once again to distinguish only between magnetic ($|1\rangle$ and $| - 1\rangle$) and non-magnetic states ($|0\rangle$). This approach explicitly illustrates the contribution of higher-order magnetic moments.

We can see in Fig. 4.3, the competition between spin and quadrupolar orders over time, given the magnetic and non-magnetic states as initial states. Note that these contributions remain constant and fulfill exactly the relationship expected for the SU(3)-Bosonic representation of spin-1, summarized in Eq. (2.31). This demonstrates that the spin-1 states, even a single particle, exhibit both spin and quadrupolar order. It is also noteworthy that the magnetic states exhibit both orders, as $\langle \hat{S} \rangle_t^2 \neq 0$ and $\langle \hat{Q} \rangle_t^2 \neq 0$, unlike the non-magnetic state that only presents quadrupolar order $\langle \hat{S} \rangle_t^2 = 0$, $\langle \hat{Q} \rangle_t^2 = 4/3$, indicating its nematic nature.

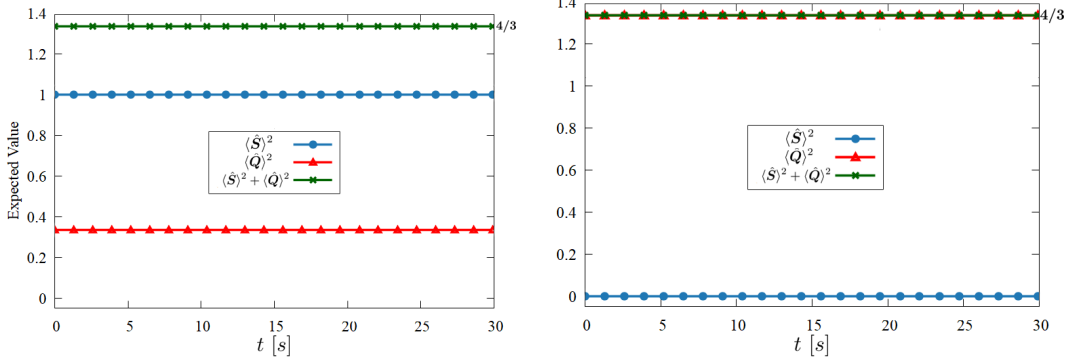


Figure 4.3: Spin-Quadrupole competition in time for the initial state $|\pm 1\rangle$ (left) and $|0\rangle$ (right) with $L = 30$, $J = 1$, $\mu = 1$, $D_0 = 1$, $T = 10^{-3}D_0$, and $m = 1$.

Partially-polarized initial states.

Now, the polarized states may not necessarily remain completely polarized in a specific magnetic projection. Therefore, it is of interest to also analyze the behavior of initial states that are superpositions of the three magnetic projections, but with a greater preference for one of them. These states are of the form:

$$\begin{aligned} |\psi_+\rangle &= \sqrt{\frac{8}{10}}|1\rangle + \frac{1}{\sqrt{10}}|-1\rangle + \frac{1}{\sqrt{10}}|0\rangle, & |\psi_-\rangle &= \frac{1}{\sqrt{10}}|1\rangle + \sqrt{\frac{8}{10}}|-1\rangle + \frac{1}{\sqrt{10}}|0\rangle, \\ |\psi_0\rangle &= \frac{1}{\sqrt{10}}|1\rangle + \frac{1}{\sqrt{10}}|-1\rangle + \sqrt{\frac{8}{10}}|0\rangle. \end{aligned} \quad (4.2)$$

In this way, these states indicate that they are mainly polarized in a certain magnetic projection but with a probability amplitude different from zero of being projected in a different magnetic projection. In this case, they are 80% polarized in the main magnetic projection and 20% in the remaining ones. This type of state is of interest because it is closer to real systems where complete polarization is not always possible. The behavior of the observables is depicted in Fig. 4.4.

As illustrated in Fig. 4.4, the change in the initial states of the system leads to noticeable variations in the behavior of the observables. Firstly, it becomes evident that the amplitudes of the corresponding probabilities of the states directly correlate with the average number of particles in each magnetic projection. Specifically, the contribution of a magnetic projection in a certain percentage within the superposition is reflected proportionally in the average number of particles. Since these contributions to the populations remain constant, both the quadrupole density and the magnetic density do not vary over time. This implies that the behavior of these observables can

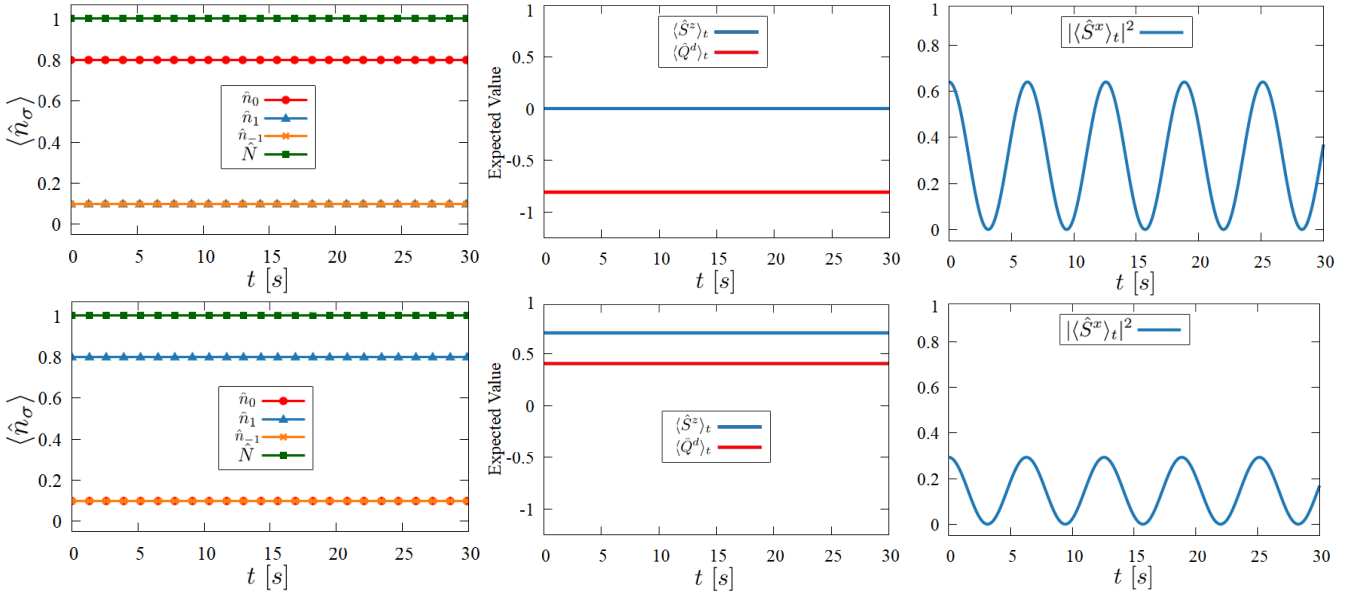


Figure 4.4: The expected value in time for the number of particles in each magnetic projection \hat{n}_σ (left), the quadrupolar density \hat{Q}^d together with the magnetic density \hat{S}^z (center), and the transverse magnetization \hat{S}^x (right) given the initial state $|\psi_0\rangle$ (top row) and $|\psi_\pm\rangle$ (bottom row) with $L = 30$, $J = 1$, $\mu = 1$, $D_0 = 1$, $T = 10^{-3}D_0$, and $m = 1$.

be inferred solely from the initial state, rendering them less significant in the dynamical analysis. Nevertheless, their respective values are presented when they are of relevance.

On the other hand, one of the most significant changes in the dynamics is the behavior of the transverse magnetization, which exhibits temporal oscillations in both cases. This reveals the first noticeable effect of the driving field on the system, directly influencing the spin fluctuations within the plane. Furthermore, it can be demonstrated that the amplitude and frequency of these oscillations are directly dependent on the probability amplitudes of the initial state and the magnitude of the coupling-field (see Appendix D). It is also worth noting that, only the states $|\psi_+\rangle$ and $|\psi_0\rangle$ are depicted, as the behavior of $|\psi_+\rangle$ and $|\psi_-\rangle$ is identical, with the only difference being an inversion in their populations ($\langle \hat{n}_1 \rangle \rightarrow \langle \hat{n}_{-1} \rangle$) and a sign change in the magnetic density ($\langle \psi_+ | \hat{S}^z | \psi_+ \rangle \rightarrow -\langle \psi_- | \hat{S}^z | \psi_- \rangle$).

Continuing with the analysis of the observables and their relations to the partially polarized initial states, one of the most intriguing outcomes is the behavior of the total spin and quadrupole contributions, as depicted in Fig. 4.5.

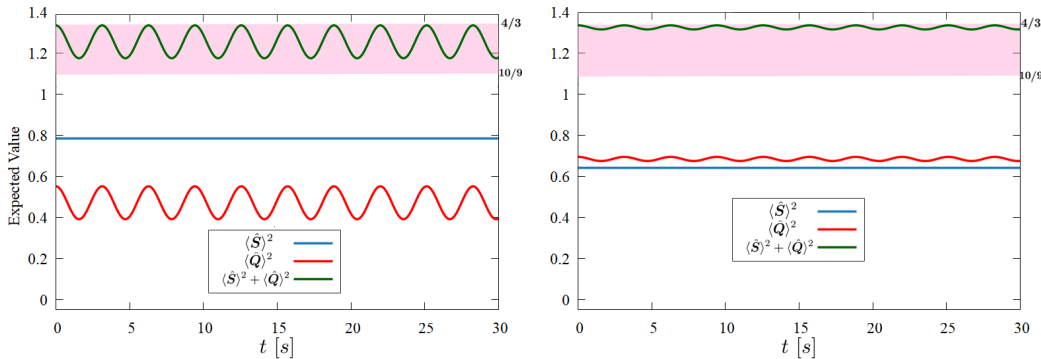


Figure 4.5: Spin-Quadrupole competition in time for the initial state $|\psi_{\pm}\rangle$ (left) and $|\psi_0\rangle$ (right) with $L = 30$, $J = 1$, $D_0 = 1$, $T = 10^{-3}D_0$, and $m = 1$.

As illustrated in Fig. 4.5, unlike polarized states, the superposition with a certain degree of polarization does not satisfy the equality in Eq. (2.31) over time. Instead, it satisfies an inequality where the upper bound is precisely $4/3$, i.e., $\langle \hat{S} \rangle_t^2 + \langle \hat{Q} \rangle_t^2 \leq 4/3$. This can be attributed to the presence of the linear Zeeman field. As demonstrated in Chapter 2, the linear field preferentially benefits one magnetic projection over time; energetically speaking, the magnetic states become completely distinguishable, with only the $| - 1 \rangle$ state minimizing the energy. This creates an imbalance among the states in the system, which is reflected in the spin order. To satisfy the equality, the spin order would need to oscillate in counterphase with the quadrupolar order. Since this does not occur, it indicates a clear breaking of the symmetry between the $|1\rangle$ and $| - 1\rangle$ states, specifically the time-reversal symmetry [87]. Furthermore, the driving applied in the field maintains a constant energy advantage for a single magnetic projection because it is a quadratic driving, i.e., of the form $D(t) = D_0 \cos^2(\omega t)$, ensuring that $D(t) > 0$ at all times. However, if this driving were linear, i.e., of the form $D(t) = D_0 \cos(\omega t)$, then over time, on average, the $|1\rangle$ and $| - 1\rangle$ states would benefit equally since $D(t)$ would frequently change sign. When $D(t) > 0$, the $| - 1\rangle$ state is favored, and when $D(t) < 0$, the $|1\rangle$ state is favored, leading, on average, to both states (or neither) benefiting over time, thereby restoring symmetry between the magnetic states on average. Consequently, their contributions to the spin and quadrupole are balanced, as depicted in Fig. 4.6 and the equality is fulfilled.

This phenomenon can also be understood analytically within the weak-driving regime or the rotating wave approximation (RWA). The RWA is based on averaging the contributions of the linear driving to zero and the quadratic driving to $1/2$, that is, $D(t) = D_0 \cos^2(\omega t) \rightarrow D_{\text{RWA}}(t) = D_0/2$ and $D(t) = D_0 \cos(\omega t) \rightarrow D_{\text{RWA}}(t) = 0$. Thus, in the case of quadratic driving, this is averaged to a

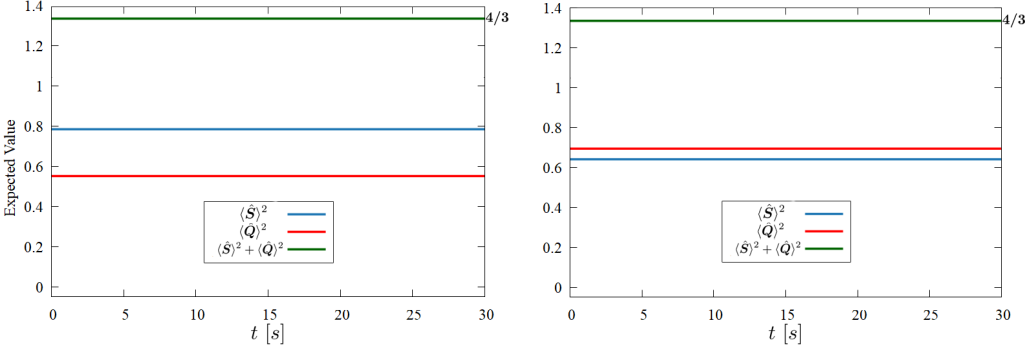


Figure 4.6: Spin-Quadrupole competition in time for the initial state $|\psi_{\pm}\rangle$ (left) and $|\psi_0\rangle$ (right) with $L = 30$, $J = 1$, $\mu = 1$, $D_0 = 1$, $T = 10^{-3}D_0$, $m = 1$ and a linear driving as a couple of the linear Zeeman field $D(t) = D_0 \cos(\omega t)$.

constant value, once again breaking the energetic symmetry of the magnetic states. In the case of linear driving, it is averaged to zero, causing the external field to disappear. Consequently, there is no lifting of the degeneracy of the magnetic projections in the system, meaning the system does not energetically favor any particular state, and we simply have a fully spin-1 particle.

Non-polarized initial state.

Finally, another possible case study of interest is that of an equiprobable initial state in each magnetic projection, i.e., a state of the form:

$$|\psi_{\sigma}\rangle = \frac{1}{\sqrt{3}}|1\rangle + \frac{1}{\sqrt{3}}|-1\rangle + \frac{1}{\sqrt{3}}|0\rangle, \quad (4.3)$$

this type of state does not have any privileged magnetic projection, making it more likely to be found in a sample that has not experienced any prior polarization process, such as an atom in a typical bosonic gas. Therefore, its analysis may be of particular interest.

As shown in Fig. 4.7, for a state that is equiprobable across all its magnetic projections, the transverse magnetization reaches its maximum value, the spin and quadrupole contributions again satisfy an inequality for the reasons previously discussed, but interestingly the minimum value of its oscillations falls on the value $10/9$, which is precisely the eigenvalue of the cubic Casimir operator of the group $SU(3)$. Thus the inequality stated above now has not only an upper limit but also a lower limit $10/9 \leq \langle \hat{S} \rangle_t^2 + \langle \hat{Q} \rangle_t^2 \leq 4/3$, such that the oscillation of constant values, fall within this band, as we can see in Figs. 4.7, 4.5 and in the subsequent ones. Additionally, it can be observed that in a superposition of this kind, both the magnetic density and the quadrupole density vanish,

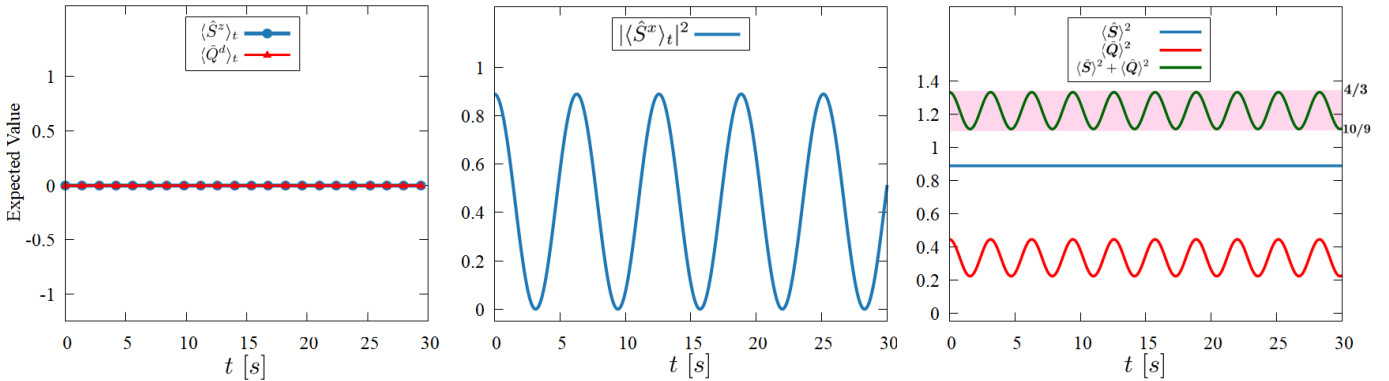


Figure 4.7: The expected value in time for the quadrupolar density \hat{Q}^d together with the magnetic density \hat{S}^z (left), the transverse magnetization \hat{S}^x (center) and Spin-Quadrupole competition (right) given the initial state $|\psi_\sigma\rangle$ with $L = 30$, $J = 1$, $\mu = 1$, $D_0 = 1$, $T = 10^{-3}D_0$, and $m = 1$.

indicating a clear equilibrium in the populations without meaning absence of dynamics in either sector. On the other hand, it is also useful to analyze the transverse magnetization along the y -axis to gain a more comprehensive perspective of the spin contributions.

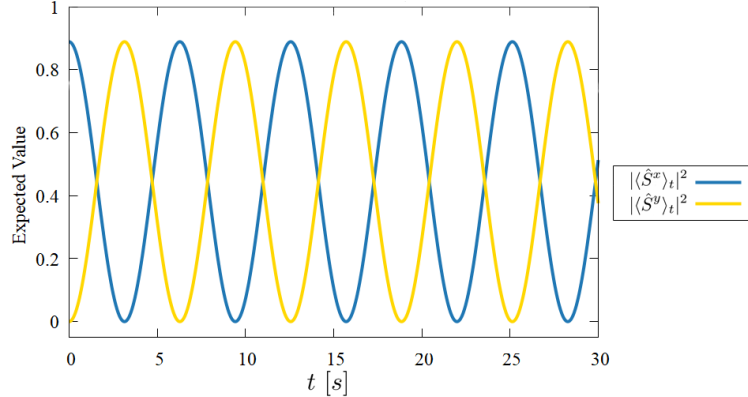


Figure 4.8: The expected value in time for the transverse magnetization \hat{S}^x and the transverse magnetization \hat{S}^y given the initial state $|\psi_\sigma\rangle$ with $L = 30$, $J = 1$, $\mu = 1$, $D_0 = 1$, $T = 10^{-3}D_0$, and $m = 1$.

As depicted in Fig. 4.8, the transverse magnetizations along x and y oscillate in counterphase. Moreover, since the populations do not change, the magnetic density remains constant, leading to a consistent sum of spin contributions, as seen in Fig. 4.7. This again indicates a broken symmetry between the magnetic states, which in this context can also be understood as isotropy in the spin fluctuations within the plane. This isotropy, along with the expectation values of the

operators \hat{S}^x and \hat{S}^y , can be interpreted through the typical effect observed in a spin-1/2 particle subjected to a linear magnetic field, known as spin precession [88]. Spin precession is a dynamic phenomenon predominantly studied in spin-1/2 particles, where a spin particle in a linear magnetic field experiences a kind of “torque” that attempts to align its spin orientation with the direction of the applied magnetic field. This causes the spin to precess around the axis along which the field is applied, in this case, the quantization axis z . Consequently, the expectation values of the spin components oscillate evenly in a plane, resulting in their average contributions remaining constant.

As we can see, this phenomenon is also applicable to spin-1 particles. The imposed linear field does not affect the non-magnetic projection ($|0\rangle$), allowing the magnetic projections ($|1\rangle$ and $| - 1\rangle$) to exhibit behavior similar to that observed in spin-1/2 particles. This effect occurs as long as there are contributions from both $|1\rangle$ and $| - 1\rangle$ projections in the initial state, causing the same precessional effect for each initial state studied and, hence, the imbalance between the spin and the quadrupole orders.

Thus far, we have only analyzed the dynamics within the weak-driving regime. As demonstrated, this regime falls within the RWA, meaning the true effect of the driving on the system has not yet been fully explored.

Case 2: Strong-Driving regime with a linear Zeeman field.

As previously mentioned, studying the strong-driving regime requires considering a sufficient number of harmonics to achieve a complete reconstruction of the state. However, if this period is extended excessively, such that $\omega \ll D_0$, the system enters a “low-frequency regime”, where, regardless of the number of harmonics considered, it becomes impossible to fully reconstruct the state using the extended Hilbert space method. Therefore, in the strong-driving regime, a period of the same order as the field coupling, $T = D_0 = 1$, $\omega = 2\pi$, is chosen. In this context, at least five harmonics $m = 5$, or equivalently 11 ($2m + 1$) blocks of the Floquet matrix, must be taken into account to ensure a reliable dynamic evolution.

To observe the real impact of driving on the system, we focus on the equiprobable magnetic projection superposition state $|\psi_\sigma\rangle$ Eq. (4.3). Under the weak-driving regime, we observed that the transverse magnetization and the quadrupolar contributions oscillate, as shown in Fig. 4.7. However, as previously noted, these oscillations are a consequence of the typical dynamic evolution of the system within the framework of the RWA and are not directly caused by the driving.

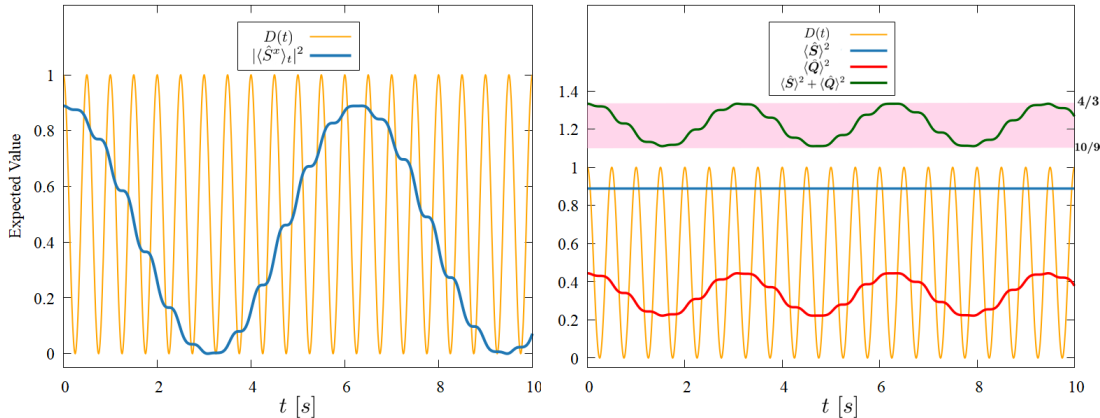


Figure 4.9: The expected value in time for the the transverse magnetization \hat{S}^x (left), Spin-Quadrupole competition (right) along with quadratic driving $D(t) = D_0 \cos^2(\omega t)$ given the initial state $|\psi_\sigma\rangle$ with $L = 30$, $J = 1$, $\mu = 1$, $D_0 = 1$, $T = D_0$, and $m = 5$.

With this in mind, Fig. 4.9 illustrates the genuine effect of driving on the system at frequencies comparable to the field, in the strong-driving regime, two types of oscillations can be recognized: one corresponding to the intrinsic dynamics of the system without periodic driving (i.e., within the RWA framework), referred to as slow dynamics, and another corresponding to the effect of driving on the system, which involves the slow dynamics, known as fast dynamics or micromotion (see Appendix B). The interplay between these two types of oscillations constitutes the overall dynamics of the system. The large oscillations primarily depend on the driving coupling D_0 , while the small oscillations depend mainly on the driving frequency ω . Furthermore, the shape of these small oscillations corresponds to the driving oscillations: when $D(t)$ reaches a maximum, the fast dynamics of the system, or the fast oscillations, tend to increase in amplitude, and when $D(t)$ reaches a minimum, these oscillations tend to decrease in amplitude. Additionally, it is evident that the spin order and the quadrupolar order continue to satisfy an inequality due to the presence of a linear field, although this dynamics is now accompanied by the small oscillations.

It is also possible to analyze the case where the system is subjected to linear driving, $D_0 \cos(\omega t)$, which, as illustrated in Fig. 4.6, reestablishes the symmetry completely or upto some low-amplitude oscillations due to the RWA. However, in the strong-driving regime, the true effect of this linear driving can be observed in Fig. 4.10. The dynamics are once again composed of slow dynamics, which in this case show a constant value as seen in Fig. 4.6, and fast dynamics, which manifest as oscillations. Notably, in this strong-driving regime, the equality of Eq. (2.31) is not fully

reestablished, unlike the case of the RWA with linear driving. This discrepancy arises because the driving oscillations are not sufficiently rapid, allowing the system to capture the advantages in each magnetic projection.

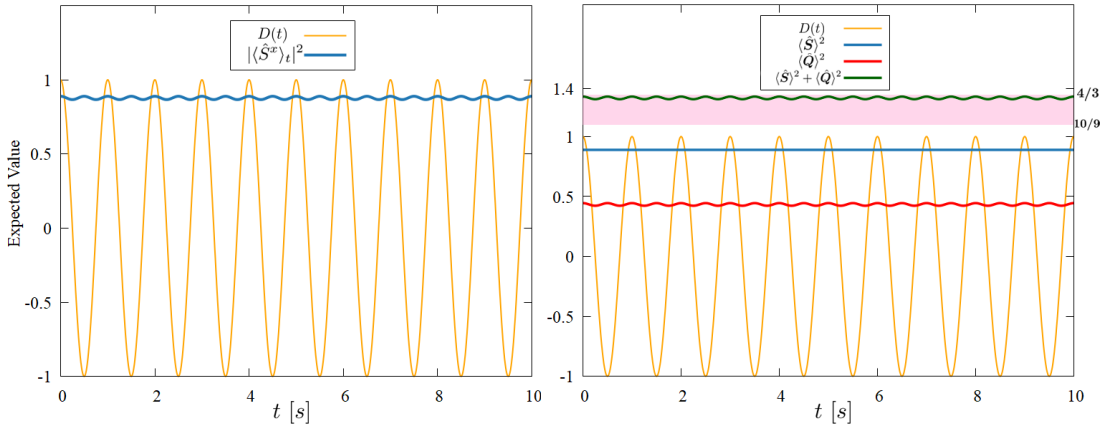


Figure 4.10: The expected value in time for the transverse magnetization \hat{S}^x (left), Spin-Quadrupole competition (right), along with linear driving $D(t) = D_0 \cos(\omega t)$ given the initial state $|\psi_\sigma\rangle$ with $L = 30$, $J = 1$, $\mu = 1$, $D_0 = 1$, $T = D_0$, and $m = 5$.

The analysis conducted for the previously established frequency may still be considered as corresponding to a high-frequency regime. However, as noted earlier, a substantial increase in the driving period destabilizes the system's dynamics, such that the fast dynamics dominate over the slow dynamics, making it impossible to separate them, which is fundamental to Floquet's theorem. In this situation, regardless of the number of harmonics considered, the state is not accurately reconstructed. An example of this scenario is provided in Appendix D, where alternative approaches for evolving the system in this low-frequency regime are also discussed.

We now observe that, for a periodic linear field, the dynamics exhibited by a spin-1 boson align with the expected values for a time-independent system or even with those expected for spin-1/2 systems, with periodic variations in these values. However, as demonstrated, the presence of the linear field disrupts the symmetry between the magnetic states of the system, leading to effects such as spin precession and consequently preventing equalities such as Eq. (2.31), which are unique to spin-1 particles, from being fully satisfied. Despite this, it is evident that the impact of a periodic driving field on such systems primarily involves introducing small oscillations into the system's dynamics (in addition to the dynamics induced by the field) in the strong regime, and facilitating the dynamic description of the system even without direct action in the weak regime.

4.1.2 Quadratic Zeeman Field

Having analyzed the case of a linear field, we now turn our attention to the dynamics of the system under a quadratic field, which, as demonstrated in Chapter 2, energetically benefits the magnetic states equally. In this scenario, we consider both the weak and strong regimes, now with an expanded understanding of the behavior of each regime. For this analysis, we utilize the Hamiltonian from Eq. (2.22) with the values $L = 30$, $J = \mu = Q_0 = 1$, and $T = 10^{-3}Q_0$ for the weak regime, and $L = 30$, $J = \mu = Q_0 = 1$, and $T = Q_0$ for the strong regime. Additionally, we analyze the dynamics coming out with the same initial states as before.

Case 3: Weak-Driving regime with a Quadratic Zeeman field.

Fully polarized initial states do not provide an interesting dynamics as it was already shown in Figs 4.1 and 4.2 regardless the magnetic field. Hence, let us start with partially polarized initial states $\{|\psi_+\rangle, |\psi_-\rangle, |\psi_0\rangle\}$, where the field plays a significant role in the dynamics. Figs. 4.11 and 4.12 shows, how the relationship $\langle \hat{\mathbf{S}} \rangle^2 + \langle \hat{\mathbf{Q}} \rangle^2 = 4/3$ is now fully satisfied, demonstrating that the initial states proposed, evolve displaying both spin and quadrupole orders, since the time-reversal symmetry is preserved and causing the spin and quadrupole contributions complement each other in counterphase. Additionally, it is noteworthy that in this scenario, the transverse magnetization components x and y continue to oscillate in counterphase (or remain equal to 0 in the case of the state $|\psi_0\rangle$). However, these oscillations no longer exhibit the same amplitude, causing the total spin order to oscillate accordingly.

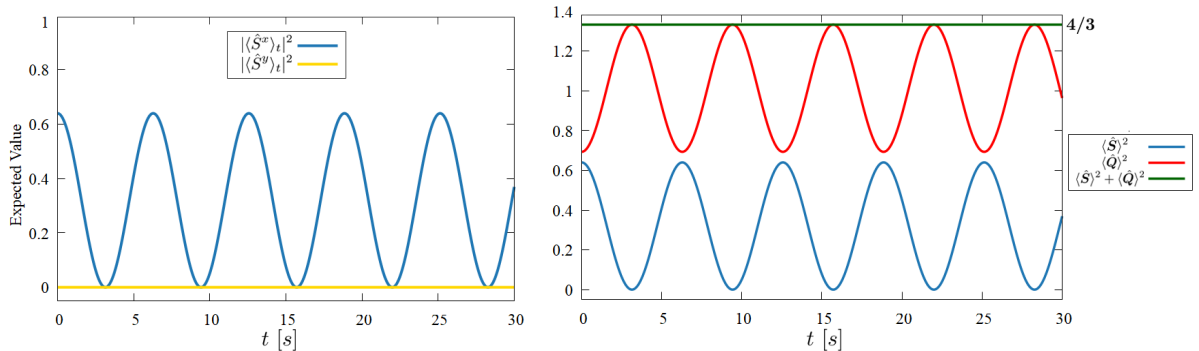


Figure 4.11: The expected value in time for the transverse magnetization x and y \hat{S}^x , \hat{S}^y (left), and Spin-Quadrupole competition (right), given the initial states $|\psi_0\rangle$ with $L = 30$, $J = 1$, $\mu = 1$, $Q_0 = 1$, $T = 10^{-3}Q_0$, and $m = 1$.

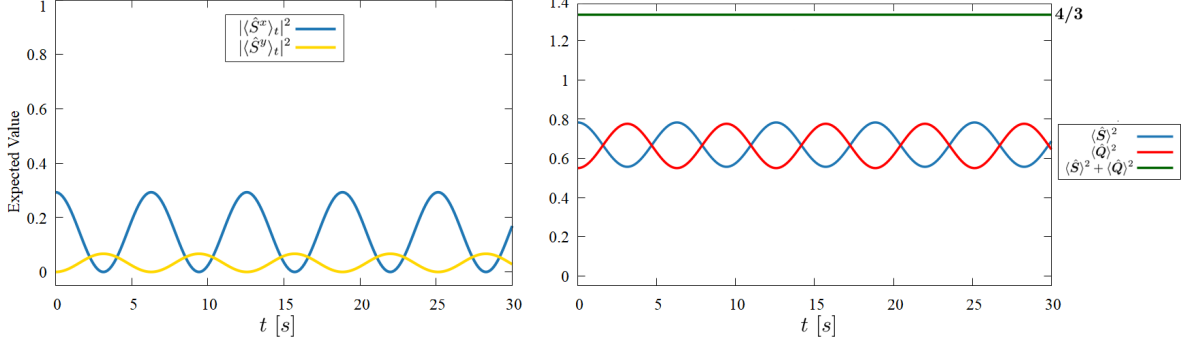


Figure 4.12: The expected value in time for the transverse magnetization x and y \hat{S}^x , \hat{S}^y (left), and Spin-Quadrupole competition (right), given the initial state $|\psi_{\pm}\rangle$ with $L = 30$, $J = 1$, $\mu = 1$, $Q_0 = 1$, $T = 10^{-3}Q_0$, and $m = 1$.

A similar behavior can also be observed in the state with equiprobable magnetic projections, $|\psi_{\sigma}\rangle$ Eq. (4.3), as depicted in Fig. 4.13. For this equiprobable initial state, we again observe both spin order and quadrupole order competing in time while satisfying their $4/3$ equality. The transverse magnetization component x also reaches its maximum amplitude, and spin fluctuations are observed exclusively along this axis, indicating an anisotropy in the spin fluctuations that favors the spin order for its oscillations. Furthermore, this suggests that the presence of a quadratic field no longer exerts a torque on the spin of the particle, thereby preventing spin precession around the z axis. As a result, the particle deviates from the typical spin- $1/2$ behavior and instead exhibits the orders expected for a spin-1 particle.

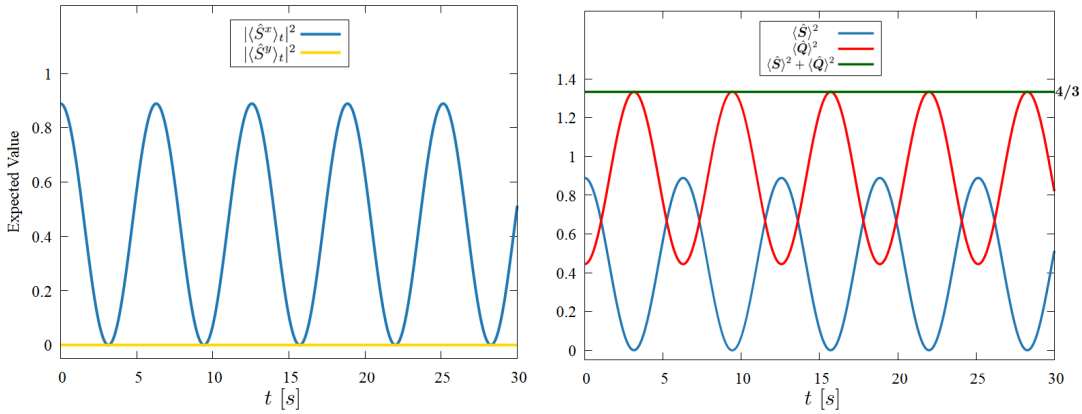


Figure 4.13: The expected value in time for the transverse magnetization x and y \hat{S}^x , \hat{S}^y (left), and Spin-Quadrupole competition (right), given the initial state $|\psi_{\sigma}\rangle$ with $L = 30$, $J = 1$, $\mu = 1$, $Q_0 = 1$, $T = 10^{-3}Q_0$, and $m = 1$.

Note also that, given the initial states presented above, their respective quadrupole and magnetic densities were not depicted. This omission is due to the fact that, as mentioned earlier, the populations of these states remain invariant over time, meaning the observables do not change. Consequently, the values depicted in Figs. 4.4 and 4.7 for a quadratic field are maintained.

It is also possible to analyze the scenario where a linear driving field ($Q_0 \cos \omega t$), rather than a quadratic one ($Q_0 \cos^2 \omega t$), is coupled to the quadratic Zeeman field (\hat{S}^z)². However, as demonstrated with the linear field, in the weak-driving regime, the field averages to zero under the RWA. Therefore, this scenario exhibits the same behavior as previously studied in Fig. 4.6.

Thus, we observe that for the quadratic Zeeman field in the weak-driving regime, the dynamic behavior is similar to that seen with the linear field. However, the key difference is that the quadratic field preserves the symmetry between the states $|1\rangle$ and $| - 1\rangle$ and does not induce spin precession. This results in a clear competition between the spin and quadrupolar order. Nevertheless, the true effect of periodic driving is revealed when analyzing the strong-driving regime, where, as seen in the linear field case, a fast dynamics behavior is anticipated.

Case 4: Strong-Driving Regime with a quadratic Zeeman field.

Taking into account the behavior observed in the strong-driving regime for the linear field, we now focus exclusively on analyzing the equiprobable state $|\psi_\sigma\rangle$, to confirm the separation between fast and slow dynamics in the context of a quadratic Zeeman field. Consequently, the evolution of the other initial states can be inferred from this analysis.

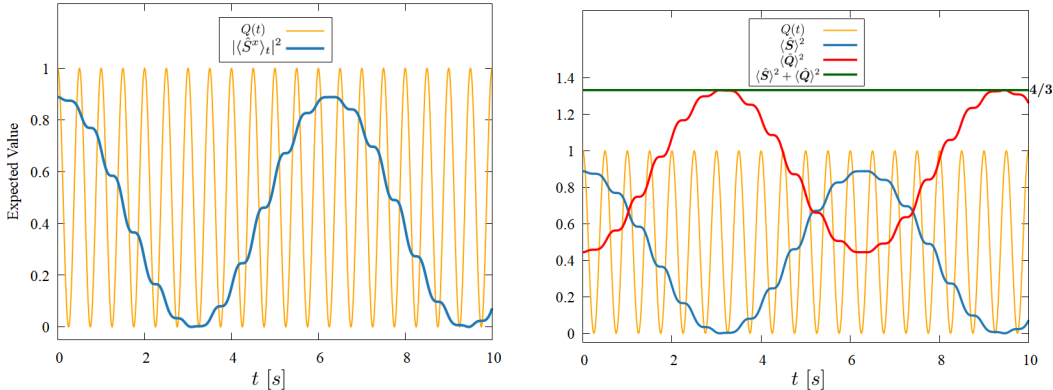


Figure 4.14: The expected value in time for the transverse magnetization \hat{S}^x (left), Spin-Quadrupole competition (right), along with quadratic driving $Q(t) = Q_0 \cos^2(\omega t)$ given the initial state $|\psi_\sigma\rangle$ with $L = 30$, $J = 1$, $\mu = 1$, $Q_0 = 1$, $T = Q_0$, and $m = 5$.

Fig. 4.14 shows the expected behavior of both the transverse magnetization (left panel) and the spin-quadrupole competition (left panel) is depicted for the strong-driving regime. The dynamics consist of a slow component and a fast component, similar to the linear case, but with micromotion that encapsulates the slow dynamics.

Interestingly, in this strong-driving regime with a quadratic field, if we consider a linear driving $Q(t) = Q_0 \cos(\omega t)$, the spin contributions also oscillate, periodically satisfying both the spin and quadrupole order equality.

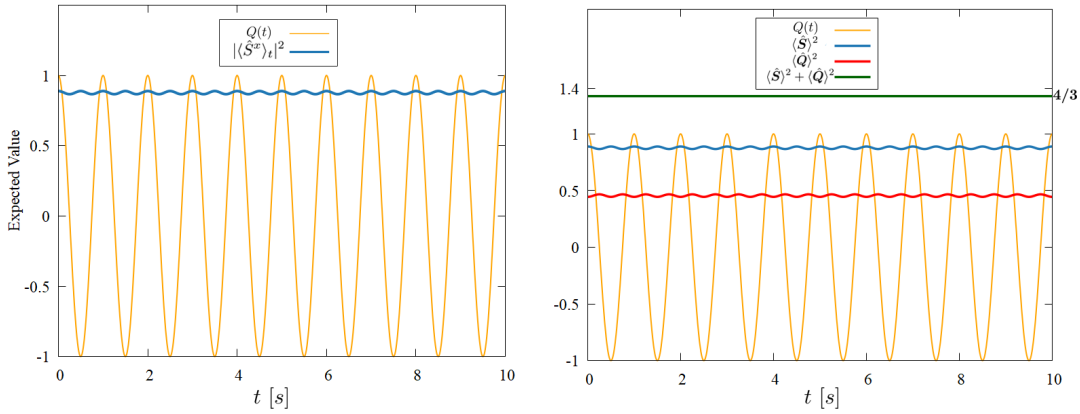


Figure 4.15: The expected value in time for the the transverse magnetization \hat{S}^x (left), Spin-Quadrupole competition (right), along with linear driving $Q(t) = Q_0 \cos(\omega t)$ given the initial state $|\psi_\sigma\rangle$ with $L = 30$, $J = 1$, $\mu = 1$, $Q_0 = 1$, $T = Q_0$, and $m = 5$.

In Fig. 4.15, the difference between the effects of a quadratic Zeeman field (\hat{S}^z)² and a linear one (\hat{S}^z) is explicitly illustrated. While the linear field disrupts the internal symmetries of the magnetic states in the system, leading to spin precession and constant spin contributions, the quadratic field preserves the symmetry between the magnetic states, thereby preventing phenomena such as spin precession. As a result, the spin order oscillates and maintains competition with the quadrupolar order, regardless of whether the driving is linear or quadratic.

Thus, the dynamic analysis of a spin-1 particle through Floquet theory enables the exploration of various scenarios in its dynamic evolution. By coupling the driving to an external field, its effects can be clearly observed, either in a constant manner (weak regime) or periodically (strong regime). Although many more parameters and states can be varied, it is evident that the nature of the field —linear or quadratic— significantly influences the evolution of a spin-1 state, with the quadratic field being preferable for preserving the symmetries of the magnetic projections. For a

more detailed analysis, additional findings are presented in Appendix D.

Having studied the dynamics of a single spin-1 boson, it becomes captivating to consider the scenario where an additional particle is included. This introduces not only the effects previously observed but also the interactions between particles, providing insights that more closely resemble the behavior of a real system.

4.2 Two particles

To demonstrate the dynamic behavior of our two-particle system, it is essential to primarily consider the interactions that emerge, as well as establish the parameters and conditions of the system. In doing so, we adhere the steps outlined in the previous chapter concerning the numerical implementation, while specifying the particularities unique to the two-particle system.

1. Set the initial parameters: The two-particle system, the Hamiltonian that models this scenario is given by Eq. (2.24), which includes the interaction between particles through their spin projections and accounts for phenomena such as spin mixing. With this in mind, we define the number of sites to be analyzed. The choice of the number of sites is numerically crucial due to the exponential growth of the system's state space. In this case, we aim to describe all possible states that can involve up to two particles across the entire optical lattice, resulting in a local basis with 10 states, as follows:

$$\begin{aligned} & \text{1) } |\emptyset\rangle, \quad \text{2) } |1, 0, 0\rangle, \quad \text{3) } |0, 1, 0\rangle, \quad \text{4) } |0, 0, 1\rangle, \\ & \text{5) } |1, 1, 0\rangle, \quad \text{6) } |1, 0, 1\rangle, \quad \text{7) } |0, 1, 1\rangle, \\ & \text{8) } |2, 0, 0\rangle, \quad \text{9) } |0, 2, 0\rangle, \quad \text{10) } |0, 0, 2\rangle, \end{aligned} \tag{4.4}$$

where, the notation $|n_1, n_{-1}, n_0\rangle$ indicates the number of particles n_σ in each magnetic projection.

Now, as we can see, the number of states in the system grows as $N_T = 10^L$, but, as explained in the case of a single particle, not all states are physically relevant, potentially allowing for a reduction in this exponential growth. However, in the case of a two-particle system, the construction of an effective basis is not as straightforward as in the single-particle case. Therefore, the selection and treatment of only effective states become impractical. Consequently, it is more straightforward to use all possible states as given by the Kronecker product and to ensure accurate evolution by simply initializing states that are physically realizable. Nevertheless, despite being more practical

manually, this approach becomes significantly more computationally demanding. For instance, if we were to use the same number of sites as in the single-particle case ($L = 30$), our code would need to handle a matrix with at least 10^{60} complex entries, which exceeds the capabilities of any conventional computer. Therefore, in this case, the number of sites to be worked on and analyzed is set to the minimum possible, that is, $\mathbf{L} = \mathbf{2}$, with additional explorations and studies involving an extra site provided in Appendix D.

Regarding the other parameters of the Hamiltonian, we must consider the two phases present in the system: the ferromagnetic phase and the antiferromagnetic phase, as explained in Chapter 2. For the antiferromagnetic phase, it was shown that the interaction forces must follow a given relation, $U_2 = 0.036U_0$, to establish a scenario similar to that of ^{23}Na [45]. However, this relation holds for a three-dimensional system which was analyzed by means of the mean-field approximation and the deep lattice Hamiltonian. In our case study, we allow free hopping between neighbors mediated only by the hopping term, so in order to observe a significant interaction, we must set the relation between the interaction forces to a higher value than usual, specifically $U_2 = 0.4U_0$. On the other hand, it can be shown that the charge scattering interaction strength U_0 can be expressed in terms of the hopping ratio J and the number of neighboring sites z (which is equal to unity since we consider $L = 2$), such that $U_0 = 2zJ$. Therefore, the system for the antiferromagnetic phase is based on our energy unit J , which we then set to $\mathbf{J} = \mathbf{0.1}$, resulting in $\mathbf{U}_0 = \mathbf{0.2}$ and $\mathbf{U}_2 = \mathbf{0.08}$.

For the ferromagnetic phase, the interaction strengths can also be established in relation to the hopping term, with the difference being a sign change in the spin scattering term, such that $U_2 = -0.005U_0$, exemplifying a scenario similar to that of ^{87}Rb [45]. However, this proportion between the interaction terms is too low to observe clear dynamics in our system, so it is increased such that $U_2 = -0.1U_0$. Thus, for the ferromagnetic phase, we again define $\mathbf{J} = \mathbf{0.1}$, resulting in $\mathbf{U}_0 = \mathbf{0.2}$ and $\mathbf{U}_2 = \mathbf{-0.02}$.

Once the interaction parameters are defined, our objective is to study the system under the influence of a quadratic Zeeman field. This field is initially imposed as periodic; however, as shown in the single-particle case, the periodicity primarily affects the system's typical evolution through micro-motions. Therefore, we analyze the field just in a constant manner by coupling a quadratic driving in the weak-driving regime, i.e., $Q(t) = Q_0 \cos^2(\omega t)$, with $T = 10^{-3}Q_0$, which is equivalent to a field coupling of the form $\mathbf{Q}_0/2$. Given this, a single harmonic is sufficient for a reliable study. Finally, we set the last parameter of the system, the chemical potential, to a value that allows us

to clearly observe the dynamics, $\mu = 1$.

2. Generate the local and non-local matrix of the Hamiltonian: The Hamiltonian is built using the Kronecker product (see Appendix C). Since the system under consideration consists of only two sites, this process is applied to all terms except for the hopping term which, being a matrix that directly involves two sites, is manually incorporated into the code by explicitly calculating the non-zero matrix elements.

3. Generate the Floquet Matrix: Once we have obtained the Hamiltonian that describes our complete system of two sites, we generate the Floquet matrix as specified in Eq. (3.13) with one harmonic. This matrix has a dimension of 300×300 , representing a computational cost similar to that of the single-particle case.

4. Diagonalization and state reconstruction: We diagonalize the Floquet matrix as outlined in the numerical implementation and completely reconstruct the state for any time t in time steps of $\delta t = 0.1$ s, clearly specifying the initial evolved state in each case. The initial states are chosen based on experimentally realizable scenarios. In this case, we focus on states that satisfy the balanced mixture condition to ensure that the contribution of neither linear Zeeman nor linear driving have to be taken into account. Then, we consider a two-particle polarized state with both in a 0 magnetic projection, $|0, 0, 2\rangle$, such that spin-changing and spin-preserving collisions can be observed.

5. Measurement of observables: Finally, we measure the relevant observables, including the average number of total particles in each magnetic projection, $\langle \hat{n}_\sigma \rangle$, the total magnetic density, $\langle \hat{S}^z \rangle$, the total quadrupole density, $\langle \hat{Q}^d \rangle$, and the transverse magnetization, $|\langle \hat{F}^x \rangle|^2$, where these last three operators have been previously divided by a factor 2 since there are two particles and we want to follow their response per particle

These considerations yield the following suitable parameters for the two-particle system:

- $L = 2$, $J = 0.1$, $\mu = 1$, $U_0 = 0.2$, $U_2 = 0.08$, $T = 10^{-3}Q_0$, and $m = 1$ for the antiferromagnetic phase.
- $L = 2$, $J = 0.1$, $\mu = 1$, $U_0 = 0.2$, $U_2 = -0.02$, $T = 10^{-3}Q_0$, and $m = 1$ for the ferromagnetic phase.

This section should be read in conjunction with Appendix D, which further explores scenarios involving an increased number of sites that contribute to a deep analysis of the system.

4.2.1 Antiferromagnetic phase $U_2 > 0$

The antiferromagnetic phase occurs when $U_2 > 0$ and is characterized by favoring the antialignment of the spins, prioritizing configurations where there is no net magnetization or it reaches its minimum value $|\langle \hat{\mathbf{F}} \rangle| = 0$.

Evolution without a magnetic field.

As demonstrated in the single-particle system, the weak-driving regime is equivalent to the RWA. Under this approximation, a linear driving causes the coupled term to vanish. Therefore, to understand how a quadratic Zeeman field influences our two-particle system, we first couple a linear driving, $Q(t) = Q_0 \cos(\omega t) \rightarrow Q_{\text{RWA}}(t) = 0$, so that the dynamics are primarily controlled by the interaction terms. We consider the case of two polarized particles in the 0 magnetic projection.

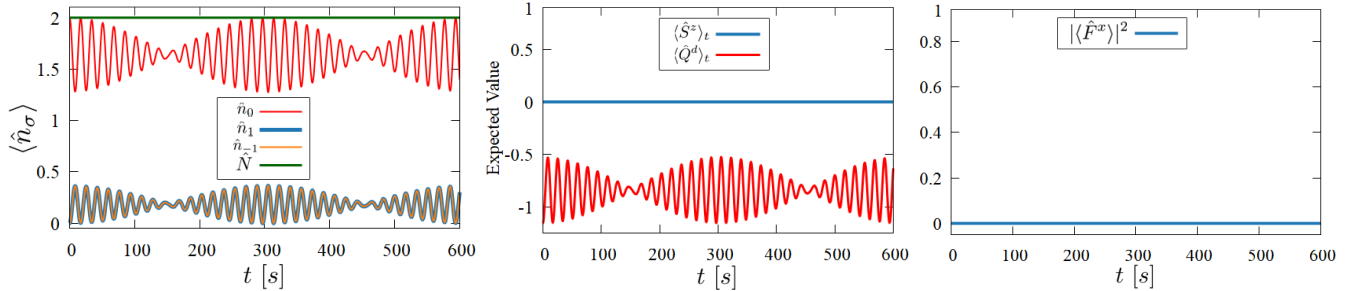


Figure 4.16: The expected value in time for the number of particles in each magnetic projection \hat{n}_σ (left), the quadrupolar density \hat{Q}^d together with the magnetic density \hat{S}^z (center) and the transverse magnetization \hat{F}^x (right) given the initial state $|0, 0, 2\rangle$ with $L = 2$, $J = 0.1$, $\mu = 1$, $U_0 = 0.2$ and $U_2 = 0.08$.

As shown in Fig. 4.16, the dynamical evolution of the two-particle system is characterized by a continuous exchange of populations between the 0, 1, and -1 magnetic projections. This behavior explicitly illustrates spin-changing collisions, or spin mixing, which occurs between the states $|0, 0, 2\rangle$ and $|1, 1, 0\rangle$, describing the transition from the annihilation of two particles in the 0 magnetic projection to the creation of two particles in the 1 and -1 magnetic projections. It is important to note that due to this exchange in populations, the quadrupole density also plays a role in the dynamics. On the other hand, since we have a balanced mixture condition, both the magnetic density and the transverse magnetization remain constant at zero, rendering them less relevant in the dynamic analysis.

On the other hand, we can observe that the change in populations manifests as modulated oscillations, where at certain moments these oscillations appear to cease, only for the amplitude to grow again and re-activate the dynamics. These points are referred to as collapses and revivals in the context of quantum optics, and are extensively studied in systems such as the Jaynes-Cummings model [89]. This phenomenon can be understood as follows: Initially, the quantum system may be in a coherent or superposition state, with all contributions in the superposition being in phase, thereby combining constructively. However, due to the internal dynamics of the system, in this case, interactions, this coherence can decrease as the different components of the superposition begin to interfere destructively with each other. This process leads to an apparent loss of coherence, resulting in a “collapse”, where the system’s dynamics seem to disappear. However, after a period of collapse, the terms in the quantum superposition can re-synchronize due to the system’s inherent periodicity. As a result, the coherence of the system can be partially or fully restored, leading to a “revival” of the dynamics. Therefore, we show that this phenomenon can also occur in dynamical spin-1 systems [45].

It is worth examining the competition between quadrupolar order and spin order, particularly since we have spin-1 particles, together with nonlocal spin-1 states. Fig. 4.17 shows the competition between quadrupolar and spin order, now significantly more complex than in the single-particle case, presenting oscillations that deviate considerably from those previously observed, making the analysis more challenging, with three frequencies: the two presented in the single particle case plus a periodic envelope. In the latter is noteworthy that at $t = 0$, and at regular intervals, the expected relation is fulfilled, adding up to the value of $4/3$, while deviating from this relation at other times. This can be understood by considering that the initial state is a completely a spin-1 local state. Even with two particles, the state is expected to follow the relation perfectly. However, as the transition $|0, 0, 2\rangle \leftrightarrow |1, 1, 0\rangle$ occurs, the resulting states are no longer typical spin-1 states but rather combinations of such states across various sites, with different contributions. As a result, the relation given by Eq. (2.31) is no longer strictly followed. Despite this, it is important to note that the maximum peak still corresponds to the eigenvalue of the SU(3) quadratic Casimir operator, conditioning the system to this symmetry group and maintaining the inequality $\langle \hat{\mathbf{S}} \rangle_t^2 + \langle \hat{\mathbf{Q}} \rangle_t^2 \leq \frac{4}{3}$, but only with the upper bound.

Having seen the dynamic evolution of the system in the absence of the quadratic Zeeman field, let us now see how its presence can affect it for different amplitudes of the coupling.

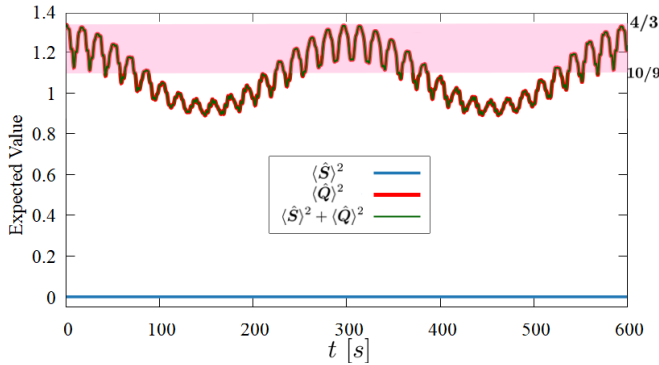


Figure 4.17: The expected value in time for the Spin-Quadrupole competition given the initial state $|0, 0, 2\rangle$ with $L = 2$, $J = 0.1$, $\mu = 1$, $U_0 = 0.2$ and $U_2 = 0.08$.

Effects of quadratic Zeeman magnetic field.

To examine the effects of the quadratic Zeeman field on the system, we consider a quadratic driving as coupling, such that in the RWA, this can be interpreted as a constant coupling, $Q(t) = Q_0 \cos^2(\omega t) \rightarrow Q_{\text{RWA}}(t) = \frac{Q_0}{2} = Q'_0$. In this context, we must first recognize that depending on the strength of this coupling relative to the interaction strength, two distinct regimes are identified: the interaction regime, where $Q'_0 < 2U_2$, and the Zeeman regime, where $Q'_0 > 2U_2$ [90].

In Fig. 4.18, we can distinguish between the interaction and Zeeman regimes. In the interaction regime, they dominate, leading to longer spin mixing cycles, fewer collapse-revival events, and a more gradual transition between the two states of the system with fewer modulations. Conversely, in the Zeeman regime, the Zeeman field dominates the system, limiting interactions and resulting in higher frequency oscillations with lower amplitudes. If the field is significantly stronger than the interaction strength, the system ceases to interact and maintains the same initial state over time. This behavior in the Zeeman regime is also recognized in the context of quantum optics as off-resonant Rabi oscillations [90].

An interesting case arises when the amplitude of the field is precisely at the threshold between both regimes, $Q'_0 = 2U_2$. In this situation, the system exhibits a phenomenon known as “spin-mixing resonance” [90], where the effects of the external mangetic field and the interaction are perfectly in phase. This results in oscillations with maximum amplitudes and very high frequencies that do not decay over time, as illustrated in Fig. 4.19. In this specific simulation, the resonance was not obtained exactly at the value $Q'_0 = 2U_2$, but rather at $Q'_0 \approx 1.61U_2$. This deviation occurs because the initial coupling is not constant; instead, it is a quadratic driving that, due to the weak-driving

regime (RWA), we approximate as constant. Consequently, this approximation influences the precise numerical value of the resonance. However, the resonant behavior of the system between the interaction and the external magnetic field is clearly in agreement.

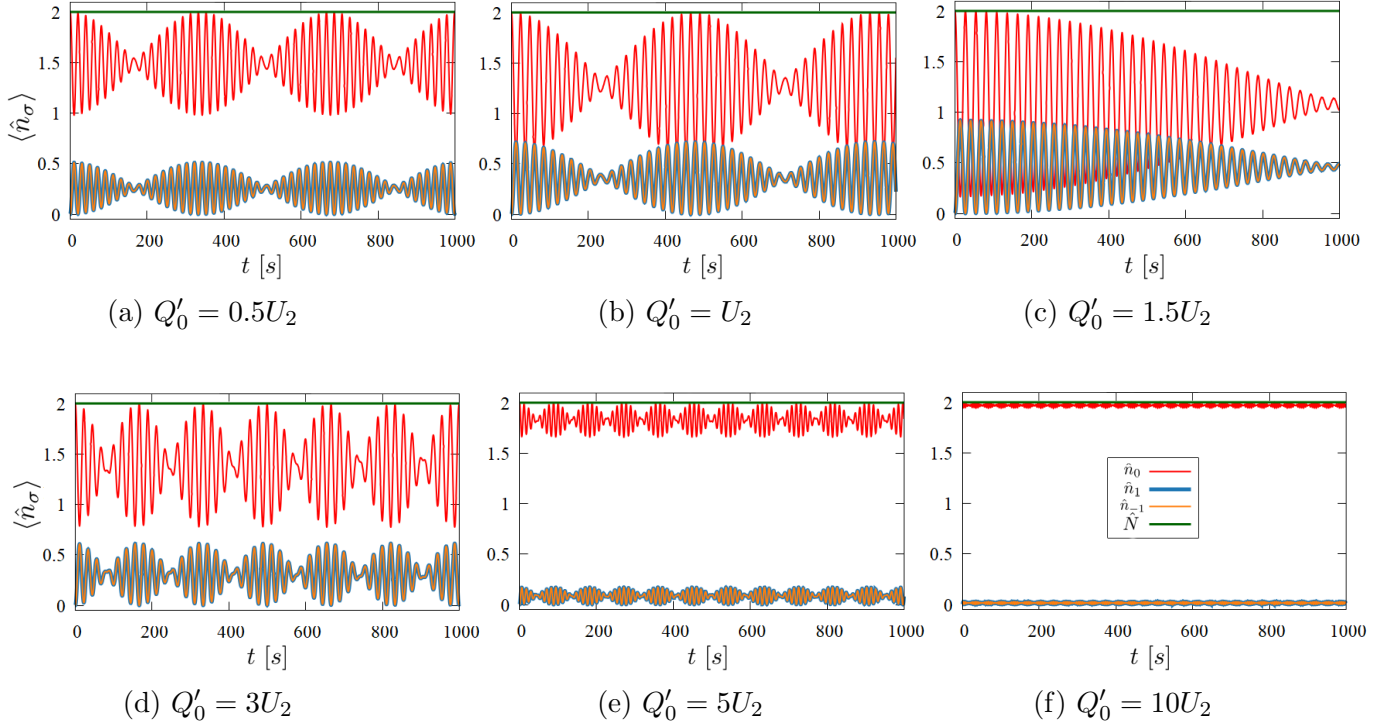


Figure 4.18: Spin mixing dynamics, for different values of the quadratic Zeeman coupling in the interaction regime (top row) and the Zeeman regime (bottom row) with $L = 2$, $J = 0.1$, $\mu = 1$, $U_0 = 0.2$ and $U_2 = 0.08$. All graphs share the same key as subfigure (f).

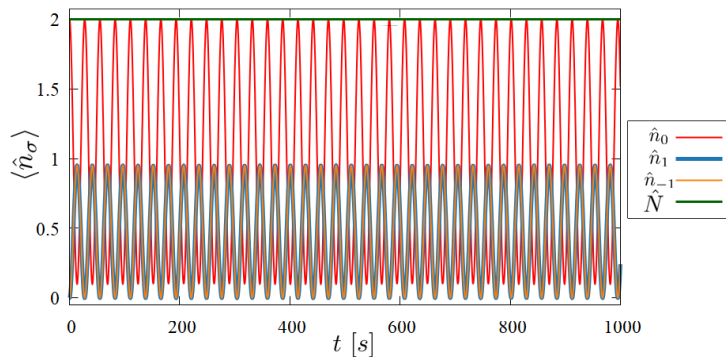


Figure 4.19: Spin mixing dynamics for the limit between the interaction regime and the Zeeman regime. In our system, the spin-mixing resonance is observed at $Q'_0 \approx 1.61U_2$.

This resonance phenomenon can be understood by drawing an analogy to a classical system of a forced pendulum: when the forcing frequency equals the natural frequency of the pendulum, maximum oscillations are achieved. Similarly, when the magnitude of the quadratic Zeeman field equals the interaction strength present in the system, these interactions are significantly enhanced. As a result, as shown in the figure, an almost complete transition is observed in the transformation from the state $|0, 0, 2\rangle$ to the state $|1, 1, 0\rangle$, demonstrating that the interaction within the system reaches its maximum intensity.

4.2.2 Ferromagnetic phase $U_2 < 0$

The ferromagnetic phase occurs when $U_2 < 0$ and is characterized by favoring the alignment of spins, prioritizing configurations where there is maximum net magnetization $|\langle \hat{\mathbf{F}} \rangle| = 1$.

Evolution without magnetic field.

The ferromagnetic phase prioritizes magnetization, however if the initial state is not magnetized, this is also preserved over time, so that the dynamics of the system without a field can be seen in the following figure given the same initial state polarized at 0.

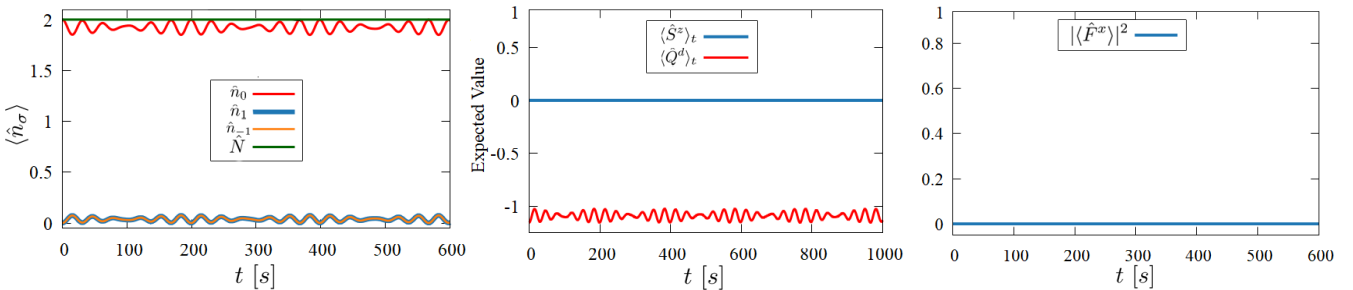


Figure 4.20: The expected value in time for the number of particles in each magnetic projection \hat{n}_σ (left), the quadrupolar density \hat{Q}^d together with the magnetic density \hat{S}^z (center) and the transverse magnetization \hat{F}^x (right) given the initial state $|0, 0, 2\rangle$ with $L = 2$, $J = 0.1$, $\mu = 1$, $U_0 = 0.2$ and $U_2 = -0.02$.

In Fig. 4.20, the ferromagnetic phase exhibits oscillations, as the collapses and revivals, but much smaller. This is because, as mentioned, the ferromagnetic phase prioritizes configurations with aligned spins, and given our initial state, only transformations between non-aligned states occur, which affects the dynamics.

Effects of magnetic field.

The ferromagnetic phase is influenced by a quadratic Zeeman field, with the dynamics separating into the same two regimes: the interaction regime and the Zeeman regime, with the boundary between them marked by the spin-mixing resonance.

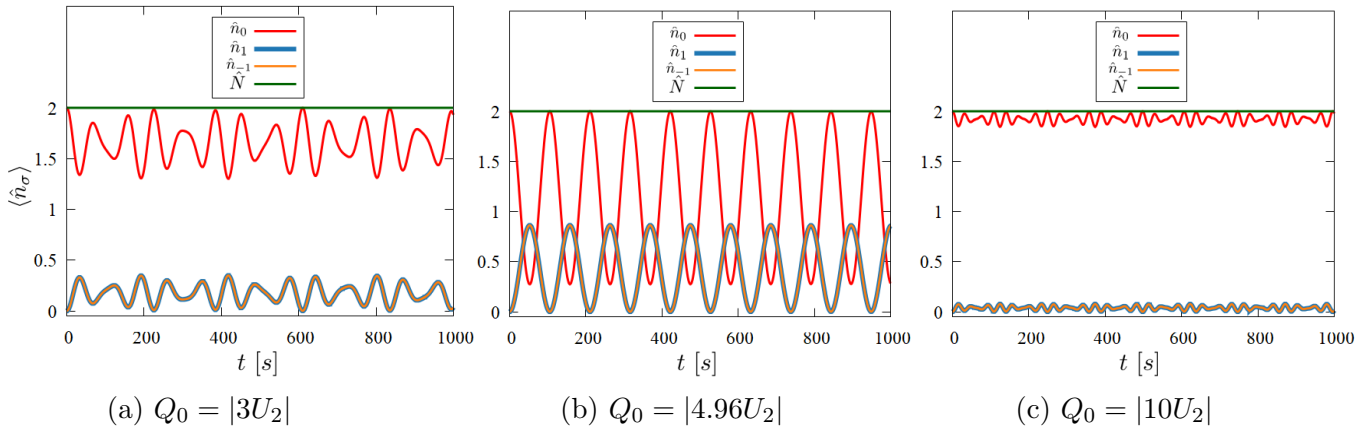


Figure 4.21: Spin mixing dynamics, for different values of the quadratic Zeeman coupling in the interaction regime (left), spin-mixing resonance (center) and the Zeeman regime (right)

Fig. 4.21 displays the fact that, the ferromagnetic phase under a quadratic Zeeman field exhibits three regimes as well: interaction regime, a Zeeman regime, and a intermediate one where spin-mixing resonance occurs. Note that the value at which spin-mixing resonance is observed differs significantly from the one predicted analytically, $Q'_0 = |2U_2|$, due to the reasons previously discussed. Additionally, the required field strength for resonance is larger, indicating that the system's preference for aligned spins necessitates a stronger field to achieve resonance with the interaction, especially since the initial state transitions between states with non-aligned spins.

In summary, when analyzing the evolution of systems starting from states such as $|\psi_\pm\rangle$, $|\psi_\sigma\rangle$, or $|0, 0, 2\rangle$ under a linear or quadratic field, as illustrated in Figs. 4.5, 4.7, 4.13, and 4.17, it becomes evident that the oscillations or stable values of the spin and quadrupole orders consistently fall within two specific limits: an upper limit and a lower limit. Notably, when the oscillations are maximal, as in the case of the state $|\psi_\sigma\rangle$, these limits correspond to the eigenvalues of the quadratic and cubic Casimir operators, respectively. Thus, it appears that for any **local** spin-1 state within a linear or quadratic field, the competition between quadrupolar and spin order can be dynamically encapsulated by the following inequality:

$$\frac{10}{9} \leq \langle \hat{\mathbf{S}} \rangle_t^2 + \langle \hat{\mathbf{Q}} \rangle_t^2 \leq \frac{4}{3}, \quad (4.5)$$

thereby demonstrating a clear relationship between the dynamic evolution of a system and the Casimir operators associated with its underlying symmetry group.

Furthermore, it was shown that the real effect of a driving term together with besides an external magnetic field preserves the typical evolution of the system under that same field, but also adds small oscillations or micromotion, making the interplay between these two types of oscillations constitute the true global dynamics of the system.

Finally, as demonstrated by the effects of the quadratic field in the two-particle system (Figs. 4.18 and 4.21), it was shown that not only can the action of an external magnetic field alter the properties of the system, but also the intensity, frequency, and manner in which it is applied can give rise to new phases, such as the interaction and Zeeman regimes, or phenomena like spin-mixing resonance. This underscores the essential role of magnetic fields in the study of spin-1 systems.

Chapter 5

CONCLUSIONS AND PERSPECTIVES

We have developed and implemented the extended Hilbert space method based on Floquet theory to investigate the time-evolution of quantum systems, applying it to simulate the spin-1 Bose-Hubbard model for both one-particle and two-particle cases in the superfluid regime. This approach has allowed us to characterize the different phases and regimes that emerge in these systems when external periodic magnetic fields are applied. Thus, to conclude this work, we provide a final summary of the essential information and significant results obtained throughout this extensive study. In addition, we present a list of perspectives for possible improvements to the method or study different approaches, as well as a deeper exploration of the model, which still contains much unexplored physics.

5.1 Conclusions

In summary, this work has demonstrated the feasibility of using Floquet theory and the extended Hilbert space method to study the dynamics of spin-1 lattice bosons in the presence of external periodic magnetic fields, employing the spin-1 Bose-Hubbard Hamiltonian as the foundational model. Moreover, we have successfully characterized the various phases present in both the single-particle and two-particle systems, revealing rich and significant physics within the field of spin-1 systems, exploring vastly their spin and quadrupolar behavior.

In Chapter 2, we presented a comprehensive modeling of spin-1 systems, specifically focusing on a system composed of spin-1 bosonic particles confined in a one-dimensional optical lattice. We began with the spinless Bose-Hubbard model, incorporated the spin-1 degree of freedom, and included both linear and quadratic Zeeman fields subject to a periodic driving that placed our system in a dynamical framework, specifically for one and two particles across the lattice, inevitably leading to the superfluid regime. Subsequently, we introduced the SU(3) bosonic representation as a new group for studying such systems, alongside the relevant bases, states, and observables needed to more fully characterize our system.

To effectively study this system, we employed a numerical technique based on Floquet theory

CHAPTER 5. CONCLUSIONS AND PERSPECTIVES

(Chapter 3). We first outlined Floquet's theorem, its implications, and its analogies with Bloch's theorem. The method utilized in our analysis was the extended Hilbert space method, which takes advantage of the periodic nature of our system to transfer the problem into Fourier harmonic space, where the evolution of the state could be more readily determined. We validated this method by analytically solving our one-particle system at two sites and comparing it with our numerical implementation, demonstrating a perfect match with no discernible errors.

From the dynamical analysis conducted in Chapter 4, three main conclusions can be drawn. First, through the analysis of spin and quadrupolar operators across various states and fields, we concluded that even in the absence of quadrupolar interaction terms in the Hamiltonian, or any interaction at all, spin-1 states inherently exhibit both spin and quadrupolar order. This was explicitly corroborated using Eq. (2.31), which revealed the competition between spin and quadrupolar order based on the expectation values of their observables, converging in their quadratic sum to the value of the quadratic Casimir operator of SU(3), 4/3. This relationship holds as long as the symmetry between the magnetic states of the system is preserved; otherwise, dynamically the equality may be replaced by the inequality $\frac{10}{9} \leq \langle \hat{\mathbf{S}} \rangle_t^2 + \langle \hat{\mathbf{Q}} \rangle_t^2 \leq \frac{4}{3}$, where the upper and lower bounds correspond to the eigenvalues of the quadratic and cubic Casimir operators of the SU(3) group, respectively. This finding underscores the intrinsic connection between spin-1 systems and the SU(3) symmetry group, which must be considered in both static and dynamic analyses, even in the absence of quadrupolar operators in the Hamiltonian or absence of particle-particle interactions.

Second, external magnetic fields, whether linear or quadratic are crucial for inducing different quantum phases in spin-1 systems. As demonstrated in the single-particle system, linear magnetic fields break time-invariance symmetry, leading to a preference for one magnetic state and the emergence of phenomena such as spin precession, making the system behave more like a spin-1/2 system. Conversely, quadratic fields preserved this symmetry, ensuring equal preference for magnetic states and causing the magnetic and quadrupolar orders to oscillate in time, maintaining their expected competition. This indicates that the influence of these fields can significantly alter the internal symmetries of the system and, consequently, its characteristics. In the two-particle system, the quadratic magnetic field is shown to divide the system's inherent phases (ferromagnetic and antiferromagnetic) into two crucial regimes: the interaction regime and the Zeeman regime. It was possible to either enhance or completely suppress internal interactions by adjusting the field strength, with specific field values marking the point where the field and interactions enter into phase, leading to the phenomenon of spin-mixing resonance ($Q'_0 \approx 1.61U_2$ for the antiferromagnetic phase and $Q'_0 \approx |4.96U_2|$ for the ferromagnetic phase). Thus, magnetic fields in spin systems

substantially enrich the physics, especially in dynamic systems like in our case.

Finally, it can be concluded that Floquet theory and specifically the extended Hilbert space approach provide an exceptionally powerful tool for addressing dynamical systems in a practical and straightforward manner. The inclusion of a periodic driving term allowed not only the successful reproduction of system dynamics but also offered diverse insights into how the Hamiltonian term to which the driving is coupled affects the system. The method's versatility, whether in examining the system without the term (weak-driving regime and linear driving), with the term in a constant manner (weak-driving regime and quadratic driving), or with the term oscillating the system (strong-driving regime), positions it as a strong technique that can be applied to any quantum system in a practical way. Despite extending the dimension of the Hilbert space, which can be challenging depending on the degrees of freedom of the system, the method converges rapidly if compensated by techniques such as effective bases in the case of single particles or few sites in the case of two particles, thereby also demonstrating computational efficiency. Moreover, further numerical enhancements can always be implemented in order to extend the length of the system.

Given these conclusions, it is evident that the extended Hilbert space method, as provided by Floquet's theorem, is an incredibly powerful tool for studying any type of dynamical system. It opens up the possibility of exploring different quantum systems dynamically, including those that are not typically studied due to their complexity. In this work, we effectively applied it to study the dynamics of one and two spin-1 bosons loaded into an optical lattice in the presence of external magnetic fields using the spin-1 Bose-Hubbard Hamiltonian as a foundation. However, as mentioned, this method can be applied to any quantum system and even combined with other analytical techniques or approximations. This work also serves as a guide for implementing Floquet's theorem in other systems or for continuing research in the field of dynamical spin systems, where much remains to be discovered, especially for my colleagues in the Theoretical Solid State Physics research group in our Physics Department, contributing to high-level research at Universidad del Valle.

5.2 Perspectives

Finally, with the numerical construction of the extended Hilbert space method provided by Floquet theory, we present a list of potential enhancements for this approach and suggest directions for investigating the unexplored physics in the spin-1 Bose-Hubbard Model:

CHAPTER 5. CONCLUSIONS AND PERSPECTIVES

For the Floquet Theory tool:

- Implement and study different types of periodic driving that can be coupled, such as square, triangular, sawtooth (ramp), pulsed, or rectified signal-type driving, among other periodicities widely used in experimental contexts.
- Use and implement other numerical approaches based on Floquet's theory, such as the Trotter decomposition of the time evolution operator, $\hat{U}(t_0 + T, t_0)$.

For the unexplored physics in the spin-1 Bose-Hubbard model:

- Develop an algorithm to generate effective state bases in the system, which would significantly reduce computational costs as the number of sites increases, enabling the study of the system with any number of particles.
- Explore further the properties and implications of Eq. (4.4) concerning the superfluidity of the system.
- Conduct a study involving three particles, including three-body interactions.
- Perform spectral analysis of the system using the quasienergies provided by Floquet theory and analyze what type of information can be extracted, for instance, related to the energies of the non-dynamic system.
- Investigate a two-dimensional or three-dimensional lattice, which could allow for phenomena such as condensation within the system.
- Analyze the system under approximations such as mean-field theory or deep lattice Hamiltonian.
- Study variations of the system by coupling the driving to different terms of the Hamiltonian, such as the interaction term.

Appendix A

SPIN 1 CALCULATIONS

With the addition of the spin-1 degree of freedom, new physics emerges. In this appendix, we detail the on-site interaction potential of the Bose-Hubbard Hamiltonian for spin-1 particles. Initially, we demonstrate how to convert the interaction potential from projector operators to spin operators, considering the addition of angular momenta and the spin-1 characteristics. We then proceed to express the whole Hamiltonian in second quantization and outline the effective potential used to describe many-particle systems as shown in Eq. (2.14). Then, we describe how to employ the Schwinger bosons formalism to represent the entire Hamiltonian in terms of creation and annihilation operators, facilitating the use of a common basis for matrix representation. Finally, some aspects of SU(3) group is shown, which connects the symmetry group of the system and the physical observables.

A.1 Interaction Potential

We define the spin operators for a two-particle interacting system as $\{\hat{\mathbf{S}}_1, \hat{\mathbf{S}}_2\}$, where the subscript indicates the particle to which the operator corresponds. These operators form a new operator for the coupled system:

$$\hat{\mathbf{F}} = \hat{\mathbf{S}}_1 + \hat{\mathbf{S}}_2, \quad (\text{A.1})$$

this total spin operator enables us to describe the spin-1 system in terms of a new complete set of commuting observables (CSCO), the coupled basis is given by the following set of operators:

$$\left\{ \hat{\mathbf{S}}_1^2, \hat{\mathbf{S}}_2^2, \hat{\mathbf{F}}^2, \hat{F}^z \right\}, \quad (\text{A.2})$$

where $\hat{\mathbf{S}}_i^2$ are the squares of the spin operators for each individual particle, $\hat{\mathbf{F}}^2$ is the square of the total spin operator for the coupled system, and \hat{F}^z is its associated magnetic projection on the z-axis. This set of operators defines the set of eigenstates $\{|s_1, s_2, F, M\rangle\}$, where $|s_1 - s_2| \leq F \leq s_1 + s_2$ and $-F \leq M \leq F$.

The typical uncoupled basis is defined by the set of operators $\left\{ \hat{\mathbf{S}}_1^2, \hat{\mathbf{S}}_2^2, \hat{S}_1^z, \hat{S}_2^z \right\}$, with its set of

APPENDIX A. SPIN 1 CALCULATIONS

eigenstates $\{|s_1, s_2, \sigma_1, \sigma_2\rangle\}$, where the relationship between these two bases is given by the well-known Clebsch-Gordan coefficients. Since the total spin F is conserved in a binary collision, the interaction Hamiltonian can be divided according to the spin channel F as:

$$\hat{V}_{\text{int}} = \sum_F g_F \hat{P}_F \delta(x - x'), \quad \text{with } g_F = \frac{4\pi\hbar^2 a_F}{m}. \quad (\text{A.3})$$

The scattering processes are independent in each channel, and with the bosonic nature of the particles, the available channels are $F = \{0, 2\}$. Therefore, the interaction can now be expressed as follows:

$$\hat{V}_{\text{int}} = \left(g_0 \hat{P}_0 + g_2 \hat{P}_2 \right) \delta(x - x'), \quad (\text{A.4})$$

For convenience, we aim to rewrite the effective potential in terms of the spin operators, so using Eq. (A.1), we write:

$$\begin{aligned} \hat{F}^2 &= \left(\hat{\mathbf{S}}_1 + \hat{\mathbf{S}}_2 \right)^2 = \hat{\mathbf{S}}_1^2 + 2\hat{\mathbf{S}}_1 \cdot \hat{\mathbf{S}}_2 + \hat{\mathbf{S}}_2^2, \\ \hat{\mathbf{S}}_1 \cdot \hat{\mathbf{S}}_2 &= \frac{1}{2} \left(\hat{F}^2 - \hat{\mathbf{S}}_1^2 - \hat{\mathbf{S}}_2^2 \right), \end{aligned} \quad (\text{A.5})$$

due to the linear independence, we use the interaction channels as a basis for the space of linear operators acting on the two particles, yielding the decomposition:

$$\hat{\mathbf{S}}_1 \cdot \hat{\mathbf{S}}_2 = \lambda_0 \hat{P}_0 + \lambda_2 \hat{P}_2, \quad (\text{A.6})$$

Applying $\hat{\mathbf{S}}_1 \cdot \hat{\mathbf{S}}_2$ to the elements of the coupled basis according to the identity in Eq. (A.5), we obtain:

$$\hat{\mathbf{S}}_1 \cdot \hat{\mathbf{S}}_2 |F, M\rangle = \frac{1}{2} (F(F+1) - s_1(s_1+1) - s_2(s_2+1)) |F, M\rangle, \quad (\text{A.7})$$

since $s_1 = s_2 = 1$ implies $\lambda_0 = -2$ and $\lambda_2 = 1$. Additionally, the identity operator of the bosonic Hilbert space can be expanded as $\hat{I} = \hat{P}_0 + \hat{P}_2$, giving us the following system of equations:

$$\hat{I} = \hat{P}_0 + \hat{P}_2, \quad \hat{\mathbf{S}}_1 \cdot \hat{\mathbf{S}}_2 = -2\hat{P}_0 + \hat{P}_2, \quad (\text{A.8})$$

then, solving the system of equations for the projectors, we get:

$$\hat{P}_0 = \frac{\hat{I} - \hat{\mathbf{S}}_1 \cdot \hat{\mathbf{S}}_2}{3}, \quad \hat{P}_2 = \frac{2\hat{I} + \hat{\mathbf{S}}_1 \cdot \hat{\mathbf{S}}_2}{3}, \quad (\text{A.9})$$

finally allowing us to write the interaction potential as:

$$\hat{V}_{\text{int}} = \left(c_0 + c_2 \hat{\mathbf{S}}_1 \cdot \hat{\mathbf{S}}_2 \right) \delta(x - x') \quad \text{with: } c_0 = \frac{g_0 + 2g_2}{3} \quad \text{and} \quad c_2 = \frac{g_2 - g_0}{3}. \quad (\text{A.10})$$

A.2 Second quantization

First led us to define the new fields operators $\hat{\Psi}_\alpha(x)$ which includes the spin 1 degree of freedom

$$\hat{\Psi}_\alpha(x) = \sum_i W_i(x) \hat{b}_{i,\alpha}, \quad (\text{A.11})$$

where $W_i(x)$ are the wannier function of the lowest Bloch band, which is a strongly localized wave function in the i -th site of the lattice, and satisfy the common orthogonal relation, $\alpha = -1, 0, 1$ are the spin projections and now this operators satisfies the following commutation relations

$$\begin{aligned} \left[\hat{b}_{i,\alpha}^\dagger, \hat{b}_{j,\beta}^\dagger \right] &= \left[\hat{b}_{i,\alpha} \hat{b}_{j,\beta} \right] = 0, \quad \left[\hat{b}_{i,\alpha} \hat{b}_{j,\beta}^\dagger \right] = \delta_{\alpha\beta} \delta_{ij}, \\ \left[\hat{\Psi}_\alpha^\dagger(x), \hat{\Psi}_\beta^\dagger(x') \right] &= \left[\hat{\Psi}_\alpha(x), \hat{\Psi}_\beta(x') \right] = 0, \quad \left[\hat{\Psi}_\alpha(x), \hat{\Psi}_\beta^\dagger(x') \right] = \delta_{\alpha\beta} \delta(x - x'). \end{aligned}$$

In order to derive the model we start from the Hamiltonian for one particle which reads,

$$\hat{H} = \frac{\hat{p}^2}{2m} + \hat{V}_{\text{lat}} + \hat{V}_{\text{int}} + \hat{H}_Z, \quad (\text{A.12})$$

in the second quantization formalism with the addition of spin 1 degree of freedom the hopping term would be

$$\begin{aligned} \hat{H}_J &= \sum_{\alpha,\beta} \int dx \hat{\Psi}_\alpha^\dagger(x) \langle \alpha | \left(-\frac{\hbar^2 \nabla^2}{2m} + V_{\text{lat}}(x) \right) | \beta \rangle \hat{\Psi}_\beta(x), \\ &= \sum_{i,j} \sum_{\alpha,\beta} \int dx W_i^*(x) \left(-\frac{\hbar^2 \nabla^2}{2m} + V_{\text{lat}}(x) \right) W_j(x) \langle \alpha | \beta \rangle \hat{b}_{i,\alpha}^\dagger \hat{b}_{j,\beta}, \\ &= -J \sum_{i,\sigma} \left(\hat{b}_{i+1,\sigma}^\dagger \hat{b}_{i,\sigma} + \hat{b}_{i,\sigma}^\dagger \hat{b}_{i+1,\sigma} \right), \end{aligned} \quad (\text{A.13})$$

for the Zeeman fields we have

$$\hat{H}_Z = \sum_{\alpha,\beta} \int dx \hat{\Psi}_\alpha^\dagger(x) \langle \alpha | \left(D_0 \hat{S}^z + Q_0 \left(\hat{S}^z \right)^2 \right) | \beta \rangle \hat{\Psi}_\beta(x),$$

APPENDIX A. SPIN 1 CALCULATIONS

$$\begin{aligned}
&= \sum_{i,j,\alpha,\beta} \int dx W_i^*(x) \hat{b}_{i,\alpha}^\dagger \left(D_0 \langle \alpha | \hat{S}^z | \beta \rangle + Q_0 \langle \alpha | (\hat{S}^z)^2 | \beta \rangle \right) \hat{b}_{j,\beta} W_j(x), \\
&= D_0 \sum_i \sum_{\alpha,\beta} \hat{b}_{i,\alpha}^\dagger [\hat{S}^z]_{\alpha\beta} \hat{b}_{i,\beta} + Q_0 \sum_i \sum_{\alpha,\beta} \hat{b}_{i,\alpha}^\dagger [(\hat{S}^z)^2]_{\alpha\beta} \hat{b}_{i,\beta}, \\
&= D_0 \sum_{i,\sigma} \sigma \hat{n}_{i,\sigma} + Q_0 \sum_{i,\sigma} \sigma^2 \hat{n}_{i,\sigma},
\end{aligned} \tag{A.14}$$

and for the interaction potential defined in Eq. (A.10), we get,

$$\begin{aligned}
\hat{V}_{\text{int}} &= \frac{1}{2} \sum_{\alpha,\gamma,\beta,\sigma} \int dx dx' \hat{\Psi}_\alpha^\dagger(x) \hat{\Psi}_\gamma^\dagger(x') \langle \alpha, \gamma | \hat{V}_{\text{int}} | \beta, \sigma \rangle \hat{\Psi}_\beta(x') \hat{\Psi}_\sigma(x), \\
&= \sum_{\alpha,\beta,\gamma,\sigma} \int dx \left(\frac{c_0}{2} \hat{\Psi}_\alpha^\dagger(x) \hat{\Psi}_\beta^\dagger(x) \hat{\Psi}_\beta(x) \hat{\Psi}_\alpha(x) + \frac{c_2}{2} \hat{\Psi}_\alpha^\dagger(x) \hat{\Psi}_\gamma^\dagger(x) [\hat{\mathbf{S}}]_{\alpha\beta} \cdot [\hat{\mathbf{S}}]_{\gamma\sigma} \hat{\Psi}_\gamma(x) \hat{\Psi}_\sigma(x) \right), \\
&= \frac{U_0}{2} \sum_{i,\alpha,\beta} \hat{b}_{i,\alpha}^\dagger \hat{b}_{i,\beta}^\dagger \hat{b}_{i,\beta} \hat{b}_{i,\alpha} + \frac{U_2}{2} \sum_{i,\alpha,\beta,\gamma,\sigma,\nu} \hat{b}_{i,\alpha}^\dagger \hat{b}_{i,\gamma}^\dagger [\hat{S}^\nu]_{\alpha\beta} [\hat{S}^\nu]_{\gamma\sigma} \hat{b}_{i,\sigma} \hat{b}_{i,\beta}, \\
&= \sum_{i,\alpha,\beta} \hat{b}_{i,\alpha}^\dagger (\hat{b}_{i,\alpha} \hat{b}_{i,\beta}^\dagger - \delta_{\alpha\beta}) \hat{b}_{i,\beta} + \frac{U_2}{2} \sum_{i,\nu} \left\{ \left(\hat{F}_i^\nu \right)^2 - \sum_{\alpha,\beta,\sigma} \hat{b}_{i,\alpha}^\dagger [\hat{S}^\nu]_{\alpha\beta} [\hat{S}^\nu]_{\beta\sigma} \hat{b}_{i,\sigma} \right\}, \\
&= \frac{U_0}{2} \sum_{i,\sigma} \hat{n}_{i,\sigma} (\hat{n}_{i,\sigma} - 1) + \frac{U_2}{2} \sum_i \left(\hat{\mathbf{F}}_i^2 - 2 \sum_\sigma \hat{n}_{i,\sigma} \right),
\end{aligned} \tag{A.15}$$

where

$$\begin{aligned}
J &= \int dx W_i^*(x) \left(-\frac{\hbar^2 \nabla^2}{2m} + V_{\text{lat}}(x) \right) W_j(x), \\
U_0 &= c_0 \int dx |W(x)|^4 = \frac{g_0 + 2g_2}{3} \int dx |W(x)|^4, \\
U_2 &= c_2 \int dx |W(x)|^4 = \frac{g_2 - g_0}{3} \int dx |W(x)|^4, \\
\hat{\mathbf{F}}_i &= \left(\hat{F}_i^x, \hat{F}_i^y, \hat{F}_i^z \right), \quad \hat{F}_i^\nu = \sum_{\sigma,\sigma'} \hat{b}_{i,\sigma}^\dagger [\hat{S}^\nu]_{\sigma\sigma'} \hat{b}_{i,\sigma'}.
\end{aligned}$$

So finally, the Bose-Hubbard Hamiltonian for spin-1 particles, in second quantization and in the grand canonical ensemble, is given by,

$$\hat{H} = -J \sum_{i,\sigma} \left(\hat{b}_{i+1,\sigma}^\dagger \hat{b}_{i,\sigma} + \text{h.c.} \right) + \frac{U_0}{2} \sum_{i,\sigma} \hat{n}_{i,\sigma} (\hat{n}_{i,\sigma} - 1) + \frac{U_2}{2} \sum_i \hat{\mathbf{F}}_i^2 - (\mu + U_2) \sum_{i,\sigma} \hat{n}_{i,\sigma} + \hat{H}_Z. \tag{A.16}$$

A.3 Schwinger Bosons (SB)

Since we are working with spin-1 bosons, we can adopt an SU(3) bosonic representation where the generators of the Hilbert space are based on creation and annihilation operators. A standard construction of the SU(3) generators, utilizing these operators, involves defining three independent pairs of annihilation and creation operators (often referred to as three “flavors”) $(\hat{b}_{i,\sigma}, \hat{b}_{i,\sigma}^\dagger)$, where i denotes the lattice sites and σ represents the three magnetic projections: $\{1, -1, 0\}$ [64]. Specifically, $\hat{b}_{i,\sigma}^\dagger |\emptyset\rangle = |\sigma\rangle_i$ creates a particle with magnetic projection σ at site i . The generators $\hat{\Gamma}_i^{\sigma,\sigma'} = \hat{b}_{i,\sigma}^\dagger \hat{b}_{i,\sigma'}$ form the SU(3) Lie algebra and fulfill the SU(N) commutation relations [91].

$$[\hat{\Gamma}_i^{\sigma,\sigma'}, \hat{\Gamma}_j^{\alpha,\alpha'}] = \delta_{ij} \left(\delta_{\sigma'\alpha} \hat{\Gamma}_j^{\sigma,\alpha'} - \delta_{\sigma\alpha} \hat{\Gamma}_i^{\sigma',\alpha'} \right). \quad (\text{A.17})$$

The identity and the $N^2 - 1$ generators of SU(N) form a basis for the $(N + 1) \times (N + 1)$ matrices acting on the Hilbert space associated with the site i . This includes the vacuum state, which adds a row and a column of zeros to the matrix, a crucial aspect for a complete description of the system. Therefore, any local operator can be expressed as a linear combination of these generators. Thus, for a local operator \hat{O}_i , its representation in terms of Schwinger bosons can be expressed as follows:

$$\hat{O}_i = \sum_{\sigma,\sigma'} \hat{b}_{i,\sigma}^\dagger [\hat{O}]_{\sigma,\sigma'} \hat{b}_{i,\sigma'}, \quad (\text{A.18})$$

where $[\hat{O}]_{\sigma,\sigma'}$ corresponds to the matrix elements (in the magnetic basis) of the local operator \hat{O}_i . Consequently, we can express any spin operator in the Schwinger Boson (SB) representation as functions of the \hat{b} operators, as detailed below:

$$\begin{aligned} \hat{S}_i^+ &= \sqrt{2} \left(\hat{b}_{i,0}^\dagger \hat{b}_{i,-1} + \hat{b}_{i,1}^\dagger \hat{b}_{i,0} \right), & \hat{S}_i^- &= \sqrt{2} \left(\hat{b}_{i,-1}^\dagger \hat{b}_{i,0} + \hat{b}_{i,0}^\dagger \hat{b}_{i,1} \right), \\ \hat{S}_i^z &= \hat{b}_{i,1}^\dagger \hat{b}_{i,1} - \hat{b}_{i,-1}^\dagger \hat{b}_{i,-1}, \end{aligned} \quad (\text{A.19})$$

in such a way that, utilizing the identity $\hat{\mathbf{F}}_i^2 = \frac{1}{2}(\hat{S}_i^- \hat{S}_i^+ + \hat{S}_i^+ \hat{S}_i^-) + (\hat{S}_i^z)^2$, we can reformulate the total spin operator involved in the interaction in terms of Schwinger Bosons.

$$\begin{aligned} \hat{\mathbf{F}}_i^2 &= (\hat{n}_{i,1} - \hat{n}_{i,-1})^2 + \hat{n}_{i,1} + 2\hat{n}_{i,0} + \hat{n}_{i,-1} + 2(\hat{n}_{i,1}\hat{n}_{i,0} + \hat{n}_{i,0}\hat{n}_{i,-1}) \\ &\quad + 2 \left(\hat{b}_{i,1}^\dagger \hat{b}_{i,-1}^\dagger \hat{b}_{i,0} \hat{b}_{i,0} + \hat{b}_{i,0}^\dagger \hat{b}_{i,0}^\dagger \hat{b}_{i,1} \hat{b}_{i,-1} \right), \end{aligned} \quad (\text{A.20})$$

APPENDIX A. SPIN 1 CALCULATIONS

And in the same way to the operator $\hat{F}_i^x = \frac{1}{2}(\hat{S}_i^+ + \hat{S}_i^-)$, for its measurement as an observable of the total transverse magnetization at site i ,

$$\hat{F}_i^x = \frac{1}{\sqrt{2}} (\hat{b}_{i,0}^\dagger \hat{b}_{i,-1} + \hat{b}_{i,0}^\dagger \hat{b}_{i,1} + \text{h. c.}) . \quad (\text{A.21})$$

It is important to remark that the spin operators keep the usual spin commutation relations, as a consequence of the bosonic commutation relations.

A.4 SU(3) Group

The group SU(3) is an 8-dimensional Lie group consisting of all 3×3 unitary matrices with determinant 1 [92]. Our generators of the SU(3) are given in the cartesian $\{|x\rangle, |y\rangle, |z\rangle\}$ basis by:

$$\begin{aligned} \Lambda^1 &= \begin{pmatrix} 0 & 0 & 0 \\ 0 & 0 & -i \\ 0 & i & 0 \end{pmatrix}, \quad \Lambda^2 = \begin{pmatrix} 0 & 0 & -i \\ 0 & 0 & 0 \\ i & 0 & 0 \end{pmatrix}, \quad \Lambda^3 = \begin{pmatrix} 0 & -i & 0 \\ i & 0 & 0 \\ 0 & 0 & 0 \end{pmatrix}, \\ \Lambda^4 &= \begin{pmatrix} 0 & 0 & 0 \\ 0 & 0 & -1 \\ 0 & -1 & 0 \end{pmatrix}, \quad \Lambda^5 = \begin{pmatrix} 0 & 0 & -1 \\ 0 & 0 & 0 \\ -1 & 0 & 0 \end{pmatrix}, \quad \Lambda^6 = \begin{pmatrix} 0 & -1 & 0 \\ -1 & 0 & 0 \\ 0 & 0 & 0 \end{pmatrix}, \\ \Lambda^7 &= \begin{pmatrix} 1 & 0 & 0 \\ 0 & -1 & 0 \\ 0 & 0 & 0 \end{pmatrix}, \quad \Lambda^8 = \frac{1}{\sqrt{3}} \begin{pmatrix} 1 & 0 & 0 \\ 0 & 1 & 0 \\ 0 & 0 & -2 \end{pmatrix}, \end{aligned} \quad (\text{A.22})$$

which are related, simply by a change in the order and signs, with the typical generators of SU(3), the Gell-Mann matrices $(\hat{\lambda}^a)$ [69]. Then, with the change of basis of the Eq. (2.38) in the magnetic basis $\{|1\rangle, |-1\rangle, |0\rangle\}$ are given by:

$$\begin{aligned} \Lambda^1 &= \frac{1}{\sqrt{2}} \begin{pmatrix} 0 & 0 & 1 \\ 0 & 0 & 1 \\ 1 & 1 & 0 \end{pmatrix}, \quad \Lambda^2 = \frac{1}{\sqrt{2}} \begin{pmatrix} 0 & 0 & -i \\ 0 & 0 & i \\ i & -i & 0 \end{pmatrix}, \quad \Lambda^3 = \begin{pmatrix} 1 & 0 & 0 \\ 0 & -1 & 0 \\ 0 & 0 & 0 \end{pmatrix}, \\ \Lambda^4 &= \frac{1}{\sqrt{2}} \begin{pmatrix} 0 & 0 & -i \\ 0 & 0 & -i \\ i & i & 0 \end{pmatrix}, \quad \Lambda^5 = \frac{1}{\sqrt{2}} \begin{pmatrix} 0 & 0 & 1 \\ 0 & 0 & -1 \\ 1 & -1 & 0 \end{pmatrix}, \quad \Lambda^6 = \frac{1}{\sqrt{2}} \begin{pmatrix} 0 & -i & 0 \\ i & 0 & 0 \\ 0 & 0 & 0 \end{pmatrix}, \end{aligned} \quad (\text{A.23})$$

$$\Lambda^7 = \begin{pmatrix} 0 & 1 & 0 \\ 1 & 0 & 0 \\ 0 & 0 & 0 \end{pmatrix}, \quad \Lambda^8 = \frac{1}{\sqrt{3}} \begin{pmatrix} 1 & 0 & 0 \\ 0 & 1 & 0 \\ 0 & 0 & -2 \end{pmatrix},$$

the above matrices, being Hermitian and traceless, satisfy the following SU(3) algebra:

$$[\hat{\Lambda}^a, \hat{\Lambda}^b] = 2i \sum_c f^{abc} \hat{\Lambda}^c, \quad (\text{A.24})$$

where f^{abc} are structure constants having the following numerical values:

$$\begin{aligned} f^{184} = f^{258} &= \frac{\sqrt{3}}{2}, \\ f^{123} = f^{147} = f^{165} = f^{354} = f^{246} &= f^{257} = \frac{1}{2}, \\ f^{376} &= 1. \end{aligned} \quad (\text{A.25})$$

A.4.0 The Casimir Operators of SU(3)

The *Casimir operator* or *Casimir element* \hat{C} is defined as the operator that commutes with every generator $\hat{\Lambda}^a$ of the group [70], namely

$$[\hat{C}, \hat{\Lambda}^a] = 0. \quad (\text{A.26})$$

The importance of this operator lies in the fact that, since it commutes with all the generators of the group, its form is diagonal regardless of the chosen basis. Additionally, it satisfies a crucial property: regardless of the representation, it is always a multiple of the identity, making its eigenvalues a natural way to label the different representations.

One way to understand this is by examining the SU(2) Casimir operator, which is expressed as a quadratic operator of the generators $\hat{J}^2 = \hat{J}_x^2 + \hat{J}_y^2 + \hat{J}_z^2$ in a general way. Together with the magnetic projection on the z -axis \hat{J}^z , they form the typical magnetic basis used to describe angular momentum in quantum mechanics [77]. This basis is denoted as $|j, m\rangle$ with the respective eigenvalue equations $\hat{J}^2|j, m\rangle = \hbar j(j+1)|j, m\rangle$ and $\hat{J}^z|j, m\rangle = \hbar m|j, m\rangle$. As we see, the eigenvalues of the Casimir operator provide a natural way to label the different representations of SU(2), which in this case physically represent different spin values of the particles ($j = 1/2, 1, 3/2, \dots$). Therefore,

APPENDIX A. SPIN 1 CALCULATIONS

the Casimir operator takes the form $\hat{J}^2_{j=1/2} = \frac{3}{4}\hat{I}$, $\hat{J}^2_{j=1} = 2\hat{I}$..., which as we can see is always a multiple of the identity.

Now, the SU(3) case is quite similar. The Casimir operator is defined in the same way as a quadratic operator of the generators, namely

$$\hat{C} = \sum_{a=1}^8 \hat{\Lambda}^a \hat{\Lambda}^a = \hat{\mathbf{S}}^2 + \hat{\mathbf{Q}}^2, \quad (\text{A.27})$$

and just as in the case of SU(2), its eigenvalues serve to label the different representations. In fact, one can prove that given the typical magnetic basis ($\{\hat{\mathbf{S}}^2, \hat{S}^z\} \rightarrow |S, \sigma\rangle$), its eigenvalue equation is given by

$$\hat{C}|S, \sigma\rangle = (\hat{\mathbf{S}}^2 + \hat{\mathbf{Q}}^2)|S, \sigma\rangle = \frac{4}{3}S^2(S+1)^2|S, \sigma\rangle. \quad (\text{A.28})$$

However, in our case, the important representation is the fundamental or three-dimensional representation ($S = 1$), which takes the form, $\hat{C}^2 = \frac{16}{3}\hat{I}$.

Typically, it is common to express the generators with a factor of $1/2$, i.e., $\hat{T}^a = \frac{1}{2}\hat{\Lambda}^a$, such that the quadratic Casimir operator is expressed in the most common way as

$$\hat{C}^2 = \frac{1}{4} \sum_{a=1}^8 \hat{\Lambda}^a \hat{\Lambda}^a = \sum_{a=1}^8 \hat{T}^a \hat{T}^a = \frac{4}{3}\hat{I}, \quad (\text{A.29})$$

thereby connecting the SU(3) quadratic Casimir operator with the expectation values of the total spin and quadrupole contributions, Eq. (2.31).

Furthermore, it can be shown that in the case of SU(3), there is no unique Casimir operator. Indeed, for the group SU(N), there are $N - 1$ Casimir operators, each expressed in quadratic, cubic, and higher-order forms [93]. Therefore, in the case of SU(3), the cubic Casimir operator is given by

$$\hat{C}^3 = \sum_{a,b,c} d_{abc} \hat{T}^a \hat{T}^b \hat{T}^c, \quad (\text{A.30})$$

where d_{abc} are structure constants [92]. Then, in its fundamental representation, the cubic Casimir operator takes the form

$$\hat{C}^3 = \frac{10}{9}\hat{I}, \quad (\text{A.31})$$

also connecting it with some results seen in this study (see appendix D and Chapter 4).

Appendix B

SUPPLEMENTARY MATERIAL ON FLOQUET THEORY

Since Floquet theory encompasses many analytical and numerical approaches, this appendix provides supplementary material to delve deeper into the formalism used. First, the most common proof of Floquet's theorem is provided, emphasizing the properties of the time evolution operator. Then, other types of numerical solutions to Floquet's problem are covered. Finally, the different concepts and definitions established in Floquet's formalism are summarized, highlighting its analogies with Bloch's theorem.

B.1 Proof of Floquet theorem

As mentioned in chapter 3 there are several ways to express Floquet's theorem, for its demonstration it is easier to state it in such a way that it focuses on the properties of the time evolution operator, which due to the periodicity of the Hamiltonian satisfies:

$$\hat{U}(t + nT, t_0) = \hat{U}(t, t_0) \left[\hat{U}(t_0 + T, t_0) \right]^n. \quad (\text{B.1})$$

This proof is a simplified form of the typical proof basing in the time evolution operator, emphasizing in the more relevant points [76].

Then, in principle, the whole dynamics is captured by the unitary time-evolution operator $\hat{U}(t, t_0)$, which evolve the state in the common way

$$|\psi(t)\rangle = \hat{U}(t, t_0)|\psi(t_0)\rangle, \quad \text{with} \quad \hat{U}(t, t_0) = \mathcal{T} \exp \left\{ -\frac{i}{\hbar} \int_{t_0}^t \hat{H}(t') dt' \right\}, \quad (\text{B.2})$$

where \mathcal{T} denotes the time-ordering. Now, evidently this time evolution operator satisfy the following property

$$\hat{U}(t_2, t_0) = \hat{U}(t_2, t_1)\hat{U}(t_1, t_0), \quad (\text{B.3})$$

APPENDIX B. SUPPLEMENTARY MATERIAL ON FLOQUET THEORY

with this in mind consider the time-evolution operator from initial time t_0 to some final time $t + T$

$$\begin{aligned}\hat{U}(t+T, t_0) &= \hat{U}(t+T, t_0+T)\hat{U}(t_0+T, t_0), \\ &= \hat{U}(t, t_0)\hat{U}(t_0+T, t_0).\end{aligned}$$

We knowing that any time-evolution operator $\hat{U}(t_2, t_1)$ must be unitary (i.e. $\hat{U}^\dagger\hat{U} = \mathbb{1}$), therefore we are able to write the second part of our time-evolution operator as

$$\hat{U}(t_0+T, t_0) = e^{-\frac{i}{\hbar}\hat{H}_F T}, \quad (\text{B.4})$$

where \hat{H}_F is called the “*Floquet Hamiltonian*” and its exponential is the “*Floquet Operator*”, the “*Floquet Propagator*” or the “*slow-motion operator*”, and as \hat{H}_F is a hermitian operator ($\hat{H}_F^\dagger = \hat{H}_F$) using this, we can rewrite the time-evolution operator of the whole system as

$$\begin{aligned}\hat{U}(t, t_0) &= \underbrace{\hat{U}(t, t_0)e^{\frac{i}{\hbar}\hat{H}_F \times (t-t_0)}}_{\hat{P}(t, t_0)} e^{-\frac{i}{\hbar}\hat{H}_F \times (t-t_0)}, \\ \hat{U}(t, t_0) &= \hat{P}(t, t_0)e^{-\frac{i}{\hbar}\hat{H}_F \times (t-t_0)},\end{aligned}$$

and now again due the unitarity $\hat{P}(t, t_0)$ must be

$$\hat{P}(t, t_0) = \hat{U}(t, t_0)e^{\frac{i}{\hbar}\hat{H}_F \times (t-t_0)} = e^{-i\hat{K}_F(t)}, \quad (\text{B.5})$$

where $\hat{K}_F(t)$ is called the “*stroboscopic kick operator*” and its exponential the “*fast-motion operator*”, that obeys $e^{-i\hat{K}_F(t+T)} = e^{-i\hat{K}_F(t)}$

This means that the kick operator describes the motion within one period T but does change from one period to the next(it just depends on the global choice of starting time t_0). This allows us to directly write down Floquet’s theorem for periodically modulated hamiltonians, which states that given a Hamiltonian that satisfies $\hat{H}(t) = \hat{H}(t+T)$ then its time-evolution operator is given by

$$\hat{U}(t, t_0) = e^{-i\hat{K}_F(t)}e^{-\frac{i}{\hbar}\hat{H}_F \times (t-t_0)}, \quad (\text{B.6})$$

where

$$e^{-i\hat{K}_F(t)} : \text{Fast-motion operator}, \quad e^{-\frac{i}{\hbar}\hat{H}_F \times (t-t_0)} : \text{Slow-motion operator}.$$

APPENDIX B. SUPPLEMENTARY MATERIAL ON FLOQUET THEORY

This result is the mathematical way of separating the slow dynamics (governed by \hat{H}_F) from the fast-motion during one period T (governed by $e^{-i\hat{K}_F(t)}$), as illustrated in the Figs B.1 and B.2.

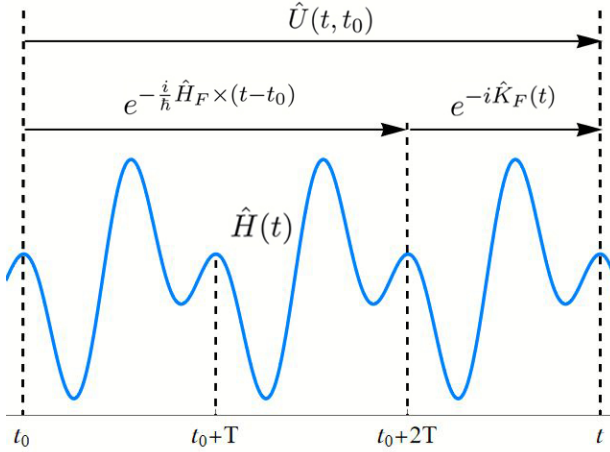


Figure B.1: Floquet's theorem illustrated. The slow dynamics (from one period T to the next) is captured by Floquet Hamiltonian \hat{H}_F , whereas the fast “micromotion” within a period is governed by the fast motion operator $e^{-i\hat{K}_F(t)}$.

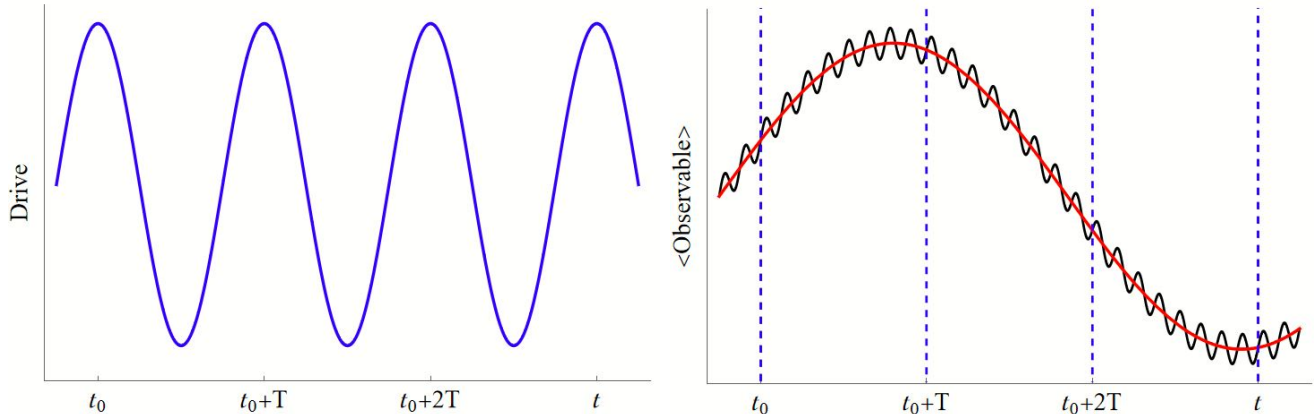


Figure B.2: The action of a periodic drive (left panel) on the time-evolution of a quantum system. The slow dynamics of an observable (red line) is captured by the Floquet Hamiltonian \hat{H}_F whereas the exact dynamics (black line) is composed of fast dynamics (micromotion) and slow dynamics. The micromotion is described by the kick operators $e^{-i\hat{K}_F(t)}$ and vanishes at stroboscopic times $t_0, t_0 + T$, etc.

Now, the Floquet operator, being unitary can be in principle diagonalised, it means that a complete

APPENDIX B. SUPPLEMENTARY MATERIAL ON FLOQUET THEORY

set of eigenstates exist, let us indicate them by $|u_n(t_0)\rangle$, such that

$$e^{-\frac{i}{\hbar}\hat{H}_F \times (t-t_0)}|u_n(t_0)\rangle = e^{-\frac{i}{\hbar}\varepsilon_n \times (t-t_0)}|u_n(t_0)\rangle, \quad (\text{B.7})$$

where, these eigenvalues $e^{-\frac{i}{\hbar}\varepsilon_n \times (t-t_0)}$ are called the “*Floquet multipliers*”. Remember ε_n is a real parameter called quasienergy being unique up to multiples of $\hbar\omega$, $\omega = \frac{2\pi}{T}$. Taking the multivaluedness of the energies ε_n into account, we can also directly get the eigenstates and eigenvalues via

$$\hat{H}_F|u_n(t_0)\rangle = \varepsilon_n|u_n(t_0)\rangle, \quad (\text{B.8})$$

where the eigenstates $|u_n(t_0)\rangle$ are called the “*Floquet Modes*”. Now we expand an arbitrary initial state $|\psi(t_0)\rangle$ in eigenbasis of Floquet hamiltonian

$$\begin{aligned} |\psi(t_0)\rangle &= \sum_n |u_n(t_0)\rangle \underbrace{\langle u_n(t_0)|\psi(t_0)\rangle}_{\equiv c_n}, \\ &= \sum_n c_n |u_n(t_0)\rangle. \end{aligned}$$

Then, the state at later times is expressed as

$$\begin{aligned} |\psi(t)\rangle &= \hat{U}(t, t_0)|\psi(t_0)\rangle, \\ &= \sum_n c_n e^{-i\hat{K}_F(t)} e^{-\frac{i}{\hbar}\hat{H}_F \times (t-t_0)}|u_n(t_0)\rangle, \\ &= \sum_n c_n e^{-\frac{i}{\hbar}\varepsilon_n \times (t-t_0)} e^{-i\hat{K}_F(t)}|u_n(t_0)\rangle, \\ &= \sum_n c_n e^{-\frac{i}{\hbar}\varepsilon_n \times (t-t_0)}|u_n(t)\rangle, \end{aligned} \quad (\text{B.9})$$

where $|u_n(t)\rangle = e^{-i\hat{K}_F(t)}|u_n(t_0)\rangle$ with $|u_n(t)\rangle = |u_n(t+T)\rangle$, and in the literature the states

$$|\psi_n(t)\rangle = e^{-\frac{i}{\hbar}\varepsilon_n \times (t-t_0)}|u_n(t)\rangle, \quad (\text{B.10})$$

are often called “*Floquet states*” in analogy with the Bloch theorem.

B.2 Alternative Approaches to Numerical Solutions

In the following subsections, we explore additional methods for numerically solving the Floquet problem, either directly or through approximations of the time evolution operator $\hat{U}(t_0 + T, t_0)$.

B.2.1 Exact Time-Evolution of $\hat{U}(t_0 + T, t_0)$

If the Hilbert space of $\hat{H}(t)$ is not excessively large and its analytical form is not overly complex, it is possible to obtain $\hat{U}(t_0 + T, t_0)$ by integrating the time-dependent Schrödinger equation over one period, i.e., by solving the Schrödinger equation in the standard manner. First, the initial state is expanded in the Floquet modes:

$$|\psi(t_0)\rangle = \sum_n c_n(t_0) |u_n(t_0)\rangle. \quad (\text{B.11})$$

The state $|\psi(t_0)\rangle$ is then evolved over one period according to the time-dependent Schrödinger equation:

$$i\hbar \frac{d}{dt} c_n(t) = \sum_m H_{nm}(t) c_m(t). \quad (\text{B.12})$$

This results in a set of n coupled differential equations for each coefficient $c_n(t_0)$ from t_0 to $t_0 + T$. The solutions to this set of differential equations provide the time-evolved vectors $\{c_n(t_0 + T)\}$, which are directly related to the columns of $\hat{U}(t_0 + T, t_0)$. Diagonalizing this matrix yields the Floquet multipliers $\left\{e^{-\frac{i}{\hbar}\varepsilon_n T}\right\}$, thereby providing all the necessary components to reconstruct the state at any time t .

Clearly, solving a set of n coupled differential equations is not a trivial numerical task. Therefore, this approach is recommended only for cases where the dimension of the Hamiltonian is relatively small (which is not the our case) and the functional form of the Hamiltonian is not overly complex.

B.2.2 Trotter Decomposition of $\hat{U}(t_0 + T, t_0)$

If the Hilbert space is too large, a direct numerical integration of Eq. (B.12) can become impractical. In such cases, an alternative approach is the Trotter decomposition of the time-evolution operator [94], which involves dividing the timespan $[t_0, t_0 + T]$ into N segments $t_i = t_0 + i\Delta t$ with $\Delta t = \frac{T}{N}$ (see Fig B.3). The time-evolution operator can then be approximated as follows:

$$\begin{aligned}
 \hat{U}(t_0 + T, t_0) &= \mathcal{T} \exp \left(-\frac{i}{\hbar} \int_{t_0}^{t_0+T} \hat{H}(t) dt \right), \\
 &\approx \exp \left(-\frac{i}{\hbar} \sum_{i=0}^{N-1} \hat{H}(t_i) \Delta t \right), \\
 &\approx \prod_{i=0}^{N-1} \exp \left(-\frac{i}{\hbar} \hat{H}(t_i) \Delta t \right) + \mathcal{O}(\Delta t^2).
 \end{aligned} \tag{B.13}$$

Here, \mathcal{T} denotes time-ordering, and the third line represents the Trotter decomposition, i.e., transitioning from the exponential of a sum to the product of exponentials. This can be challenging because Hamiltonians at different times generally do not commute, i.e., $[\hat{H}(t_1), \hat{H}(t_2)] \neq 0$. The Trotter decomposition ensures that the error introduced by ignoring the commutators is only $\mathcal{O}(\Delta t^2)$, meaning it decreases quadratically with the duration of each time-step. During each time-step, the Hamiltonian $\hat{H}(t_i)$ is assumed to be constant, thereby reducing the time-ordered integral to a product of exponentiated matrices. As before, diagonalizing $\hat{U}(t_0 + T, t_0)$ yields the Floquet multipliers $\left\{ e^{-\frac{i}{\hbar} \varepsilon_n T} \right\}$, providing all the necessary components to reconstruct the state at any time t .

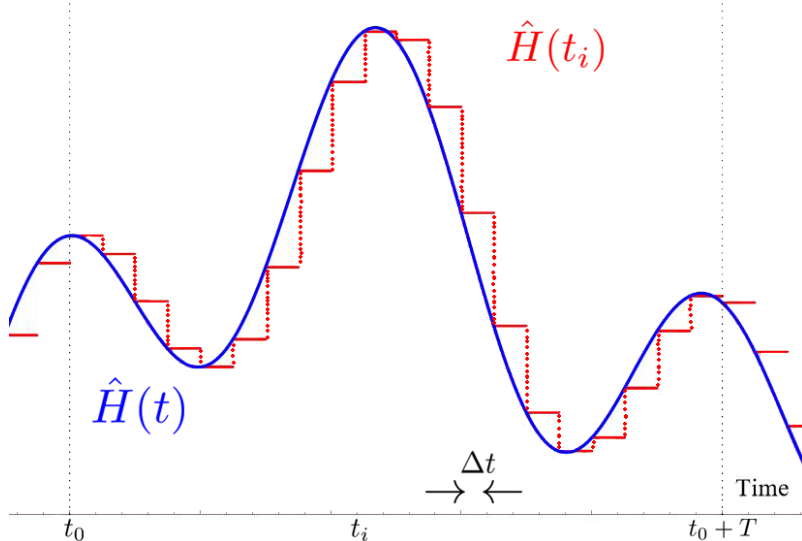


Figure B.3: Trotter decomposition of the time-evolution operator $\hat{U}(t_0 + T, t_0)$. The time-axis is discretized in units of Δt , taking the Hamiltonian $\hat{H}(t_i)$ to be constant at each instant.

B.3 Summary of important definitions

Name(s)	Definition	Expression
Floquet Hamiltonian	A Hermitian operator that extends the concept of the Hamiltonian to include the effects of periodic variations in a quantum system.	$\hat{H}_F = \hat{H}(t) - i\hbar \frac{d}{dt}$
Floquet modes	The eigenstates of the Floquet Hamiltonian, which define the basis of the system.	$ u_n(t_0)\rangle$
Quasienergies	The eigenvalues of the Floquet Hamiltonian, serving as the replacement for energy in the system. The term originates from the analogy with quasimomentum in Bloch's theorem.	$\varepsilon_n \sim \hbar\omega$
Floquet operator \\\ Floquet propagator \\\ Slow-motion operator	A time-evolution operator that governs the “slow dynamics,” i.e., the dynamics from one interval to another in the system. Its respective generator is the Floquet Hamiltonian.	$e^{-\frac{i}{\hbar} \hat{H}_F \times (t-t_0)}$
Floquet multipliers	The exponentials of the quasienergies and the corresponding eigenvalues of the Floquet operator.	$e^{-\frac{i}{\hbar} \varepsilon_n \times (t-t_0)}$
Stroboscopic kick operator	An operator that describes how the state of a quantum system changes after one complete cycle of the periodic perturbation.	$\hat{K}_F(t)$
Fast-motion operator	A time-evolution operator that governs the “fast dynamics,” i.e., the dynamics within an interval in the system. Its respective generator is the Stroboscopic operator.	$e^{-\frac{i}{\hbar} \hat{K}_F(t)}$
Floquet states	The solutions of the time-dependent Schrödinger equation, expanded in terms of Floquet modes and Floquet multipliers. The term draws an analogy with Bloch states in Bloch's theorem.	$ \psi_n(t)\rangle = e^{-\frac{i}{\hbar} \varepsilon_n t} u_n(t)\rangle$
Floquet-Brillouin zone	The zone that, in analogy with solid state theory, contains all distinct Floquet state solutions to the Schrödinger equation.	$\varepsilon_{min} < \varepsilon_n < \varepsilon_{min} + \hbar\omega$

Table B.1: Summary of important concepts discussed in this document.

Appendix C

FLOQUET'S IMPLEMENTATION IN C/C++

This appendix provides more detailed information about the numerical implementation used in this work. It serves as a guide for implementing the extended Hilbert space method of Floquet theory in other physical systems or as an instruction manual for further research into the spin-1 Bose-Hubbard model. It includes the names of the essential libraries and programs required for implementing the numerical technique. As well as a description of how to create the Hamiltonian of the system from the local operators of the basis.

C.0 Numerical Implementation Details

The first observation to note is that the numerical implementation of the extended Hilbert space method, as described by Floquet theory, is carried out in C/C++. This language is chosen for its efficiency in controlling system resources and its ability to compile directly to machine code, which enables significantly faster execution compared to interpreted or bytecode-compiled languages such as Python. Additionally, C/C++ allows the use of robust and well-optimized libraries in the field of linear algebra. Given the requirements of the method, the resources employed are as follows:

1. **Linear Algebra Handling:** The extended Hilbert space method and state reconstruction are managed using a matrix representation of the system. All operations involving matrices, vectors, tensors, and basic linear algebra routines are handled with the Boost library, specifically the uBLAS module. This module facilitates the manipulation, operation, and measurement of various observables and necessary states (for more information, see https://www.boost.org/doc/libs/1_85_0/libs/numeric/ublas/doc/index.html). Additionally, standard C/C++ libraries are utilized to handle arrays for matrix and vector blocks, as used in the Floquet matrix.
2. **Numerical Integration:** As discussed in Chapter 3, the extended Hilbert space method requires the calculation of various Fourier coefficients, as expressed in Eq. (3.11), which necessitates numerical integration. This integration is performed using the trapezoidal quadrature method, implemented via the Math module of the Boost library. This module

includes a variety of mathematical tools such as constants, special functions, interpolation, differentiation, and numerical integration, among others (for more information, see https://www.boost.org/doc/libs/1_85_0/libs/math/doc/html/index.html). The trapezoidal quadrature method is chosen for its simplicity and efficiency in integrating periodic functions both rapidly and accurately [95].

3. **Diagonalization:** As noted in Chapter 3, the extended Hilbert space method requires diagonalization of the Floquet matrix. This process is accomplished using a static library provided by the Solid State Physics Theory research group of the Physics Department, which employs the LAPACK subroutine “*zheev*.” This subroutine returns the eigenvalues and eigenvectors of a Hermitian matrix.
4. **Compilation and Plotting:** It is advisable to include flags during the command or compilation of the code to identify potential errors. Since repeating this process can be uncomfortable, we utilize the make program and create a Makefile to register all necessary flags and commands for compilation and execution. Once the code is compiled and executed, the measured observables are plotted using .dat files with the assistance of the Gnuplot program.

It is also important to note that the numerical implementation of the system, from coding the local matrices, integration, and diagonalization to state reconstruction and measurement of observables, is conducted within a single .cpp file. This approach allows for direct modification of system parameters within the source code, which is then compiled, executed, and plotted for each variation. Despite this setup, and considering the cases addressed in Chapter 4, the numerical implementation of the extended Hilbert space method under Floquet's theorem proves to be both efficient and practical for periodic systems.

C.0 Construction of the Hamiltonian

To generate the matrices for the entire system and therefore the complete Hamiltonian, we employ the standard construction of non-local matrices in a lattice from the local ones using the Kronecker product. Let \hat{O}_i be a local operator at site i with dimension $n_l \times n_l$. To generate the operator that acts on a state of the complete lattice with L sites, we construct it as follows:

$$\hat{O} = \hat{O}_1 \otimes \underbrace{\hat{I}_v \otimes \cdots \otimes \hat{I}_v}_{L-1} + \hat{O}_2 \otimes \underbrace{\hat{I}_v \otimes \cdots \otimes \hat{I}_v}_{L-2} + \cdots + \underbrace{\hat{I}_v \otimes \cdots \otimes \hat{I}_v}_{L-1} \otimes \hat{O}_L$$

$$\hat{O} = \sum_{i=0}^{L-1} \hat{I}_v^{\otimes i} \otimes \hat{O}_{i+1} \otimes \hat{I}_v^{\otimes(L-1-i)}, \quad (\text{C.1})$$

where \otimes represents the tensor product or Kronecker product, and \hat{I}_v is the vacuum identity operator, which has a 1 in the vacuum state and 0 in the other local states, namely:

$$I_v = \underbrace{\begin{pmatrix} 1 & 0 & \cdots & 0 \\ 0 & 0 & \cdots & 0 \\ \vdots & \vdots & \ddots & \vdots \\ 0 & 0 & \cdots & 0 \end{pmatrix}}_{n_l}. \quad (\text{C.2})$$

This matrix represents the addition of an empty site in the lattice, and $\hat{I}_v^{\otimes n}$ represents the tensor product of the vacuum identity operator with itself n times, i.e., $\hat{I}_v^{\otimes 0} = 1$, $\hat{I}_v^{\otimes 1} = \hat{I}_v$, $\hat{I}_v^{\otimes 2} = \hat{I}_v \otimes \hat{I}_v$, and so on.

This construction is used to generate the matrices of the entire system from the local ones. If the local operator is defined over two or more sites (such as the hopping term), the sum must be adjusted to consider the tensor product with the remaining sites. Note also that, in our system, the tensor product is performed with the vacuum identity operator, thereby adding only sites and not particles. If we wish to add more sites that can also host particles, we must use the standard identity operator.

This method was implemented only for the two-particle system, as the one-particle system allows for the matrices of the entire system to be easily constructed by considering only the effective states. The Kronecker product generates a matrix with all mathematically possible states; however, since only empty sites are added and not all of them are physically relevant, considering all states results in $(n_l)^L$ states, significantly increasing computational cost.

Appendix D

ADDITIONAL FINDINGS ON THE DYNAMICAL ANALYSIS

Given that the system under analysis permits the variation of numerous parameters, this appendix aims to provide a more in-depth exploration of the behavior of the observables by examining different initial states and other relevant configurations. First, the scenario involving a single particle is explored, with a focus on the impact of relative phases in the initial states, such as quadrupolar states. Subsequently, the behavior of the system is examined under changes in the driving conditions, including variations in the coupling amplitude and the low-frequency regime. Finally, in the case of two particles, the analysis is extended to consider a greater number of lattice sites.

D.1 One Particle

As mentioned in the dynamic analysis of a single particle, additional variations in the system's parameters can be made, with particular interest in the effects of relative phases and changes in the system's driving, to gain a deeper understanding of the dynamic behavior of spin-1 systems.

D.1.1 Effect of Relative Phases

In the dynamic analysis of a single particle, it was shown that initial states whose superpositions included contributions from the three magnetic projections were influenced by external fields. These contributions are represented as probability amplitudes, which can be either real or complex numbers. This implies that the introduction of relative phases into the system alters its evolution. To illustrate this, consider the equiprobable state $|\psi_\sigma\rangle$ but now in the Cartesian basis, $|\psi_c\rangle$, representing a quadrupolar state of the form:

$$|\psi_c\rangle = \frac{1}{\sqrt{3}}|x\rangle + \frac{1}{\sqrt{3}}|y\rangle + \frac{1}{\sqrt{3}}|z\rangle = \frac{i-1}{\sqrt{6}}|1\rangle - \frac{i-1}{\sqrt{6}}|-1\rangle - \frac{i}{\sqrt{3}}|0\rangle \quad (\text{D.1})$$

Thus, it is essentially the same superposition as in Eq. (4.3), since it includes the same contributions

APPENDIX D. ADDITIONAL FINDINGS ON THE DYNAMICAL ANALYSIS

from each magnetic projection but with relative phases that significantly alter the system's dynamics. To understand how these dynamics are affected, let us examine the weak-driving regime, initially with a linear magnetic field and quadratic driving.

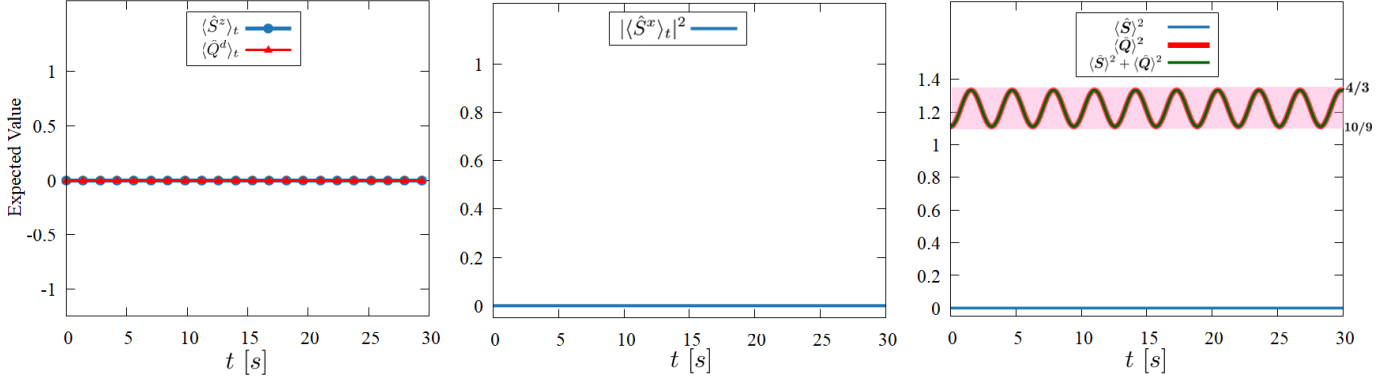


Figure D.1: The expected value in time for the quadrupolar density \hat{Q}_i^d together with the magnetic density \hat{S}_i^z (left), the transverse magnetization \hat{S}_i^x (center), and Spin-Quadrupole competition (right) given the initial state $|\psi_c\rangle$ with $L = 30$, $J = 1$, $\mu = 1$, $D_0 = 1$, $T = 10^{-3}D_0$, and $m = 1$.

As observed in Fig. D.1, the evolution of the observables is similar to what is seen in the absence of relative phases. However, these phases cause both the transverse magnetization and the magnetic density to approach zero, indicating that this initial state is completely confined within the plane, thereby displaying only quadrupolar order, as expected for a quadrupolar state. Conversely, if this initial state is evolved in the presence of a quadratic field instead of a linear one, a notable change occurs.

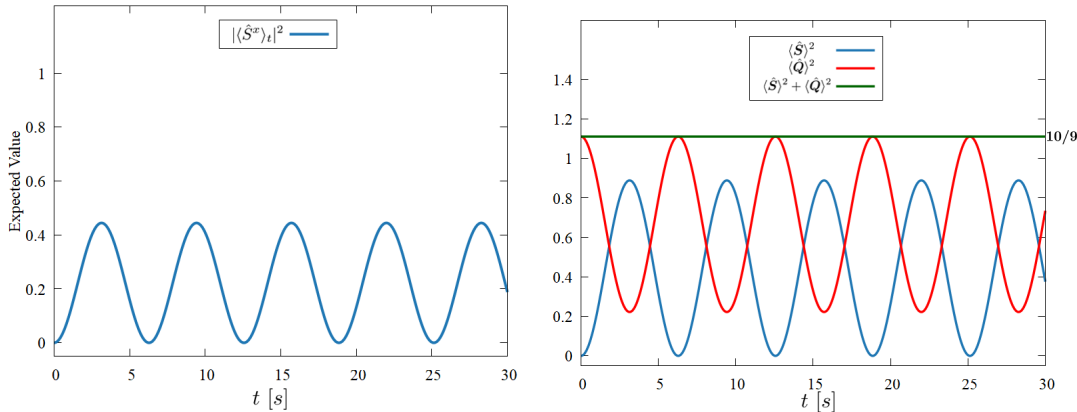


Figure D.2: The expected value in time for the transverse magnetization \hat{S}_i^x (left), Spin-Quadrupole competition (right) given the initial state $|\psi_c\rangle$ with $L = 30$, $J = 1$, $\mu = 1$, $Q_0 = 1$, $T = 10^{-3}Q_0$, and $m = 5$.

APPENDIX D. ADDITIONAL FINDINGS ON THE DYNAMICAL ANALYSIS

As illustrated in Fig. D.2, when a quadratic field is applied instead of a linear one, the competition between quadrupolar order and spin order differs significantly from what is observed in the case of the initial state without relative phases ($|\psi_\sigma\rangle$). Indeed, this competition deviates from the expected behavior described by Eq. (2.31), as the equality no longer aligns with the eigenvalue of the quadratic Casimir operator of SU(3), which is 4/3. Rather, it intriguingly corresponds to the eigenvalue of the cubic Casimir operator of SU(3), which is 10/9 (see Appendix A). Therefore, in this case, the competition between spin and quadrupole order appears to be governed by the relationship $\langle \hat{S} \rangle_t^2 + \langle \hat{Q} \rangle_t^2 = \frac{10}{9}$ satisfying even in this case, with the lower limit the inequality of Eq. (4.4).

D.1.2 Driving Variations

Another variation that can be introduced to the system under study involves modifications to the driving coupled to the field, such as changes in its amplitude and the behavior of the system under a low-frequency regime ($\omega \ll D_0$ or $\omega \ll Q_0$). To begin, let us analyze the first case.

Variations in amplitude

For this analysis, we again consider the equiprobable initial state $|\psi_\sigma\rangle$ under the weak-driving regime, with a linear field and quadratic driving. The impact of varying the driving amplitude D_0 is depicted in Fig. D.3.

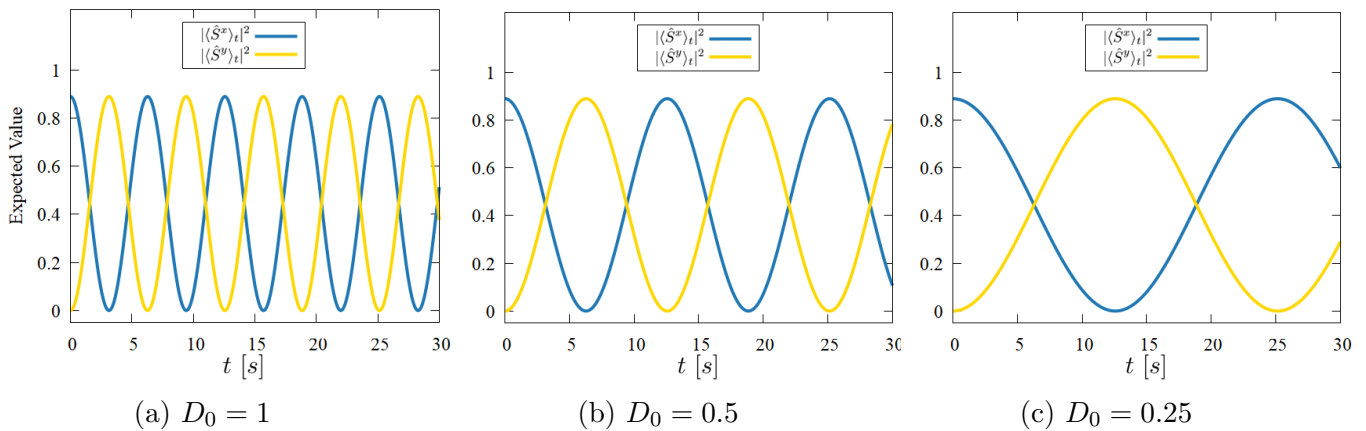


Figure D.3: The expected value in time for the transverse magnetization x and y \hat{S}_i^x, \hat{S}_i^y , given the initial state $|\psi_\sigma\rangle$ for different values of the driving amplitude with $L = 30$, $J = 1$, $\mu = 1$, $T = 10^{-3}D_0$, and $m = 1$.

APPENDIX D. ADDITIONAL FINDINGS ON THE DYNAMICAL ANALYSIS

As illustrated in Fig. D.3, variations in the driving amplitude are manifested in the frequency of the oscillations of the expected values, clearly indicating a relationship between this amplitude and the well-known Larmor frequency [88].

The Larmor frequency refers to the rate at which the spin precesses around the axis aligned with the applied field, and it is directly proportional to the field's magnitude, which, in this context, is represented by the driving amplitude.

Low-frequency regime

As discussed in Chapters 3 and 4, the regimes for studying the system's dynamics via the extended Hilbert space are typically defined by a high-frequency or weak-driving regime, $\omega \gg D_0$, and a medium-frequency or strong-driving regime, $\omega \sim D_0$. It was also noted that further lowering the frequencies to enter a “low-frequency regime,” $\omega \ll D_0$, destabilizes the system to the extent that the state cannot be accurately reconstructed. To illustrate this, let us again consider the equiprobable initial state $|\psi_\sigma\rangle$ with a quadratic field $(\hat{S}^z)^2$ and quadratic driving $(Q_0 \cos^2 \omega t)$, i.e., the same system conditions analyzed in Fig. 4.13 but with $T = 15Q_0$, such that $\omega < Q_0$.

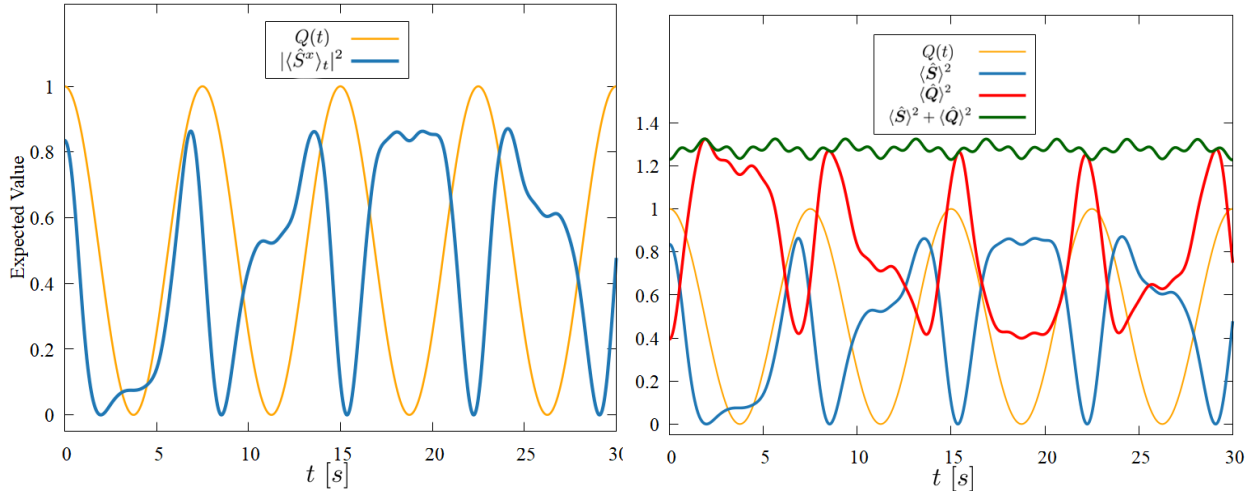


Figure D.4: The expected value in time for the transverse magnetization \hat{S}_i^x (left) and Spin-Quadrupole competition (right), with quadratic driving $Q(t) = Q_0 \cos^2(\omega t)$ given the initial state $|\psi_\sigma\rangle$ with $L = 30$, $J = 1$, $\mu = 1$, $Q_0 = 1$, $T = 15Q_0$, and $m = 8$.

As shown in Fig. D.4, the behavior of the observables at low frequencies deviates significantly from those observed in the weak- and strong-driving regimes. In this case, it is not possible to clearly

distinguish between fast and slow dynamics in the system, making it difficult to assess how the driving explicitly affects the system. Notably, for these low frequencies, eight harmonics $m = 8$ or equivalently 17 blocks of the Floquet matrix were considered. Despite this, complete normalization of the evolved state $\sum_n |c_n|^2 = 0.9796$ could not be achieved, rendering the dynamics observed in the observables unreliable.

Furthermore, even if the number of harmonics were increased indefinitely, it would not be possible to achieve higher precision in the state's normalization, as the extended Hilbert space method is not particularly suited for such scenarios.

Given these considerations, if one wishes to analyze the dynamics of a system under periodic driving at low frequencies, it is advisable to employ alternative numerical approaches based on Floquet's theorem, as mentioned in appendix B, or even explore other entirely different numerical techniques.

D.2 Two particles

As demonstrated in Chapter 4, increasing the number of sites in the two-particle system exponentially enlarges the size of the Hilbert space ($N_T = (n_l)^L$), and therefore, the computational cost also increases exponentially. This makes the dynamic analysis for a typical number of sites in such systems highly complex. However, in the following section, we present the behavior of the system for a number of sites that our computational resources can still manage ($L = 3$), allowing us to make predictions about the evolution in systems with a significantly larger number of sites.

D.2.1 Increase in the number of sites

To illustrate the evolution with an increased number of sites to 3, we use the state where both particles are polarized at 0 ($|0, 0, 2\rangle$), under a quadratic magnetic field $(\hat{S}^z)^2$, with quadratic driving ($Q(t) = Q_0 \cos^2 \omega t$) in the RWA ($Q(t) = Q_0/2 = Q'_0$), focusing on the antiferromagnetic phase, considering open boundary conditions and in time steps of $\delta t = 1$ s in this case.

As shown in Fig. (D.6), the evolution of our two-particle system in the 3-site antiferromagnetic phase evolves similarly to the 2-site system discussed in Chapter 4. However, in this case, the dynamics slow down significantly, requiring a longer time scale for detailed observation. It can also be seen that the collapses and revivals are less distinct than in the 2-site case, with the system maintaining a spin-mixing dynamic characterized by relatively high frequencies. Additionally, the

APPENDIX D. ADDITIONAL FINDINGS ON THE DYNAMICAL ANALYSIS

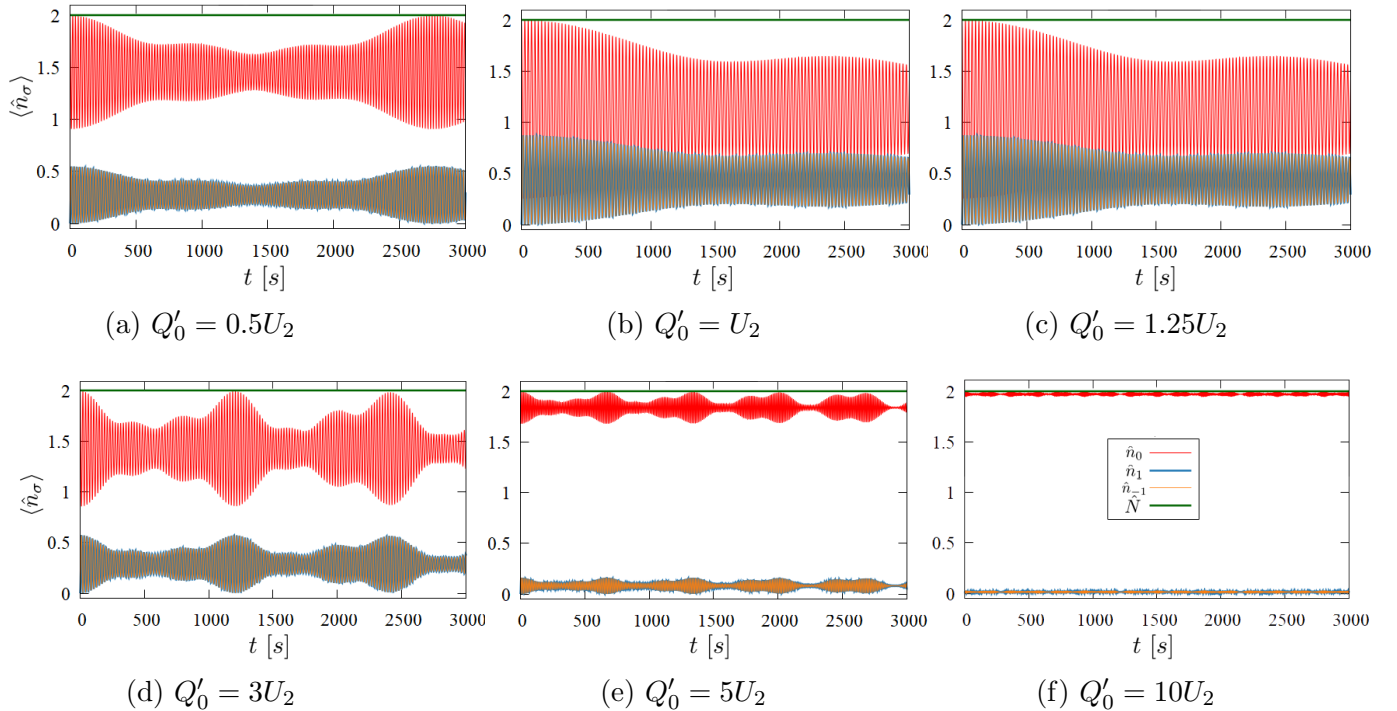


Figure D.6: Spin mixing dynamics, for different values of the quadratic Zeeman coupling in the interaction regime (top row) and the Zeeman regime (bottom row) with $L = 3$, $J = 0.1$, $\mu = 1$, $U_0 = 0.2$ and $U_2 = 0.08$. All graphs share the same key as subfigure (f).

quadratic Zeeman field exhibits the same effect as before, dividing the phase into the same two regimes observed in Chapter 4, namely the Interaction and Zeeman regimes. Furthermore, the spin-mixing resonance in this case was observed at $Q'_0 \approx 1.51U_2$, suggesting that with a greater number of sites, the resonance can be observed at lower field values. However, this could also be influenced by the presence of open boundary conditions.

Therefore, it is evident that the evolution of the system can be analyzed with a larger number of sites. However, as mentioned earlier, the computational cost for this two-particle system increases exponentially. For instance, analyzing a system with just 5 sites would involve working with a matrix of 10^{10} entries. Considering that each entry stores a complex number and each complex number occupies 16 bytes of memory, at least 160 GB of available memory would be required to accurately reconstruct the state. This estimate does not take into account the expansion of the Hilbert space by our extended Hilbert space method, which would necessitate even more memory. Thus, working with such systems on conventional computers becomes highly complex.

BIBLIOGRAPHY

- [1] E. Schrödinger. “An Undulatory Theory of the Mechanics of Atoms and Molecules.” In: *Phys. Rev.* 28 (6 Dec. 1926), pp. 1049–1070. URL: <https://link.aps.org/doi/10.1103/PhysRev.28.1049>.
- [2] P. A. M. Dirac. “The Principles of Quantum Mechanics.” In: *Oxford University Press* (1958). URL: <https://global.oup.com/academic/product/the-principles-of-quantum-mechanics-9780198520115?cc=us&lang=en	>.
- [3] J. S. Bell and Alain Aspect. *Speakable and Unspeakable in Quantum Mechanics: Collected Papers on Quantum Philosophy*. 2nd ed. Cambridge University Press, 2004.
- [4] Zeitschrift für Physik. “Plancks Gesetz und Lichtquantenhypothese.” In: *Phys. Rev.* 26 (1 Dec. 1924), pp. 178–181. URL: <https://doi.org/10.1007/BF01327326>.
- [5] André F. Verbeure. “Bose Einstein Condensation (BEC).” In: *Many-Body Boson Systems: Half a Century Later*. London: Springer London, 2011, pp. 43–107. URL: https://doi.org/10.1007/978-0-85729-109-7_4.
- [6] William D. Phillips. “Nobel Lecture: Laser cooling and trapping of neutral atoms.” In: *Rev. Mod. Phys.* 70 (3 July 1998), pp. 721–741. URL: <https://link.aps.org/doi/10.1103/RevModPhys.70.721>.
- [7] Claude N. Cohen-Tannoudji. “Nobel Lecture: Manipulating atoms with photons.” In: *Rev. Mod. Phys.* 70 (3 July 1998), pp. 707–719. URL: <https://link.aps.org/doi/10.1103/RevModPhys.70.707>.
- [8] Harald F. Hess. “Evaporative cooling of magnetically trapped and compressed spin-polarized hydrogen.” In: *Phys. Rev. B* 34 (5 Sept. 1986), pp. 3476–3479. URL: <https://link.aps.org/doi/10.1103/PhysRevB.34.3476>.
- [9] Kendall B. Davis, Marc-Oliver Mewes, Michael A. Joffe, Michael R. Andrews, and Wolfgang Ketterle. “Evaporative Cooling of Sodium Atoms.” In: *Phys. Rev. Lett.* 74 (26 June 1995), pp. 5202–5205. URL: <https://link.aps.org/doi/10.1103/PhysRevLett.74.5202>.
- [10] M. H. Anderson, J. R. Ensher, M. R. Matthews, C. E. Wieman, and E. A. Cornell. “Observation of Bose-Einstein Condensation in a Dilute Atomic Vapor.” In: *Science* 269.5221 (1995), pp. 198–201. URL: <https://www.science.org/doi/abs/10.1126/science.269.5221.198>.

BIBLIOGRAPHY

- [11] Claude N. Cohen-Tannoudji and William D. Phillips. “New Mechanisms for Laser Cooling.” In: *Physics Today* 43.10 (Oct. 1990), pp. 33–40. URL: <https://doi.org/10.1063/1.881239>.
- [12] Wolfgang Ketterle. “Nobel lecture: When atoms behave as waves: Bose-Einstein condensation and the atom laser.” In: *Rev. Mod. Phys.* 74 (4 Nov. 2002), pp. 1131–1151. URL: <https://link.aps.org/doi/10.1103/RevModPhys.74.1131>.
- [13] Roy J. Glauber. “The Quantum Theory of Optical Coherence.” In: *Phys. Rev.* 130 (6 June 1963), pp. 2529–2539. URL: <https://link.aps.org/doi/10.1103/PhysRev.130.2529>.
- [14] Iulia Georgescu. “Nobel Prize 2012: Haroche & Wineland.” In: *Nature Physics* 8 (2012), pp. 777–777. URL: <https://doi.org/10.1038/nphys2472>.
- [15] Nobel Prize. *The Nobel Prize in Physics 2016*. <https://www.nobelprize.org/prizes/physics/2016/summary/>. 2016.
- [16] John F. Clauser, Michael A. Horne, Abner Shimony, and Richard A. Holt. “Proposed Experiment to Test Local Hidden-Variable Theories.” In: *Phys. Rev. Lett.* 23 (15 Oct. 1969), pp. 880–884. URL: <https://link.aps.org/doi/10.1103/PhysRevLett.23.880>.
- [17] Immanuel Bloch. “Ultracold quantum gases in optical lattices.” In: *Nature Physics* 1 (2005), pp. 23–30. URL: <https://www.nature.com/articles/nphys138>.
- [18] Tetsuo Ohmi and Kazushige Machida. “Bose-Einstein Condensation with Internal Degrees of Freedom in Alkali Atom Gases.” In: *Journal of the Physical Society of Japan* 67.6 (1998), pp. 1822–1825. URL: <https://doi.org/10.1143/JPSJ.67.1822>.
- [19] SHI-JIAN GU. “FIDELITY APPROACH TO QUANTUM PHASE TRANSITIONS.” In: *International Journal of Modern Physics B* 24.23 (2010), pp. 4371–4458. URL: <https://doi.org/10.1142/S0217979210056335>.
- [20] Immanuel Bloch, Jean Dalibard, and Sylvain Nascimbène. “Quantum simulations with ultracold quantum gases.” In: *Nature Physics* 8 (2012), pp. 267–276. URL: <https://www.nature.com/articles/nphys2259>.
- [21] Gavin K. Brennen, Carlton M. Caves, Poul S. Jessen, and Ivan H. Deutsch. “Quantum Logic Gates in Optical Lattices.” In: *Phys. Rev. Lett.* 82 (5 Feb. 1999), pp. 1060–1063. URL: <https://link.aps.org/doi/10.1103/PhysRevLett.82.1060>.

BIBLIOGRAPHY

- [22] Jose Carlos Pelayo, Karol Gietka, and Thomas Busch. “Distributed quantum sensing with optical lattices.” In: *Phys. Rev. A* 107 (3 Mar. 2023), p. 033318. URL: <https://link.aps.org/doi/10.1103/PhysRevA.107.033318>.
- [23] C. A. Weidner and Dana Z. Anderson. “Experimental Demonstration of Shaken-Lattice Interferometry.” In: *Phys. Rev. Lett.* 120 (26 June 2018), p. 263201. URL: <https://link.aps.org/doi/10.1103/PhysRevLett.120.263201>.
- [24] Dragomir Neshev, Andrey Sukhorukov, Arnan Mitchell, Christian Rosberg, Robert Fischer, Alexander Dreishuh, Wieslaw Krolikowski, and Yuri Kivshar. “Optical lattices as nonlinear photonic crystals.” eng. In: Bulgaria: SPIE, 2007, 66041B.
- [25] Ana Maria Rey. “Ultra-cold bosonic atoms in optical lattices: An Overview.” en. In: *Revista de la Academia Colombiana de Ciencias Exactas, Físicas y Naturales* 45 (Sept. 2021), pp. 666–696. URL: http://www.scielo.org.co/scielo.php?script=sci_arttext&pid=S0370-39082021000300666&nrm=iso.
- [26] P.S. Jessen and I.H. Deutsch. “Optical Lattices.” In: ed. by Benjamin Bederson and Herbert Walther. Vol. 37. Advances In Atomic, Molecular, and Optical Physics. Academic Press, 1996, pp. 95–138. URL: <https://www.sciencedirect.com/science/article/pii/S1049250X08600993>.
- [27] Markus Greiner, Olaf Mandel, Tilman Esslinger, Theodor W. Hänsch, and Immanuel Bloch. “Quantum phase transition from a superfluid to a Mott insulator in a gas of ultracold atoms.” In: *Nature Physics* 415 (2002), pp. 39–44. URL: <https://www.nature.com/articles/415039a>.
- [28] Tian-Heng Han, Joel S. Helton, Shaoyan Chu, Daniel G. Nocera, Jose A. Rodriguez-Rivera, Collin Broholm, and Young S. Lee. “Fractionalized excitations in the spin-liquid state of a kagome-lattice antiferromagnet.” In: *Nature Physics* 492 (2012), pp. 406–410. URL: <https://doi.org/10.1038/nature11659>.
- [29] Dominik Suszalski and Jakub Zakrzewski. “Different lattice geometries with a synthetic dimension.” In: *Phys. Rev. A* 94 (3 Sept. 2016), p. 033602. URL: <https://link.aps.org/doi/10.1103/PhysRevA.94.033602>.
- [30] D. Einzel. “Superfluids.” In: *Encyclopedia of Mathematical Physics*. Ed. by Jean-Pierre Francoise, Gregory L. Naber, and Tsou Sheung Tsun. Oxford: Academic Press, 2006, pp. 115–121. URL: <https://www.sciencedirect.com/science/article/pii/B0125126662001103>.

BIBLIOGRAPHY

- [31] Piers Coleman. *Introduction to Many-Body Physics*. Cambridge University Press, 2015.
- [32] Rui Asaoka, Hiroki Tsuchiura, Makoto Yamashita, and Yuta Toga. “Dynamical instability in the $S = 1$ Bose-Hubbard model.” In: *Phys. Rev. A* 93 (1 Jan. 2016), p. 013628. URL: <https://link.aps.org/doi/10.1103/PhysRevA.93.013628>.
- [33] L. de Forges de Parny and V. G. Rousseau. “Phase diagrams of antiferromagnetic spin-1 bosons on a square optical lattice with the quadratic Zeeman effect.” In: *Phys. Rev. A* 97 (2 Feb. 2018), p. 023628. URL: <https://link.aps.org/doi/10.1103/PhysRevA.97.023628>.
- [34] K. Rodríguez, A. Argüelles, A. K. Kolezhuk, L. Santos, and T. Vekua. “Field-Induced Phase Transitions of Repulsive Spin-1 Bosons in Optical Lattices.” In: *Phys. Rev. Lett.* 106 (10 Mar. 2011), p. 105302. URL: <https://link.aps.org/doi/10.1103/PhysRevLett.106.105302>.
- [35] Felipe Reyes Osorio and Karen Rodríguez Ramírez. “Separation of quadrupole, spin, and charge across the magnetic phases of a one-dimensional interacting spin-1 gas.” In: *Phys. Rev. B* 107 (8 Feb. 2023), p. 085424. URL: <https://link.aps.org/doi/10.1103/PhysRevB.107.085424>.
- [36] Lode Pollet. “Recent developments in quantum Monte Carlo simulations with applications for cold gases.” In: *Reports on Progress in Physics* 75.9 (Aug. 2012), p. 094501. URL: <https://dx.doi.org/10.1088/0034-4885/75/9/094501>.
- [37] Alexei Filinov, Jens Böning, and Michael Bonitz. “Path Integral Monte Carlo Simulation of Charged Particles in Traps.” In: *Computational Many-Particle Physics*. Ed. by H. Fehske, R. Schneider, and A. Weiße. Berlin, Heidelberg: Springer Berlin Heidelberg, 2008, pp. 397–412. URL: https://doi.org/10.1007/978-3-540-74686-7_13.
- [38] U. Schollwöck. “The density-matrix renormalization group.” In: *Rev. Mod. Phys.* 77 (1 Apr. 2005), pp. 259–315. URL: <https://link.aps.org/doi/10.1103/RevModPhys.77.259>.
- [39] Martin C. Gutzwiller. “Effect of Correlation on the Ferromagnetism of Transition Metals.” In: *Phys. Rev. Lett.* 10 (5 Mar. 1963), pp. 159–162. URL: <https://link.aps.org/doi/10.1103/PhysRevLett.10.159>.
- [40] Sebastiano Peotta and Massimiliano Di Ventra. *Improving the Gutzwiller Ansatz with Matrix Product States*. 2013.

BIBLIOGRAPHY

- [41] Jae-yoon Choi, Sebastian Hild, Johannes Zeiher, Peter Schauß, Antonio Rubio-Abadal, Tarik Yefsah, Vedika Khemani, David A. Huse, Immanuel Bloch, and Christian Gross. “Exploring the many-body localization transition in two dimensions.” In: *Science* 352.6293 (2016), pp. 1547–1552. URL: <https://www.science.org/doi/abs/10.1126/science.aaf8834>.
- [42] K. Sengupta. *Entanglement in Spin Chains: From Theory to Quantum Technology Applications*. Springer International Publishing, 2022. URL: <http://dx.doi.org/10.1007/978-3-031-03998-0>.
- [43] C. K. Law, H. Pu, and N. P. Bigelow. “Quantum Spins Mixing in Spinor Bose-Einstein Condensates.” In: *Phys. Rev. Lett.* 81 (24 Dec. 1998), pp. 5257–5261. URL: <https://link.aps.org/doi/10.1103/PhysRevLett.81.5257>.
- [44] Rui Asaoka, Hiroki Tsuchiura, Makoto Yamashita, and Yuta Toga. “Dynamical instability in the $S = 1$ Bose-Hubbard model.” In: *Phys. Rev. A* 93 (1 Jan. 2016), p. 013628. URL: <https://link.aps.org/doi/10.1103/PhysRevA.93.013628>.
- [45] K. W. Mahmud and E. Tiesinga. “Dynamics of spin-1 bosons in an optical lattice: Spin mixing, quantum-phase-revival spectroscopy, and effective three-body interactions.” In: *Phys. Rev. A* 88 (2 Aug. 2013), p. 023602. URL: <https://link.aps.org/doi/10.1103/PhysRevA.88.023602>.
- [46] Mark S. Rudner and Netanel H. Lindner. *The Floquet Engineer’s Handbook*. 2020.
- [47] G. Floquet. “Sur les équations différentielles linéaires à coefficients périodiques.” fr. In: *Annales scientifiques de l’École Normale Supérieure* 2e série, 12 (1883), pp. 47–88. URL: <http://www.numdam.org/articles/10.24033/asens.220/>.
- [48] Milena Grifoni and Peter Hänggi. “Driven quantum tunneling.” In: *Physics Reports* 304.5 (1998), pp. 229–354. URL: <https://www.sciencedirect.com/science/article/pii/S0370157398000222>.
- [49] Sho Higashikawa, Hiroyuki Fujita, and Masahiro Sato. *Floquet engineering of classical systems*. 2018. URL: <https://arxiv.org/abs/1810.01103>.
- [50] Wen Wei Ho, Takashi Mori, Dmitry A. Abanin, and Emanuele G. Dalla Torre. “Quantum and classical Floquet prethermalization.” In: *Annals of Physics* 454 (July 2023), p. 169297. URL: <http://dx.doi.org/10.1016/j.aop.2023.169297>.

BIBLIOGRAPHY

- [51] Cheng-Jie Liu, Yu-Chen Meng, Jie-Li Qin, and Lu Zhou. “Classical and Quantum chaos in a spin-1 atomic Bose–Einstein condensate via Floquet driving.” In: *Results in Physics* 43 (2022), p. 106091. URL: <https://www.sciencedirect.com/science/article/pii/S2211379722007057>.
- [52] Mark S. Rudner and Netanel H. Lindner. “Band structure engineering and non-equilibrium dynamics in Floquet topological insulators.” In: *Nature Reviews Physics* 2.5 (May 2020), pp. 229–244. URL: <https://doi.org/10.1038/s42254-020-0170-z>.
- [53] Takashi Oka and Sota Kitamura. “Floquet Engineering of Quantum Materials.” In: *Annual Review of Condensed Matter Physics* 10. Volume 10, 2019 (2019), pp. 387–408. URL: <https://www.annualreviews.org/content/journals/10.1146/annurev-conmatphys-031218-013423>.
- [54] Krzysztof Sacha. “Discrete Time Crystals and Related Phenomena.” In: *Time Crystals*. Cham: Springer International Publishing, 2020, pp. 39–172. URL: https://doi.org/10.1007/978-3-030-52523-1_4.
- [55] Martin Holthaus. “Floquet engineering with quasienergy bands of periodically driven optical lattices.” In: *Journal of Physics B: Atomic, Molecular and Optical Physics* 49.1 (Nov. 2015), p. 013001. URL: <http://dx.doi.org/10.1088/0953-4075/49/1/013001>.
- [56] André Eckardt, Christoph Weiss, and Martin Holthaus. “Superfluid-Insulator Transition in a Periodically Driven Optical Lattice.” In: *Phys. Rev. Lett.* 95 (26 Dec. 2005), p. 260404. URL: <https://link.aps.org/doi/10.1103/PhysRevLett.95.260404>.
- [57] D. Jaksch, C. Bruder, J. I. Cirac, C. W. Gardiner, and P. Zoller. “Cold Bosonic Atoms in Optical Lattices.” In: *Phys. Rev. Lett.* 81 (15 Oct. 1998), pp. 3108–3111. URL: <https://link.aps.org/doi/10.1103/PhysRevLett.81.3108>.
- [58] Tin-Lun Ho. “Bose-Einstein Condensation in Dilute Gases.” In: *Physics Today* 56.6 (June 2003), pp. 62–63. URL: <https://doi.org/10.1063/1.1595060>.
- [59] T. D. Kühner and H. Monien. “Phases of the one-dimensional Bose-Hubbard model.” In: *Phys. Rev. B* 58 (22 Dec. 1998), R14741–R14744. URL: <https://link.aps.org/doi/10.1103/PhysRevB.58.R14741>.

BIBLIOGRAPHY

- [60] N. Elstner and H. Monien. “Dynamics and thermodynamics of the Bose-Hubbard model.” In: *Phys. Rev. B* 59 (19 May 1999), pp. 12184–12187. URL: <https://link.aps.org/doi/10.1103/PhysRevB.59.12184>.
- [61] Ghassan George Batrouni and Richard T. Scalettar. “World-line quantum Monte Carlo algorithm for a one-dimensional Bose model.” In: *Phys. Rev. B* 46 (14 Oct. 1992), pp. 9051–9062. URL: <https://link.aps.org/doi/10.1103/PhysRevB.46.9051>.
- [62] Adilet Imambekov, Mikhail Lukin, and Eugene Demler. “Spin-exchange interactions of spin-one bosons in optical lattices: Singlet, nematic, and dimerized phases.” In: *Phys. Rev. A* 68 (6 Dec. 2003), p. 063602. URL: <https://link.aps.org/doi/10.1103/PhysRevA.68.063602>.
- [63] Frank Deuretzbacher. “Spinor Tonks-Girardeau gases and ultracold molecules.” PhD thesis. Mar. 2009.
- [64] Tamás András Tóth. “Quadrupolar Ordering in Two-Dimensional Spin-One Systems.” PhD thesis. ÉCOLE POLYTECHNIQUE FÉDÉRALE DE LAUSANN, Feb. 2011.
- [65] Davide Castelvecchi. “The Stern–Gerlach experiment at 100.” In: *Nature Reviews Physics* 4.3 (Mar. 2022), pp. 140–142. URL: <https://doi.org/10.1038/s42254-022-00436-4>.
- [66] A.S. Peletinskii, S.V. Peletinskii, and Yu.V. Slyusarenko. “SU(3) symmetry in theory of a weakly interacting gas of spin-1 atoms with Bose-Einstein condensate.” In: *Physics Letters A* 384.31 (2020), p. 126798. URL: <https://www.sciencedirect.com/science/article/pii/S0375960120306654>.
- [67] J. J. Sakurai and Jim Napolitano. “Theory of Angular Momentum.” In: *Modern Quantum Mechanics*. Cambridge University Press, 2020, pp. 149–248.
- [68] Kimberly Remund, Rico Pohle, Yutaka Akagi, Judit Romhányi, and Nic Shannon. “Semi-classical simulation of spin-1 magnets.” In: *Physical Review Research* 4.3 (Aug. 2022). URL: <http://dx.doi.org/10.1103/PhysRevResearch.4.033106>.
- [69] M S Bulakhov, A S Peletinskii, S V Peletinskii, and Yu V Slyusarenko. “Magnetic phases and phase diagram of spin-1 condensate with quadrupole degrees of freedom.” In: *Journal of Physics A: Mathematical and Theoretical* 54.16 (Mar. 2021), p. 165001. URL: <http://dx.doi.org/10.1088/1751-8121/abed16>.

BIBLIOGRAPHY

- [70] Jakob Schwichtenberg. *Physics from Symmetry*. 2nd ed. Undergraduate Lecture Notes in Physics. Physics and Astronomy, Physics and Astronomy (R0). Cham: Springer Cham, Dec. 2018, pp. XXI, 287. URL: <https://doi.org/10.1007/978-3-319-66631-0>.
- [71] N. Papanicolaou. “Unusual phases in quantum spin-1 systems.” In: *Nuclear Physics B* 305.3 (1988), pp. 367–395. URL: <https://www.sciencedirect.com/science/article/pii/0550321388900739>.
- [72] Satoru Hayami and Kazumasa Hattori. “Multiple-q Dipole–Quadrupole Instability in Spin-1 Triangular-lattice Systems.” In: *Journal of the Physical Society of Japan* 92.12 (Dec. 2023). URL: <http://dx.doi.org/10.7566/JPSJ.92.124709>.
- [73] Waseem S. Bakr, Jonathon I. Gillen, Amy Peng, Simon Fölling, and Markus Greiner. “A quantum gas microscope for detecting single atoms in a Hubbard-regime optical lattice.” In: *Nature* 462.7269 (Nov. 2009), pp. 74–77. URL: <https://doi.org/10.1038/nature08482>.
- [74] Wenxian Zhang, D. L. Zhou, M.-S. Chang, M. S. Chapman, and L. You. “Dynamical Instability and Domain Formation in a Spin-1 Bose-Einstein Condensate.” In: *Phys. Rev. Lett.* 95 (18 Oct. 2005), p. 180403. URL: <https://link.aps.org/doi/10.1103/PhysRevLett.95.180403>.
- [75] Y. Liu, E. Gomez, S. E. Maxwell, L. D. Turner, E. Tiesinga, and P. D. Lett. “Number Fluctuations and Energy Dissipation in Sodium Spinor Condensates.” In: *Phys. Rev. Lett.* 102 (22 June 2009), p. 225301. URL: <https://link.aps.org/doi/10.1103/PhysRevLett.102.225301>.
- [76] Marin Bukov, Luca D’Alessio, and Anatoli Polkovnikov. “Universal high-frequency behavior of periodically driven systems: from dynamical stabilization to Floquet engineering.” In: *Advances in Physics* 64.2 (Mar. 2015), pp. 139–226. URL: <http://dx.doi.org/10.1080/00018732.2015.1055918>.
- [77] María Carolina Spinel Gómez. “Dinámica Cuántica.” In: *Introducción al formalismo de la mecánica cuántica no relativista*. 2009. URL: <https://repositorio.unal.edu.co/handle/unal/84250>.
- [78] Ya. B. Zel’Dovich. “The Quasienergy of a Quantum-mechanical System Subjected to a Periodic Action.” In: *Soviet Journal of Experimental and Theoretical Physics* 24 (May 1967), p. 1006.

BIBLIOGRAPHY

- [79] V. I. Ritus. “Shift and Splitting of Atomic Energy Levels by the Field of an Electromagnetic Wave.” In: *Soviet Journal of Experimental and Theoretical Physics* 24 (May 1967), p. 1041.
- [80] Charles Kittel. “Energy Bands.” In: *Introduction to Solid State Physics*. 8th. Library of Congress Cataloging in Publication Data: QC176.K5 2005, 530.4'1—dc22 2004042250. Hoboken, NJ: John Wiley & Sons, Inc, 2005.
- [81] V. Lyssenko and K. Leo. “2.09 - Bloch Oscillations and Ultrafast Coherent Optical Phenomena.” In: *Comprehensive Semiconductor Science and Technology*. Ed. by Pallab Bhattacharya, Roberto Fornari, and Hiroshi Kamimura. Amsterdam: Elsevier, 2011, pp. 343–399. URL: <https://www.sciencedirect.com/science/article/pii/B9780444531537000778>.
- [82] Mina Udono, Tatsuya Kaneko, and Koudai Sugimoto. “Wannier-Stark ladders and Stark shifts of excitons in Mott insulators.” In: *Phys. Rev. B* 108 (8 Aug. 2023), p. L081304. URL: <https://link.aps.org/doi/10.1103/PhysRevB.108.L081304>.
- [83] André Eckardt and Egidijus Anisimovas. “High-frequency approximation for periodically driven quantum systems from a Floquet-space perspective.” In: *New Journal of Physics* 17.9 (Sept. 2015), p. 093039. URL: <https://dx.doi.org/10.1088/1367-2630/17/9/093039>.
- [84] André Eckardt. “Colloquium: Atomic quantum gases in periodically driven optical lattices.” In: *Rev. Mod. Phys.* 89 (1 Mar. 2017), p. 011004. URL: <https://link.aps.org/doi/10.1103/RevModPhys.89.011004>.
- [85] Chunqing Deng, Feiruo Shen, Sahel Ashhab, and Adrian Lupascu. “Dynamics of a two-level system under strong driving: Quantum-gate optimization based on Floquet theory.” In: *Phys. Rev. A* 94 (3 Sept. 2016), p. 032323. URL: <https://link.aps.org/doi/10.1103/PhysRevA.94.032323>.
- [86] Henk T.C. Stoof, Koos B. Gubbels, and Dennis B.M. Dickerscheid. “Optical Lattices.” In: *Ultracold Quantum Fields*. Dordrecht: Springer Netherlands, 2009, pp. 391–430. URL: https://doi.org/10.1007/978-1-4020-8763-9_16.
- [87] Karlo Penc and Andreas M. Läuchli. “Spin Nematic Phases in Quantum Spin Systems.” In: *Introduction to Frustrated Magnetism: Materials, Experiments, Theory*. Ed. by Claudine Lacroix, Philippe Mendels, and Frédéric Mila. Berlin, Heidelberg: Springer Berlin Heidelberg, 2011, pp. 331–362. URL: https://doi.org/10.1007/978-3-642-10589-0_13.

BIBLIOGRAPHY

- [88] David J. Griffiths and Darrell F. Schroeter. “Quantum Mechanics in Three Dimensions.” In: *Introduction to Quantum Mechanics*. Cambridge University Press, 2018, pp. 131–197.
- [89] Christopher Gerry and Peter Knight. “Emission and absorption of radiation by atoms.” In: *Introductory Quantum Optics*. Cambridge University Press, 2004, pp. 74–114.
- [90] Dan M. Stamper-Kurn and Masahito Ueda. *Spinor Bose gases: Explorations of symmetries, magnetism and quantum dynamics*. 2012. URL: <https://arxiv.org/abs/1205.1888>.
- [91] Rodrigo A. Muniz, Yasuyuki Kato, and Cristian D. Batista. “Generalized spin-wave theory: Application to the bilinear–biquadratic model.” In: *Progress of Theoretical and Experimental Physics* 2014.8 (Aug. 2014), p. 083I01. URL: <https://doi.org/10.1093/ptep/ptu109>.
- [92] W. Greiner, D.A. Bromley, and B. Müller. “The SU(3) Symmetry.” In: *Quantum Mechanics: Symmetries*. Springer Berlin Heidelberg, 2012. Chap. The SU(3) Symmetry, pp. 183–205. URL: <https://books.google.com/books?id=bVnrCAAAQBAJ>.
- [93] Walter Pfeifer. *The Lie Algebras $su(N)$. An Introduction*. 1st ed. Springer Book Archive. Birkhäuser Basel, July 2003, pp. X, 432. URL: <https://doi.org/10.1007/978-3-0348-8097-8>.
- [94] Masuo Suzuki. “Decomposition formulas of exponential operators and Lie exponentials with some applications to quantum mechanics and statistical physics.” In: *Journal of Mathematical Physics* 26.4 (Apr. 1985), pp. 601–612. URL: <https://doi.org/10.1063/1.526596>.
- [95] Lloyd N. Trefethen and J. A. C. Weideman. “The Exponentially Convergent Trapezoidal Rule.” In: *SIAM Review* 56.3 (2014), pp. 385–458. URL: <https://doi.org/10.1137/130932132>.